

Molecular engineering of patchiness and flexibility in all-DNA rods

Inaugural dissertation

for the attainment of the title of doctor
in the Faculty of Mathematics and Natural Sciences
at the Heinrich Heine University Düsseldorf

presented by

Katarina Gvozden
from Belgrade, Serbia

Düsseldorf, January 2022

from the Institute of Biological Information Processing, Biomolecular Systems
and Processes (IBI-4)
Forschungszentrum Jülich

Published by permission of the
Faculty of Mathematics and Natural Sciences at
Heinrich Heine University Düsseldorf

Supervisor: Prof. Dr. Jan K.G. Dhont
Co-supervisor: Dr. Stiakakis Emmanuel

Date of the oral examination: 21/01/2022

Declaration of Authorship

I hereby certify that this thesis has been composed by me and is based on my own work, unless stated otherwise. No other person's work has been used without due acknowledgement in this thesis. All references and verbatim extracts have been quoted, and all sources of information, including graphs and data sets, have been specifically acknowledged.

Date:

Signature:

*“A scientist is not a person who gives the right answers, a
scientist is a person who asks the right questions.”*

Claude Lévi-Strauss

Abstract

Molecular engineering of patchiness and flexibility in all-DNA rods

It has been known for long that the two dominant stabilizing forces in the formation of the DNA double helix arise from the stacking between adjacent base-pairs and from the pairing between complementary bases. Base stacking between the end of individual duplexes, the so-called blunt-end stacking, plays a crucial role in DNA self-assembly, which in turn is a key process in the nanofabrication of novel DNA-based materials. However, the importance and a suitable modelling of these weak and non-covalent intermolecular stacking forces in collective phenomena, such as the hierarchical assembly in all-DNA rod-like liquid crystals, is not yet fully understood.

The thesis at hand explores how a selective screening scheme of these attractions in the stiff all-DNA constructs with a linear (full-paired duplexes) and a chain-stick (gapped duplexes) architecture, on the basis of single-stranded DNA capped blunt-ends, can be developed to encode specific directionality in their intermolecular interactions (patchiness). The work presented herein provides a full characterization of blunt-ends stacking interactions between DNA-duplexes, and clarifies the role that they play in the formation of smectic all-DNA phases. A rich packing and molecular conformation diversity are generated within these layered liquid crystalline structures by controlling the flexibility and the patchiness of the above-mentioned all-DNA rods. Through a combination of small-angle X-ray scattering and polarization microscopy, assisted by Monte Carlo simulations, the concentration-dependent phase diagrams of semi-capped and fully-capped linear DNA duplexes are provided. Moreover, the phase diagram of purely repulsive all-DNA chain-sticks (fully-capped gapped DNA duplexes) is found to exhibit a remarkably rich phase behaviour, as reflected by the multiple order-to-order liquid crystal transitions by altering the chain-stick flexibility (chain length) or/and DNA concentration.

The presented results offer a direct proof of the blunt-ends monovalent attractive patchy character, highlighting unique opportunities for advancing the field of directed self-assembly in DNA-based liquid crystals.

Zusammenfassung

Es ist seit langem bekannt, dass die beiden vorherrschenden Kräfte, die zur Stabilisierung der DNS-Doppelhelix führen, aus der Paarbildung komplementärerer Basen und aus der stapelartigen Anordnung (stacking) benachbarter Basen-Paare resultieren. Das Stacking zwischen den Enden einzelner Doppelstränge, die sogenannte Stapelung stumpfer Enden (blunt-end stacking) spielt eine entscheidende Rolle bei der Selbstorganisation von DNS, was wiederum ein Schlüsselprozess bei der nanofabrikation DNS-basierter Materialien ist.

Allerdings ist die Bedeutung noch nicht völlig geklärt, die diese schwachen, nicht-kovalenten intramolekularen Stapelkräfte für kollektive Phänomene haben, wie z. B. der hierarchischen Organisation in Flüssigkristallen aus stäbchenartigen reinen DNS-Mesogenen.

In der vorliegenden Arbeit wurden Methoden entwickelt, diese anziehenden Kräfte abzuschirmen, indem die stumpfen Enden mit verschiedenen DNS-Einzelstrangmotiven abgedeckt wurden. An steifen, vollständig gepaarten DNS-Doppelsträngen und an unvollständig gepaarten oder lückenhaften Doppelsträngen, sogenannte Ketten-Stäbchen Architekturen, wurde untersucht, wie diese Abschirmungsmechanismen genutzt werden können, um eine spezifische Direktionalität der intramolekularen Wechselwirkung (Patchiness) zu erzeugen. Die vorgelegte Arbeit liefert eine vollständige Charakterisierung der Wechselwirkung durch Stapelung stumpfer Enden zwischen DNS-Doppelsträngen und klärt deren Rolle bei der Bildung von smektischen Phasen aus reinen DNS-Bausteinen. In diesen geschichteten Flüssigkristallstrukturen kann eine reiche Vielfalt von Packungen und molekularen Konformationen erzeugt werden, indem Flexibilität und Patchiness der erwähnten DNS-Stäbchen kontrolliert werden.

Mit einer Kombination von Kleinwinkel-Röntgenstreuung und Polarisationsmikroskopie unterstützt mit Monte Carlo Simulationen wurden die konzentrationsabhängigen Phasendiagramme von halb und vollständig abgedeckten, linearen DNS-Doppelsträngen erstellt. Außerdem wurde gefunden, dass das Phasenverhalten von vollständig repulsiven DNS-Ketten-Stäbchen-Strukturen (vollständig abgedeckte, lückenhafte Doppelstränge) bemerkenswert vielfältig ist, was sich in mehrfachen Ordnung-Ordnung Übergängen in Abhängigkeit von Flexibilität (Länge des Kettensegments) und der Konzentration zeigt.

Die präsentierten Ergebnissen stellen einen direkten Beweis für die monovalente, attraktive, uneinheitliche Natur der stumpfen Enden dar und eröffnen einzigartige Möglichkeiten, das Gebiet der gerichteten Selbstorganisation in Flüssigkristallen auf DNS-Basis weiter zu entwickeln.

Acknowledgements

“You can, you should, and if you are brave enough to start, you will.” And I did. Reaching this moment certainly was not an easy task and besides hard work, big effort and love for what you are doing, it requires a lot of energy, energy that is needed in the time of a struggle to motivate yourself, push harder and win. Since we all know that there is no such thing as a *perpetuum mobile*, I would like to thank everybody who were, in one way or another, a part of the mechanism and my source of energy when needed, which helped me reach this finish line.

First and foremost, I would like to thank my scientific advisor, **Dr. Emmanuel Stiakakis- Manolis**, for being my scientific and a life teacher. Thank you for all the help and for always being there. I will remember this journey of a lifetime and all your advice, which really helped me surpass myself and made me grow in every sense. Thanks to you I carry more than only a scientific victory from this, so your mission is completed! *Σας ευχαριστώ από τα βάθη της καρδιάς μου!*

I would like to thank my supervisor **Prof. Jan Dhont**, whose doors were always open and who provided his help and support along the way, whether through scientific comments during seminars or through jokes during encounters in the kitchen. Furthermore, for showing me, especially in the end, that our limitations really should not stop us from trying. Last but not least, thank you as well for giving your comments and remarks about the thesis and recognizing my work and effort.

I would also like to thank our collaborator, **Prof. Cristiano de Michele** who spent his time and effort and did a great job to provide us a simulation support of our experimental results.

Special thanks to **Dr. Emmanuel Kentzinger** and **Dr. Ulrich Rücker** whose expertise and advice made all of our GALAXI measurements possible.

Sometimes listening to a student’s concerns may seem like a simple and insignificant job, but to a student in a moment that seem like a despair, means a world and gives a special kind of an energy boost to continue forward. Therefore, I would like to thank **Prof. Peter Lang** who made me feel heard when needed and for always having or finding an answer to my every question. Furthermore, thank you for the help with the German translation of the thesis abstract.

I owe no less gratitude to **Prof. Gerhard Nägele** for every good word, smile, motivation and the scientific support. Moreover, for making me feel seen and acknowledged as a young scientist. I am also thankful for every question during seminar talks, that sparked a desire to find better answers. Special thanks to **Ulrike Nägele**, that was kind enough to offer to save my jeans from a “Tipp-ex” disaster, only few weeks after I started this adventure.

We are maybe a small group, but without the influence of every gear wheel the clock would not work, so a big thanks to: **Dr. Johan Buitenhuis** – thank you for all safety instructions, for asking how I am doing and for sharing your experiences, I enjoyed

listening to them; **Prof. Simone Wiegand** – thank you for taking care of the group and our seminars and for every smile in the hallway; **Dr. Kyongok Kang** – thank you for the Korean pancakes and for making every group meeting more colourful and fun. Soon we will cheer with some “Lady killers”; **Prof. Pavlik Lettinga**- for making me worry about questions that you will ask during my presentations; they were always on point and made learn more. Thank you as well for recognizing my work and for the nice comments when they were deserved; **Dr. Yi Liu**- thanks for caring and all the great advice and support; **Dr. Zihan Tan**- thank you for your kindness that inspired me to be a better person; **Dr. Hartmunt Kriegs, Dr. Namkyu Lee, Dr. Gunwoo Park, Dipl. Ing. Hans Hoffman** and **Angelika Schmitz** – thank you for all your help, big or small, whenever needed! I was feeling special being part of our group.

Now a big and a special thanks to young padawans of our group who really brought colour into my every day, at and outside of work: **Shilpa, Alex** and **Amir**- thanks for all the fun lunches, hallway and lab encounters. I will not forget our “outside of work” adventures as well. I enjoyed being a part of the team with you and organizing a Christmas party and all the PhD hats.

Then there are former colleagues, who were there from my very start and I would like to express a special thank you to **Mariano** and **Oli** for sharing their experiences and wisdom. Thank you, **Mariano**, for being a breath of fresh air and a wind of change in every sense, you made a change in my life and for that I am very grateful. Thank you as well for bringing my attention to clean underneath my keyboard – very important topic! **Oli**, thanks for being a support at the beginning when it was the hardest and for giving me a lifetime lesson that made me more self-aware.

To my office roomy, dear **Mehrnaz**, I owe a great gratitude for a wholehearted support in person and on distance. As I said, every good thought counts and thank you. Thank you for all the patience and understanding from the very beginning. It was my pleasure sharing an office with you and I think we did a great job making it comfier. I enjoyed all of our adventures, shopping, serious or less serious talks, our power naps, lunches, Friday motivational singings, parties, sleepovers, ideas... All of this gave me an energy to push harder and I am looking forward to our future celebrations and adventures. از صرمی قلب از شمل پیل گذارم.

Now, PIVOT!!! I would like to thank people who were there for me through better or worse, when it hasn't been my day, my week, my month or even my year, no matter how far or close they live at the moment from me.

Andrea, Ribice, there are no words (in Italian or Serbian) that could express how grateful I am to you. Thanks for being a true and an outstanding friend. Thanks for all your unconditional support and help, understanding and for all the nice and fun time we had during the past years and especially in this last period. I am looking forward to more, but... new adventures won't include Villanious or guess what? ARTICLES! Thank you once again for creating all these great stories with me, which I will definitely tell to my kids as bed time stories. Grazie mille!

Dear **Andrea**, or should I say Andrea B, I am so grateful that I have been on this journey with you and I cannot imagine a better person to have as a roomy and support. Thank you for being there even before the very beginning and till the end. Certainly, this is only an ending of “an era” (“Oh, all right. But, you know, I gotta say, I don't think six (three and a half years) years counts as an era. - An era is defined as a significant period of time...”) but a beginning of a new and more exciting period that we will share. Thank you for all small and big things which I will remember forever and thank you for making me a part of your family. I would also like to thank your family and name each one of them because they care and make me feel part of the team. **Oma Matilde, Birgit, Christina, Lukas, Patrick and Sophia** – Thank you so much for making me feel at home. It gave me a tremendous strength and a motivation.

Drage Juliške frajle- **Bogdana i Jelo**, hvala vam za toliko lepih trenutaka koje smo proveli zajedno, za sve svirke i šetnje uvek ispunjene smehom. Hvala za sve savete kao i za dubokumne razgovore koji su me uvek inspirisali. Hvala **Medi** što je jedno malo krzneno stvorenje koje se odmah zavoli. Njena radost nema cenu.

Dragi **Hana i Emine**, hvala vam što ste me doveli na ovaj put odrastanja, hvala na podršci, i hvala što ste podelili radost ovog trenutka sa mnom.

We started as a mentor and an internship student and it resulted into me expanding my friends network for two more valuable persons. **Sanja and Albert** thank you for all the support and nice moments we had, when we were here together, and also now whenever and wherever we meet. Draga **Sanja**, hvala ti beskrajno na svoj podršci i strpljenju koje si mi pružala dok si bila ovde, a i sad na daljinu. Prezahvalna sam što sam te upoznala i što smo imali toliko lepih trenutaka i slavljaja zajedno i radujem se novim. Hvala ti što si mi, još od prakse, uvek dokazivala i pokazivala da ja ovo mogu. Takođe, hvala ti što si baš mene izabrala!

Dragi **Tanja, Dušane, Dunja i Leno**, hvala vam što ste ušli u moj život i što ste mi ukazali poverenje da na neki način budem deo vase porodice. Deo ove pobede ide i vama, jer ste se vi pojavili u momentu kad mi je najviše trebala motivacija i da se podsetim ko sam, šta sam i koliko mogu. Posebna zahvalnica **Leni**, na svim crtežima I sitnicama, jer stvarno donose sreću. Hvala ti što me inspirišeš da budem bolja osoba.

Veliku zahvalnost dugujem i mojim dragim ljudima iz Beograda, koji su preživeli sa mnom mnogo različitih bitaka. **Ivana**, Prijatelju, hvala ti na svim druženjima, srpskim, holandskim i nemačkim avanturama kao i podršci. Ko bi rekao da ćemo od “Atoma” i “Alhemičara” doći do Groningena i Juliha. Pre sedam meseci si mi dostavila tvoje “reči slobode”, hvala ti što si me podržala I inspirisala da ih ja sad tebi dostavim.

Drage devojke, **Đuki i Tićo**, koje me uvek dočekate raširenih ruku i sa osmehom na licu, hvala vam za sve osmehe i za sva druženja svih ovih godina. Hvala vam i na podršci koju ste mi pružale tokom ovog perioda, kao i tokom svih prethodnih, lepih ili ružnih. Moraćemo ovo da proslavimo jednim Pictionary-jem. **Veki**, hvala ti što si mi pružala podršku kad se čujemo i inspirisala me svojim lepim događajima. **Šaki**, drago mi je da smo se susreli i ovde, hvala na podršci, na slušanju i na smehu kad god je bio potreban.

Hajde sad, ništa manje ne očekujem od tebe, nego da I ti dođeš do trenutka pisanje zahvalnice. Pokaži im od čega smo! Draga **Miro**, hvala ti što si tu od malena, što si uvek mislila na mene i slala mi pozitivnu energiju i misli. I hvala ti što si bila ona koja je me je podsećala šta imamo za domaći i kad je koji kontrolni, verujem da je to mnogo bitan preduslov da neko uopšte i ima šansu da dođe do ovde. Hvala ti i na svim slatkim susretima kad god dođem, jer budimo realni tvoja kuhinja je mir.njam! Draga **Džajo** hvala ti što si svaki susret ili dopisivanje ispunila zabavom i smehom. Hvala još jednom što si bila tu da me uvek podsetiš koliko je važno čuvati i misliti na sebe.

Joki i Bokiša, šta da vam kažem, još jedna teza koju ste preživeli sa mnom. Obećavam neću više. Hvala vam na svoj podršci, lepim trenutcima i rečima. Bokiša, samo najjači opstaju. Hvala ti što navijaš i veruješ u mene sve ove godine. Nastavljamo dalje jako u susret novim događajima i slavljima, jer samo neka nam je SRETNO I BERIĆETNO.

Dragi prijatelji iz Holandije, **Jano i Bato**, hvala vam što ste i geografski i srcem blizu. Ne mogu rečima da opišem koliko mi je vasa podrška na ovom putu značila i Koliko me je svaki naš susret ispunjavao i davao snagu. Hvala vam za svu podršku, pažnju, lepe trenutke, kao i što ste mi se našli na početku kad je bilo najpotrebnije. Vaši uspesi su moja radost, inspiracija i motivacija, hvala vam što sam deo njih. Za nove pobeđe i nova slavlja!

Želim da se zahvalim porodici koja je mene izabrala i koju sam ja izabrala. **Teta Stojanka, Sandra i Sanja** hvala vam za svesrdnu i bezuslovnu podršku na blizinu i na daljinu. Hvala vam što ste uvek uz mislima bile uz mene, hvala na svakoj lepoj reci, svakoj poruci podrške, na tome što kad god da dođem, uživamo u udobnosti teta Stojankinog gnezda, sanjamo velike snove i napunimo baterije. Sve to mi je mnogo značilo da dođem ovde gde jesam. Posebnu zahvalnost dugujem **Sanji**, koja već godinama korača sa mnom, rame uz rame. Kad sam sa tobom, stojim sa armijom i hvala ti na tome. Hvala ti na svojoj ljubavi, pažnji, iskrenosti u osam ujutru ili u dva uveče. Hvala ti što sanjamo i rastemo zajedno već 15 godina! You are my person! Hvala i žestokom momku, **Dušanu**, koji je uvek imao otvorena vrata za mene i pristajao na moje ludosti kad sam priređivala Sanji nešto. Hvala i što si stojički podneo muke našeg pevanja do ranih jutarnjih časova!

Ništa manje bitni, želela bih da se zahvalim „**grupaciji Kajganić**“. **Dragi ujo i drage ujna, Ivo i Evo** hvala vam što ste svih ovih godina verovali u mene. Hvala na neizmernoj snazi i podršci i na podsećanju ko sam i odakle dolazim. Kad vas pogledam, osećam se ponosno što sam deo ovakve porodice i znam da sam nepobediva. Hvala vam što čuvate Beograd dok ja nisam tu. Radujem se i proslavi ovog trenutka uz naravno nezaobilaznu i nadaleko poznatu ujinu PIZZA PITU!

Tu je i my brother from another mother, hvala ti **Dule** za sve ove godine ispunjene smehom, za to što mi ulivaš snagu kad god je potrebno, što me štitiš na daljinu, što me uvek dočekaš sa osmehom, koji obožavam i što si ulazio i ulaziš u sve ludosti sa mnom. Hvala ti što smo zajedno bolji ljudi. Radujem se novim avanturama i proslavama!

Šta reći mojoj porodici, **mama i tata BRAVO**, uspeli ste! Hvala vam za sve godine podrške i ljubavi. Hvala vam sto ste uvek davali najbolje i najviše što ste mogli. Zbog vas sam ovo što jesam i dajete mi neverovatnu snagu da uvek radim na sebi i budem najbolja verzija sebe. Bodrite me da hrabro koračam dalje i krčim svoj put i ostvarujem svaki cilj. Hvala vam za sve „dobro se obuci“, „cuvaj se“, „jesi ponela kišobran“, tegle dzema, kesice supe, kutije plazme, iako imam previše već, ali eto da se nadju. Želela bih i da se zahvalim svojoj sestri **Jeleni**, koja mi je pomogla da nađem sebe i da čvrsto stanem na svoje noge.

Na kraju bih želela da se zahvalim osobi koja je prošla sa mnom kroz najbolje i najgore, koja i dalje veruje u mene bez zadržke. **Nenade, Nešo**, hvala ti što si verovao u mene i kad ja nisam, što si mi ulivao snagu i dozu razuma kad god je to bilo potrebno. Hvala ti što sa tobom mogu da budem u potpunosti što jesam i što me tvoja ljubav čini boljom osobom. Hvala ti za sve predivne trenutke koji su prošli i koji će doći. Hvala ti što si video i razumeo, iako ja nisam, zašto mi je ovaj put potreban i što mi nisi dao da odustanem od ovog trenutka, a samim tim ni od sebe. Hvala ti od sveg srca za to što jesi i za to što smo mi! Takođe želela bih da se zahvalim i tvojoj porodici, koja je navijala za ovaj trenutak koliko i mi- **teta Nataša, čika Zorane, Nevena, Nidžo i Ivo**-hvala!

Sincerely,

Katarina

Table of Contents

Declaration of Authorship	iii
Abstract	v
Zusammenfassung	vi
Acknowledgements	vii
Introduction	1
Chapter 1	3
1.1 Liquid crystals	3
1.1.1 Structure of liquid crystal phases	4
1.2 Liquid crystalline behaviour of anisotropic molecules.....	6
1.2.1 Onsager's theory for the isotropic-nematic transition of rod-like particles ..	6
1.2.2 Phase behaviour of hard spherocylinders.....	8
1.3 Liquid crystalline behaviour of chiral molecules	11
1.3.2 Fundamental knowledge about the DNA.....	12
1.3.3 DNA liquid crystals.....	16
1.3.4 Molecular engineering of DNA LC	18
1.4 Bibliography	19
Chapter 2	22
2.1 Instrumental methods	22
2.1.1 Small angle X-ray scattering.....	22
2.1.2 Polarized optical microscopy (POM).....	28
2.1.3 Gel electrophoresis.....	29
2.2 Computational methods.....	30
2.3 Material and synthesis	31
2.3.1 Oligonucleotides.....	31
2.3.2 Other materials	37
2.3.3 Synthesis.....	37
2.3.4 Sample preparation.....	39
Bibliography.....	40
Chapter 3	41
3.1 Introduction	41
3.2 Effects of blunt-end stacking suppression on DNA LC ordering.....	45
3.3 Phase behaviour of all-DNA rods with different terminal modifications	55
3.4 Effects of an increasing terminal attraction strength on the self-assembly of SC-duplex.....	57

3.5	Monte-Carlo simulations	59
3.6	On the molecular origin of a columnar phase in SC-duplexes	66
3.7	Summary and conclusions	70
	Bibliography	72
Chapter 4	76
4.1	Introduction	77
4.2	Design and fabrication of all-DNA repulsive rods	79
4.3	Phase behaviour of all-DNA repulsive rods with tunable aspect ratio	84
4.3.1	Structural characterization of all-DNA rod-like liquid crystals	84
4.3.2	Phase diagram of purely repulsive all-DNA rods	95
4.4	Summary and conclusions	100
	Bibliography	101
Chapter 5	105
5.1	Introduction	105
5.2	Previous and current work on the all-DNA blunt-ended chain-sticks	107
5.3	The self-assembly of purely repulsive all-DNA chain-sticks	111
5.4	Phase diagram of the repulsive all-DNA chain-sticks	114
5.5	Summary and conclusions	116
	Bibliography	118
Conclusions	119

Mojim dodeljenim i izabranim porodicama...

To my given and chosen families...

Introduction

Liquid crystals (LCs) represent a thermodynamically stable state of matter featuring long-range orientational order but complete or partial absence of long-range positional order. This confers LCs anisotropic optical and mechanical properties, thus allowing them to be categorised between isotropic liquids and crystalline solids. Moderately dense aqueous suspensions of short double-stranded DNA (dsDNA) are well known systems that exhibit multiple lyotropic LC (LLC) ordered phases. The main reasons are rooted in the DNA's characteristic base stacking and helical architecture, which endows dsDNA molecules with shape anisotropy, chirality and an unusual stiffness with a persistence length l_p^{dsDNA} of about 50 nm (~150 base pairs).

Blunt-end stacking interactions are weak, non-covalent attractions between the ends of two dsDNA helices, each terminating in a base-pair (bp). Recent studies on concentrated solutions of blunt-ended ultra-short DNA duplexes revealed that these rod-like particles can form polydisperse semi-flexible linear aggregates, which possess a sufficient shape anisotropy to form LLC phases such as chiral nematic (cholesteric) and columnar. Furthermore, these weak stacking forces were exploited to allow an externally triggered dynamic assembly and disassembly of DNA origami structures in the field of DNA nanotechnology, resembling processes which occur in many dynamic biomolecular complexes such as actin filaments or microtubules.

In this thesis, a direct proof of the blunt-end's monovalent attractive patchy character is presented, highlighting unique opportunities for advancing the field of *directed* self-assembly in DNA-based liquid crystals. Specifically, it is proposed that rich “*assembly-information*” can be encoded into all-DNA constructs by controlling the directional entropic forces through particle shape anisotropy engineering and by site-specific positioning of blunt-ends. This is demonstrated through the synthesis and study of the self-assembly of all-DNA constructs with linear (fully-paired duplexes) and chain-stick (gapped duplexes) architecture. The beneficial effects of the above hierarchical self-assembly concept are reflected by the formation of a novel smectic phase with a bilayer architecture in one blunt-end capped linear DNA duplexes, and by the remarkable entropy-driven unfolded smectic-to-folded smectic transition in purely repulsive all-DNA chain-sticks by altering the chain length and/or DNA concentration.

The thesis at hand is structured as follows:

- In **Chapter 1**, a brief literature overview of liquid crystals, with emphasis on their lyotropic counterparts with rod-like architecture, is given. The most frequently encountered LC phases are presented. The idea of entropy-driven transitions is discussed through a short presentation of the seminal theoretical and simulation works of Onsager, on a system of infinitely thin hard rods, and

of Frenkel and co-workers, on hard spherocylinders, respectively. Finally, a general introduction to the DNA structure and the most recent works on DNA-based liquid crystals are presented.

- In **Chapter 2**, a short description of the experimental techniques that were employed for the synthesis and characterization of all-DNA constructs, and the study of self-assembled structures, is provided. Furthermore, a detailed list of the DNA sequences used in this study for the fabrication of all-DNA constructs is included.
- In **Chapter 3**, through a combined experimental and numerical study, the self-assembly behaviour of selectively blunt-end capped linear DNA duplexes is investigated. Unambiguous evidence of the formation of a novel smectic phase with a bilayer architecture in one blunt-end capped DNA duplexes (semi-capped (SC)-duplexes) is provided. The control over the strength of the terminal base-stacking (blunt-end) attraction in the SC-duplexes allowed to stabilize the hexagonal columnar phase at varying DNA densities, reaching much higher density values than in the past studies. Furthermore, the lack of stacking polarity, mediated by the complete defeat of the blunt-end attractions (fully-capped (FC)-duplexes), reveal that the so far elusive monolayer smectic phase in DNA rod-like liquid crystal ordering is a thermodynamically stable phase.
- In **Chapter 4**, the phase diagram of purely repulsive all-DNA rods as a function of the shape anisotropy L/D , where L is the length and D the thickness of the rods, is explored. Using model systems containing stiff DNA duplexes with blocked blunt-end stacking interactions, it is demonstrated that such DNA-based rods can be considered as an accurate experimental realization of hard spherocylinders.
- In **Chapter 5**, the phase diagram of blunt-ended gapped DNA duplexes (chain-sticks with attractive terminal sites) is re-visited. Previous studies have shown the formation of smectic phase in concentrated aqueous solutions of these all-DNA constructs, with the gapped molecules attaining a folded conformation in this two-dimensional fluid layers mesophase. Through the synthesis and study of the self-assembly behaviour of their purely repulsive counterparts (with variable chain length), unambiguous evidence for the entropic origin of the folded conformation is provided.

Chapter 1

Rod-like liquid crystals and DNA

Liquid crystals are an intriguing and complex state of matter, which have properties between isotropic liquids and crystalline solids. In this chapter, a general introduction about lyotropic liquid crystals, together with the description of the most common encountered forms of their ordering, will be presented. A brief discussion regarding the recent aspects of the DNA-based liquid crystals which have drawn the attention of soft-matter community and, which are relevant to the topic of the thesis at hand, will be provided. Finally, the main features of the DNA molecule will be briefly presented.

1.1 Liquid crystals

Matter can be classified into three main aggregation states: gas, liquid and solid. The liquid and solid states constitute the condensed matter, which differs from the gas state because it possesses a certain degree of order in the arrangement of the particles. For certain materials, molecules form a semi-ordered state between crystal and liquid. Such materials are called liquid crystals.¹ They are anisotropic fluids, which are characterized by refractive index, dielectric constant, elastic behaviour, or viscosity, etc.²

Liquid crystals (LC) were discovered in 1888 by the Austrian botanist Friedrich Reinitzer, who reported on the observation of compounds (cholesteryl benzoate and cholesteryl acetate) with apparently two melting points. In his experiments, Reinitzer increased the temperature of a solid sample and watched the crystal change into a fuzzy liquid at 145.5°C. The material changed into a clear, transparent liquid with a further increase of the temperature up to 178.5°C. The colour of the turbid liquid also changed from red to bright blue-violet to pale blue, and the whole process was reversible. Since Reinitzer wasn't able to interpret his discovery, he sent his work to Otto Lehmann, a professor of physics at the university of Heinrich Hertz in Karlsruhe, Germany. Professor Lehmann examined them under the polarizing microscope and coined the term "flüssiger Kristall" (liquid crystal).³

Between 1970s and 1980s liquid crystals were extensively studied, bringing to the development of new theories and new technological innovations. These smart materials are useful for developing LC displays, modulators, sensors, solar cells, etc.; they even found an application in biology, medicine and food industry.⁴

Coming back to the order within the condensed matter states, we should distinguish between liquid and solid. While in a liquid state the molecules diffuse randomly throughout the solution without any orientational order, in a solid state they possess an orientational and a three-dimensional positional order. Liquid crystals, being an

intermediate state, show a long range orientational order and generally, at most, two-dimensional long range positional order. Depending on the degree of the order, three commonly occurring forms of liquid crystals can be distinguished: nematics, smectics and columnar.

Liquid crystals can be classified in two groups: thermotropic, whose LC phase transitions are temperature dependant, and lyotropic, whose LC phase transitions are temperature and concentration dependant. Liquid crystalline phases occur most commonly in systems with anisotropic particles like calamitic (rod-like), discotic (disc-like) and sanidic (board-like).^{5,6}

1.1.1 Structure of liquid crystal phases

1.1.1.1 Nematic phase

Nematic (N) is classified as the simplest of liquid crystal phases, which has no long-range positional order, but solely possesses orientational order. Molecules tend to align along a preferred direction with their long axes. The average local direction of the molecular long axes is called nematic director (\mathbf{n}) and it also represents the direction of the optical axis of the system.⁷ The arrangement of molecules in a nematic phase and the nematic director are presented in **Figure 1.1**. Nematic generally behaves as a uniaxial material with a rotational symmetry around the director. The main characteristic of the nematic phase is an anisotropy in the transmission of light (birefringence).¹ Observing the nematic under a polarized optical microscope, a thread-like texture is noticeable, where threads appear as a consequence of a defect in the orientation of the director (disclinations). Owing to these defects, nematic got its name, that comes from the Greek “νήμα” (nema), which means “thread”.^{5,7}

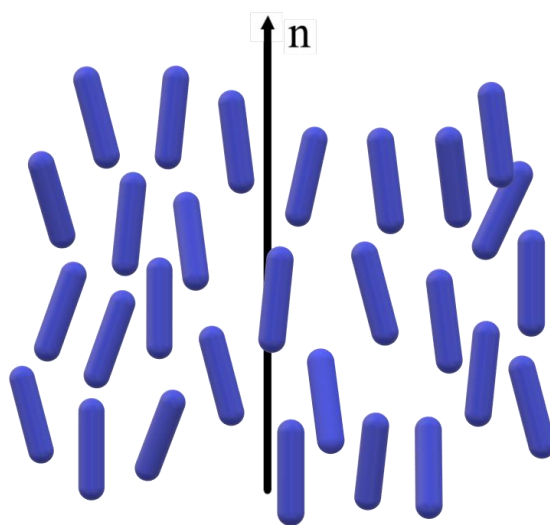


Figure 1.1 Molecular arrangement of rod-like molecules in the nematic liquid crystal phase. Molecules have orientational order, but no positional one. The average orientation is termed director, \mathbf{n} .

1.1.1.2 Smectic phase

The word smectic originates as well from the Greek language, and it means “soap-like”. Besides having a long range orientational order, in such phase molecules possess a partial positional order: they are arranged in layers.¹ The director \mathbf{n} is perpendicular to the smectic layer and it is parallel to the smectic layer normal, \mathbf{k} . Molecules within the smectic layers are randomly positioned with no correlations in or across the layer planes.⁶ Depending on the structural variations inside the smectic layers, we can distinguish three different types of smectic phase:

- **Smectic A ($Sm-A$)**, where molecules are arranged perpendicularly to the smectic layer plane, with no long-range crystalline order between them. $Sm-A$ can be viewed as a stacking of two-dimensional fluids with well-defined inter-layer spacing. This is presented in [Figure 1.2a](#).
- **Smectic B ($Sm-B$)**, where molecules within layers are locally hexagonally ordered, and possess a long-range positional order in the direction perpendicular to the layers. The top view of the layer in $Sm-B$ shows hexagonal order, as seen in [Figure 1.2b](#).
- **Smectic C ($Sm-C$)**, which is similar to the $Sm-A$, as molecules are arranged in layers without positional correlations. In this phase the director \mathbf{n} is tilted with respect to the smectic layer normal by an angle θ , so the phase has biaxial symmetry (see [Figure 1.2c](#)).

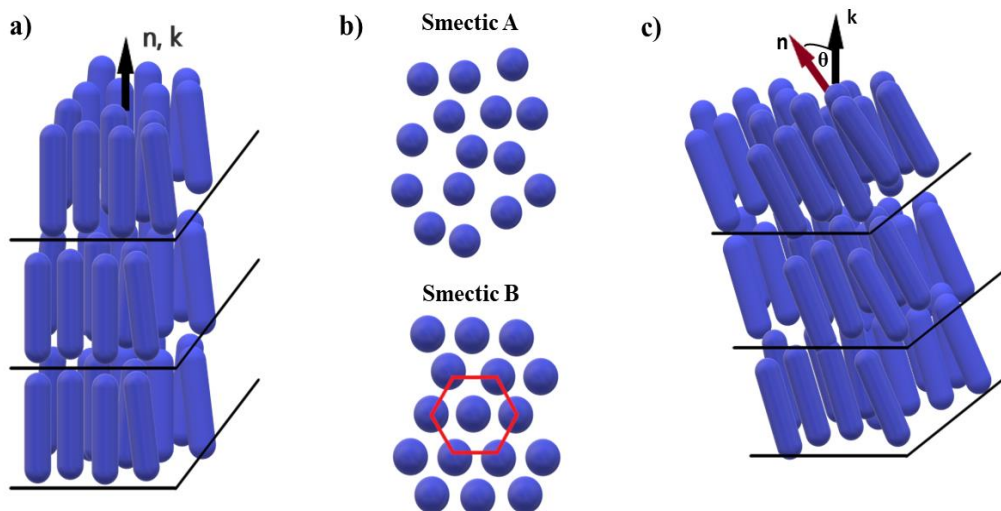


Figure 1.2 *a)* Schematic representation of the smectic-A phase. Molecules are organized in layers, where \mathbf{n} is the director, which is parallel to the layer normal, \mathbf{k} . *b)* Molecular packing in smectic layers of smectic A and smectic B, seen from above. *c)* Schematic representation of the smectic C phase, where the director \mathbf{n} is tilted by an angle θ , with respect to the layer normal, \mathbf{k} .

1.1.1.3 Columnar phase

The columnar phase (Col) was first recognized among stacked flat discotic molecules, which formed columnar structures. Consequently, it was initially called discotic liquid crystal phase, until recent studies showed that various non-discotic mesogens can also assemble into columnar structures.⁸ Therefore, the term columnar liquid crystal is more appropriate. These columnar structures are laterally ordered in the plane perpendicular to the column axis and, depending on their order, we can distinguish several types: hexagonal, tetragonal, rectangular, tilted etc. In **Figure 1.3**, adapted from the paper of E. Grelet,⁹ an hexagonal columnar phase formed by rod-like particles is shown.

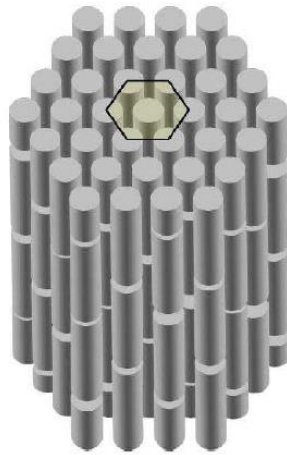


Figure 1.3 Schematic representation of rod-like particles arranged in a columnar hexagonal phase.⁹

1.2 Liquid crystalline behaviour of anisotropic molecules

Since through experiments we studied the liquid crystal phase behaviour of DNA rod-like particles, we will introduce and explain the entropy-driven transitions of these common colloidal models, which are important for understanding the DNA self-assembly.

1.2.1 Onsager's theory for the isotropic-nematic transition of rod-like particles

In 1949 Onsager provided a theoretical study of a system that has a higher entropy in the ordered phase than in the disordered one.¹⁰ He described the appearance of the nematic phase in the suspensions of thin, hard rods. The term “hard” refers to the fact that two particles cannot occupy the same space, and they only have repulsive interactions when in contact. A transition from an orientationally disordered phase

(isotropic) to an orientationally ordered one (nematic) is explained as purely entropy-driven. During the ordering of hard rods, with an increase of the density, the

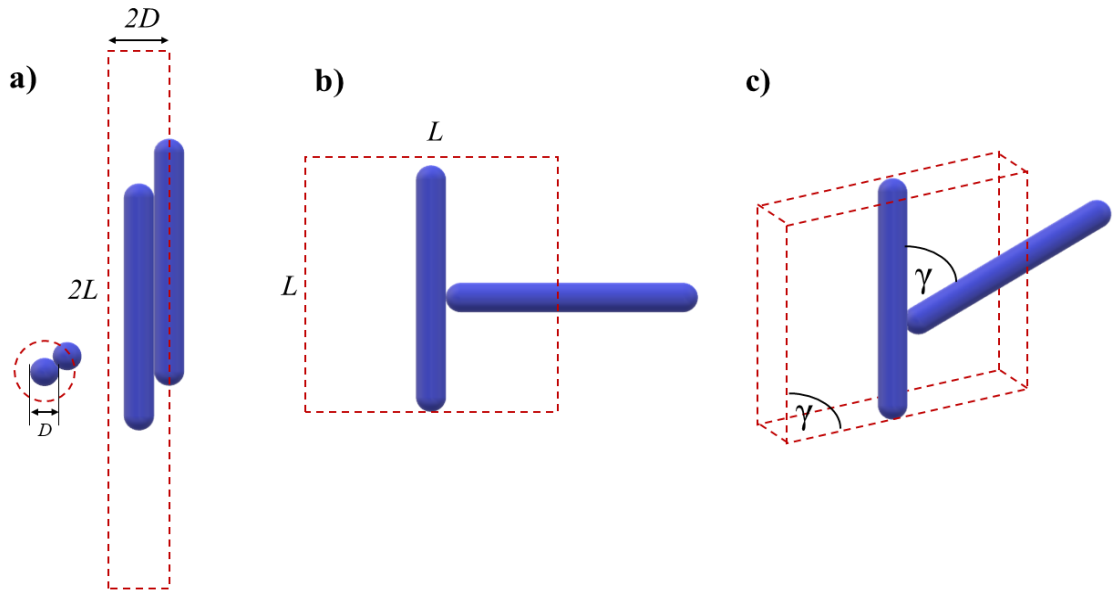


Figure 1.4 A schematic representation of the excluded volume of rods when they are : **a)** in a parallel orientation, **b)** in a perpendicular orientation, and **c)** oriented with an angle between them. The red dashed lines show the volume that is forbidden, in all three cases, to the second rod because of the first one.

orientational entropy decreases, along with the excluded volume, while the translational one increases. The latter means that rods gain more accessible (free) volume per particle. In **Figure 1.4**, it is schematically represented that parallel rods take up less space than perpendicular or randomly oriented ones, leaving more space for them to move in.

Onsager's theory is limited to the very long and very thin rods ($L/D \rightarrow \infty$), since it neglects the second virial coefficient. Therefore, few assumptions have been made:

1. Steric repulsion is the only force of importance; the rods cannot penetrate each other;
2. The volume fraction is much smaller than unity;
3. The rods are very long, thus their length L is much larger than their diameter D

For a dilute system of spherical particles, where binary interactions are dominant, the Helmholtz free energy F can be written in terms of a virial expansion to first order in the system overall concentration c :

$$F = F_0 + k_B T \left[\log c + \frac{1}{2} cV + O(c^2) \right] \quad 1.1$$

where F_0 is an additive constant, the second virial coefficient V has the dimensions of a volume and accounts for binary interactions, while $O(c^2)$ represents terms of higher order due to simultaneous interactions between three or more particles. When there are no additional interactions between particles, V corresponds then to the excluded volume,

i.e., the volume that is not accessible for a sphere due to the presence of another sphere. This simpler case introduced us to the statistical treatment of excluded volume effects.

Considering now the system of hard rods, the excluded volume effects become orientation dependent, so beside the overall concentration, the angular distribution of the rods needs to be specified:

$$f(\theta, \varphi)d\Omega = f_a \sin \theta d\varphi d\theta \quad 1.2$$

which expresses the probability of a given rod to point along a direction within a small solid angle $d\Omega = \sin \theta d\varphi d\theta$.¹¹ The number of rods per unit volume, pointing in a small solid angle $d\Omega$ around a direction labelled with a unit vector \mathbf{a} , is $cf_a d\Omega$. By the definition, the sum of these small solid angles must give the overall concentration c , therefore:

$$\int f_a d\Omega = 1 \quad 1.3$$

The free energy of hard rods can be written then in the following form:

$$F = F_0 + k_B T \left(\int f_a \log(4\pi f_a c) d\Omega + \frac{1}{2} c \iint f_a f_{a'} V d\Omega d\Omega' \right) + O(c^2) \quad 1.4$$

where the first integral describes the entropy loss associated with the molecular alignment (f is not constant), while the second integral describes the excluded volume effects; $V(\mathbf{a}\mathbf{a}')$ is the volume excluded by a rod in a direction \mathbf{a} to a rod in a direction \mathbf{a}' . Generally, for spherocylinders of length L and diameter D , the excluded volume V is given by¹²:

$$V = 2L^2 D |\sin \gamma| + 2\pi D^2 L + \frac{4}{3} \pi D^3 \quad 1.5$$

where γ is the angle between the spherocylinder, with an orientation specified by the unit vector \mathbf{a} along its long axis, and a rod with orientation \mathbf{a}' . The last two terms of **Equation 1.5** are the end effects, and they depend on the exact form of the rods near the ends. These effects are ignored in the case of Onsager's long and thin rods, thus the excluded volume in that case is (see **Figure 1.4c**):

$$V = 2L^2 D |\sin \gamma| \quad 1.6$$

By employing a variational method and comparing the free energies of the isotropic and nematic phases, Onsager got the values for the volume fractions above which the nematic phase is formed, $\Phi_{nem} = 4.5 D/L$ and the value below which the isotropic phase appears, $\Phi_{iso} = 3.3 D/L$.¹³

1.2.2 Phase behaviour of hard spherocylinders

As already mentioned, Onsager's work offered an explanation of the transition from isotropic to nematic phase of purely repulsive particles. Although this theory was exact and only applicable to infinitely thin and long rods, due to the truncation of the virial expansion, it provided a starting point for further studies on rods with less extreme shape. Theoretical studies by Vroege and Lekkerkerker, and by Odijk, provided

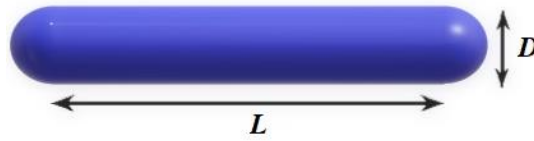


Figure 1.5 A model of a hard spherocylinder: the spherocylinders are characterized with a cylinder of length L and diameter D , capped by hemispheres on both sides.

improvements of the Onsager's initial theory, and tried to make it more applicable to shorter rodlike particles. These theories played an important role in the exploration of the phase behaviour of these systems. Hard spherocylinders are brought under the spotlight as good models for rod-like colloidal particles, due to their simplicity and the fact that they are easy to compute. They are characterized by their aspect ratio (L/D), where D is the width of the cylinder and L is its length, and they are capped on both sides with hemispheres of the same diameter (see **Figure 1.5**). Computer simulations of hard rods, restricted to certain L/D , confirmed that the isotropic-nematic transition is entropy driven, and even provided evidence for the appearance of higher ordered phases, like smectic and columnar.¹⁴⁻¹⁷

McGrother et al. performed an extensive simulation study on series of HSCs with $3 < L/D < 5$, which for $L/D=5$, confirmed the previous simulation results obtained in 1988 by Frenkel, where hard rods with this L/D exhibited an $I-N-Sm-A$ - solid transition. They also showed that, for $L/D=3.2$, there is a direct transition from I to $Sm-A$, while from $L/D=4$, $Sm-A$ is preceded by the N phase. Due to the fact that all these phase transitions

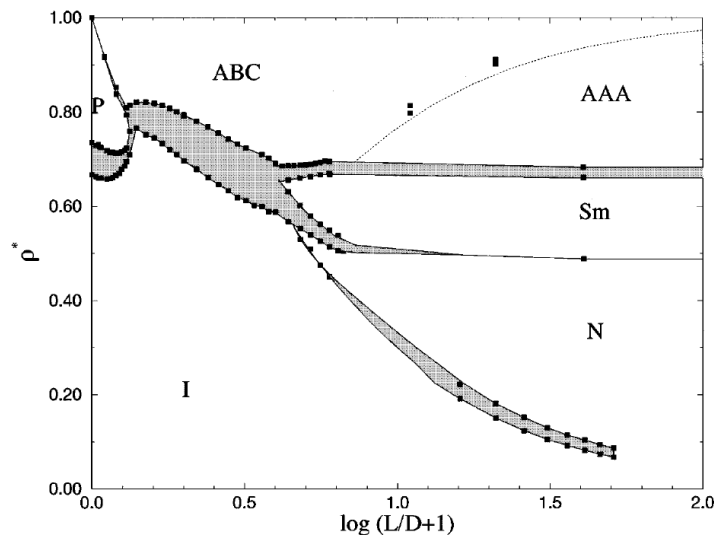


Figure 1.6 Phase diagram of hard spherocylinders with aspect ratio, $0 \leq L/D \leq 100$. The label I represents the low-density isotropic phase, N is nematic, Sm stands for smectic A phase, P is plastic solid, and AAA and ABC represent solid crystal phases with, respectively, AAA and ABC stacking.¹⁹

are followed by a discontinuous density jump, they are classified as first order transitions.¹⁸ A year later, Bolhuis and Frenkel published the results of their study, where they mapped out the complete phase diagram of hard spherocylinders over a wide range of densities and L/D values ranging from 0 to ∞ .¹⁹ Additionally, phase transitions in the limit for $L/D \rightarrow 0$ and for $L/D \rightarrow \infty$ were located. In the phase diagram of **Figure 1.6**, where the density ρ^* is plotted against $\log(L/D + 1)$, five different phases can be distinguished: isotropic, nematic, smectic-A, orientationally ordered solid ABC and AAA, and a plastic phase. With an increase of L/D towards ∞ , the I-N transition shifts towards the lower values of density, as predicted by Onsager's theory, while the N-Sm-A transition is not that sensitive to the changes of L/D of rods, and approaches the constant value of $\rho^* = 0.47$.

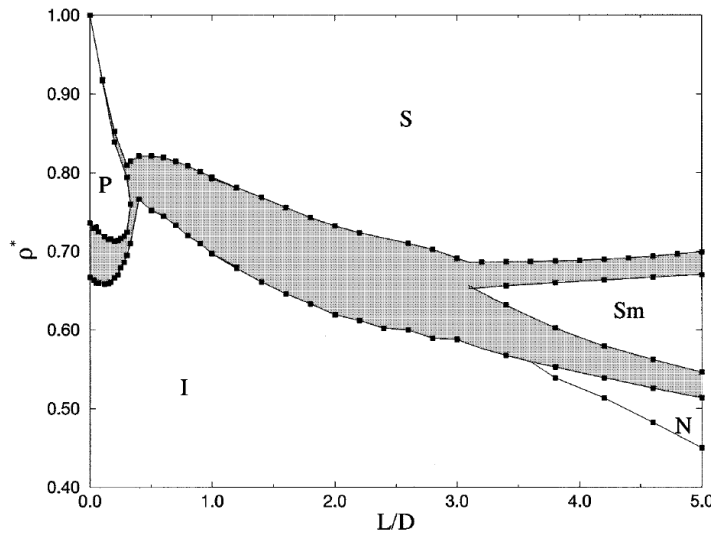


Figure 1.7 Phase diagram for hard spherocylinders $L/D \leq 5$, where *I* stands for isotropic phase, *N* for nematic, *Sm* for smectic-A, *S* for solid phase and *P* for solid plastic.¹⁹

In the phase diagram of **Figure 1.7**, the reduced density $\rho^* = \rho/\rho_{cp}$ of spherocylinders with $L/D < 5$ is plotted against L/D , where the density of regular close packing of spherocylinders ρ_{cp} is defined as:

$$\rho_{cp} = \frac{2}{(\sqrt{2} + (L/D)\sqrt{3})}$$

In the plot, we can see that smectic becomes stable already at $L/D \approx 3.1$, and I-N-Sm-A transition appears from about $L/D \approx 3.7$. Finally, according to these simulations, it was concluded that the liquid crystal phases smectic and nematic cannot be observed below L/D of 3.1.

Needless to say that the phase behaviour of rigid hard spherocylinders, obtained through simulations, may differ from the one of real rod-like systems, either because the interactions between real rod-like systems in experiments are not hard-core, or due to the fact that real colloidal particles are never fully rigid. Either way, it is interesting to study how much the phase behaviour of those systems differs or matches.

1.3 Liquid crystalline behaviour of chiral molecules

Chirality is the lack of mirror symmetry and any molecule, whose mirror image does not coincide with itself, is called chiral. Examples for such molecules can be found in all parts of nature, living or not, macroscopic or molecular. Chirality can be found in a lot of biomolecules: for example, amino acids are all chiral, except glycine, as nucleic acids, DNA and RNA, and also sugars building up their sugar-phosphate backbone.²⁰ All these chiral molecules tend to have a certain handedness, which classifies them as right- or left-handed.²¹ When one system is constructed with molecules of the same handedness, it is called homochiral. Proteins and nucleic acids fall into this category.

Molecular chirality strongly affects the liquid crystal properties. With some exceptions²², chiral mesogens usually tend to form chiral phases, which are characterized by a helical twisting of the long axis of the molecules. This way they can form nematic and smectic phases with an additional helical twist. Since the chiral nematic phase is in the scope of this thesis, we will focus on introducing that one.

1.3.1.1 Chiral nematic or cholesteric liquid crystal phase

The cholesteric phase exhibits orientational order, but no long-range positional order. As already seen in the nematic phase, the long axes of molecules align along a preferred direction, called the nematic director \mathbf{n} , which, in the case of the cholesteric phase, has a twist and rotates uniformly along a series of parallel planes (see [Figure 1.8](#)).⁷ This phase can be seen as a stack of nematic layers, with the director showing in each layer a twist with respect to the director from the layers below and above. The distance it takes the director \mathbf{n} to make a full rotation of 360° around a vertical direction is called cholesteric pitch p . Temperature, flow, chemical composition, and applied magnetic or electric fields can affect the cholesteric pitch.²³ The chiral nematic is usually marked with an asterisk next to the letter – N^* .

The main focus of this thesis is the chiral bio-polymer, DNA double-helix, whose solutions, at high enough concentrations, showed the appearance of the cholesteric phase. This phenomenon comes from the helicity and the handedness of the DNA molecule. Before continuing further to the liquid crystalline behaviour of the DNA, we will present some basic facts about the molecule itself.

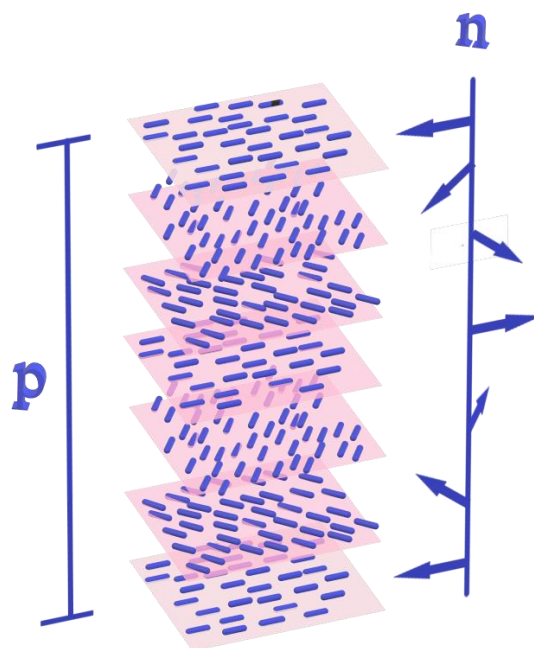


Figure 1.8 A schematic representation of the cholesteric phase, N^* . The average molecular orientation twists through the medium with a certain periodicity. The molecular orientation in planes is represented with \mathbf{n} , while p stands for the cholesteric pitch, thus the distance that it is needed by \mathbf{n} to make a full rotation of 360° around the vertical direction.

1.3.2 Fundamental knowledge about the DNA

Living organisms depend on the ability of their cells to store, retrieve and translate the genetic information needed for their creation and maintenance. The genetic information is stored in the form of genes, and DNA is their carrier. In euokaryotic cells, DNA is enclosed in a cell nucleus in the form of chromosomes, which duplicate and divide during the cell division process.²⁴

If we look at the DNA molecule more closely, we observe that it is a biopolymer that consists of two polynucleotide chains coiled around each other, which are composed of four types of nucleotide subunits, sugar – deoxyribose and phosphate groups. These subunits are: adenine (A) and guanine (G), which belong to the group of purine bases, and thymine (T) and cytosine (C), which belong to the group of pyrimidine bases. These bases can form base pairs through hydrogen bonding, and hold together two strands of a DNA helix. In each DNA base, there is a hydrogen atom bonded to a very electronegative atom, a nitrogen (N) or an oxygen (O), thus a partially positive charge (δ^+) is placed on the hydrogen atom. This positive charge is attracted by a nearby nucleophilic atom, which is partially negatively charged (δ^-) due to the possession of a nonbonding electron pair. Therefore, oppositely charged atoms attract each other, and in a process called hybridization, connect through hydrogen bonding.²⁵ This phenomenon is called Watson-Crick base pairing, and it is represented schematically in

Figure 1.9. Watson and Crick have established that the most stable base pairs are A-T and G-C.²⁶

Like any polymer, the DNA stiffness is characterized by a persistence length, L_p , which is ~ 50 nm (150bp) in the case of double stranded DNA, while it is in the range of 1 – 3 nm for a single-stranded DNA.^{27,28} Below these values DNA behaves as a stiff rod. This seemingly simple biopolymer with the diameter of only 2 nm, possesses unique and important physico-chemical properties, and it is gaining popularity even beyond biology. In order to manipulate the molecule into our advantage, we first need to understand how the molecule itself works and what are the interactions which are responsible for the three-dimensional structure of the DNA.

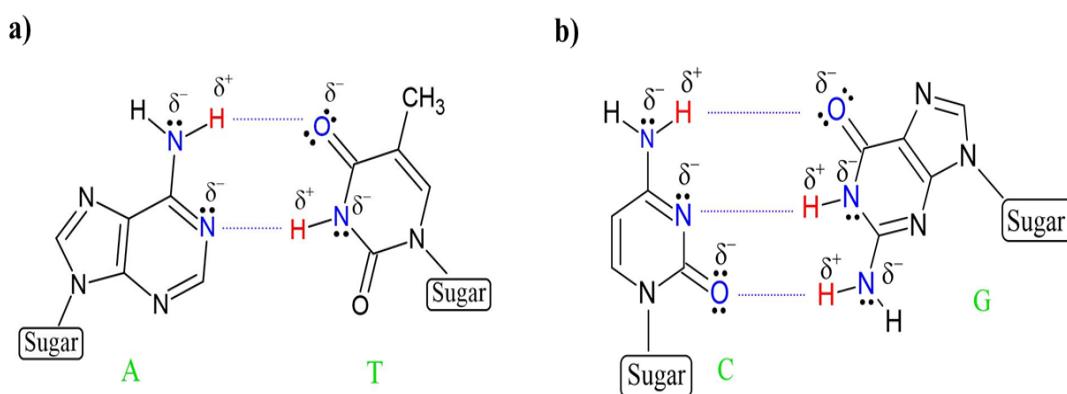


Figure 1.9 Watson-Crick base pairing through hydrogen bonding: **a)** between adenine (A) and thymine (T) and **b)** between cytosine (C) and guanine (G). Hydrogen bonds are represented with blue dotted lines. Atoms that participate in a hydrogen bonding are marked with the red colour - partially positive hydrogen atoms, and with the blue colour - partially negative charged electronegative atoms of nitrogen (N) and oxygen (O).

1.3.2.1 The three-dimensional structure of DNA

The chemical and structural properties of the polynucleotide strands are responsible for the DNA double helical structure. As already mentioned, polynucleotide strands consist of the deoxyribose sugar, the phosphate groups and the nitro-bases. The sugar and phosphate groups are soluble in water, while the nitro-bases, being aromatic hydrophobic compounds, are not. When the bases get attached to the sugar-phosphate backbone, a single-stranded DNA is formed. The bases hydrophobicity then drives the single-stranded DNA to form a structure where they would avoid to be in contact with water. Hence, a double-stranded DNA molecule is formed, where the bases are placed inside and the water-soluble sugar-phosphate backbone is placed outside. However, this still doesn't explain the formation of the helix. In order to do so, we need to consider also the sterical and geometrical properties of the DNA chain.

The distance between adjacent sugar or phosphate groups within one DNA strand is 6 Å. Due to the bond straining limitations, this distance cannot become much longer than 6.5 Å or shorter than 5.5 Å. Looking at the nitro-bases, the thickness of their flat aromatic part is 3.3 Å and, due to their chemical rigidity and inflexible bonds between atoms, this distance cannot be influenced much either. If the two strands assemble, bases are “tucked” inside this ladder structure. This arrangement leaves anyway a gap of 2.7 Å between bases, which needs to be eliminated to minimize the close contact of the bases with water.

One possible solution to eliminate the gaps would be skewing the ladder structure on one side. If the sugar-phosphate backbone is tilted by an angle of 30°, the distances between the adjacent phosphate groups would be satisfactory and the gaps would disappear. Nevertheless, the story doesn't end here since we know that, in nature, DNA forms a helical type of structure. The question is: why does DNA prefer a helical structure over a skew-ladder one? A closer look at the skew-ladder structure in **Figure 1.10**²⁵, reveals that there are many sterical hindrances between neighbouring atoms, which make this model inadequate. However, by twisting the skew-ladder structure, these unfavourable contacts between atoms are minimized, as well as the contact between the bases and water, and the criteria for the distances between phosphate groups and bases are fulfilled. Moreover, when we consider the three-dimensional conformation of the DNA double helix, it is basically a twisted ladder. It seems like in the end the DNA molecule found its way to have it all. Several studies confirmed that almost all DNA helices have 10 to 12 phosphate groups per turn of a helix. If we want to understand the basic principles that determine its structure, we can now take a look at the interactions inside the DNA, that stabilize the helix itself. Watson-Crick base pairing, together with base-stacking interactions, stabilize the DNA double helix. The base-pairing was already explained in section 1.3.2, and now we will introduce the base-stacking.

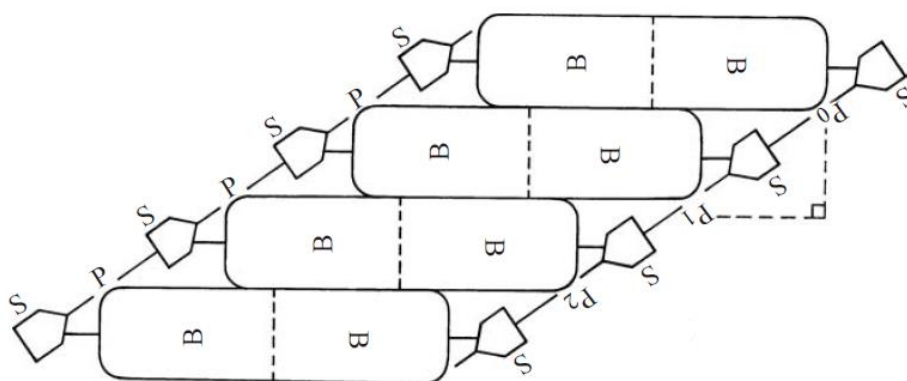


Figure 1.10 A skewed-ladder DNA structure which shows no gaps between adjacent base pairs.²⁵

1.3.2.2 Base-stacking interactions in DNA

Base-stacking interactions act between adjacent base pairs and pull the aromatic rings of the nitro-bases to stack on one another. These interactions are less selective than the base pairing ones, but they are the main ones that provide the stability of the double helix and promotes its forming, while the base-pairing provides the necessary specificity of the bonds.^{29,30} The occurrence of these interactions can be attributed again to the hydrophobicity of the bases and their tendency to minimize the contact with the water. However, based on the theory that explained the stacking of long flat molecules-porphyrins, we cannot neglect the role of partial electric charges in aromatic rings of nitrogenous bases in base stacking and attribute everything solely to the hydrophobic effect.³¹ There are three main contributions that are responsible for the base-stacking effect:

1. The hydrophobicity of the nitro-bases
2. The negative charge on the upper and lower surface of the nitro-bases
3. The partial charges on individual atoms in nitro-bases

We already mentioned that nitro-bases are hydrophobic molecules and, due to that, they have a strong tendency to avoid contact with water. Consequently, they will stack on one another in order to exclude the water from the inner part of the DNA. This behaviour can be explained with the hydrophobic effect. In an aqueous solution, water molecules associate strongly between themselves through hydrogen bonding. When such molecules come in contact with a water-insoluble DNA base, several hydrogen bonds are interrupted. In order for the water to maximize the hydrogen bonding between its own molecules, water-insoluble molecules segregate from the water molecules, by arranging themselves closer to each other.

The core of the nitro-bases consists of an aromatic component, which is rich in electrons and whose electron density is localized above and below the aromatic rings. The positive charge, that comes from the nuclei of various atoms that are joined to form the ring, is localized in between these negative charges. This means that an ideal vertical stacking of the bases would lead to a negative-to-negative charge repulsion, thus this arrangement is not the most favourable one. Therefore, the base-pairs in DNA can slightly slide to the left or the right side, in order to minimize repulsion. Furthermore, some positive-to-negative attractions can occur between the electrons of one base-pair and nuclei in another.

Coming to the effect due to the partial charges of the individual atoms in the bases, we know, as mentioned before, that some atoms with free electron pairs can generate a partial negative charge, while the ones that are connected to such atoms, generate a partial positive charge. Due to this, the nitro-bases tend to arrange themselves into positions where the charges of the same sign do not lie directly above or below each other. As a result, base-stacking can be fine-tuned by electrical interactions, meaning that it is sequence-dependent. The partial charges of each base are presented

schematically in **Figure 1.11**, where we observe a dense accumulation of negative charge along the major groove edge of the guanine ring, while the positive charge lies along the major groove edge of the cytosine ring. In contrast, A and T do not have joint

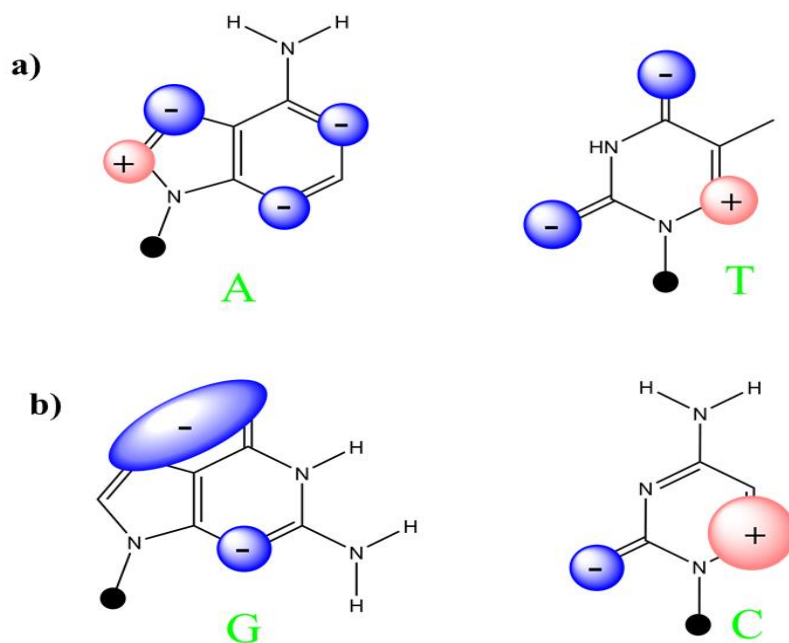


Figure 1.11 A schematic representation of accumulated charges on the rings of nucleobases: a) for A-T pair and b) for G-C pair

concentrations of partial electrical charge.²⁵ This could indicate that G-C pairs will stack much stronger than A-T ones, which could contribute to the overall stability of the DNA double helix.

The interplay of the described contributions results in base-stacking interactions that are attractive in an aqueous environment. These base-stacking interactions, besides being intramolecular and stabilizing the DNA helix itself, also occur intermolecularly, between blunt-ends of two DNA duplexes. In the latter case, these are called blunt-ends stacking interactions and they are responsible for an interesting DNA self-assembly behaviour in the formation of different DNA-based materials (liquid crystals), which will be presented in the next section.

1.3.3 DNA liquid crystals

1.3.3.1 Long DNA chains

Early studies of long DNA chains, obtained from biological sources, identified the formation of liquid crystalline phases *in vitro*, when the concentration is increased.^{32,33} *In vivo*, we find the DNA densely packed and, depending on the biological source and the local concentrations of the DNA in the cell, different liquid crystalline forms of

chromatin can be found. In bacteriophages and certain sperm heads, chromatin exhibits hexagonal packing, while in dinoflagellate chromosomes, bacterial nucleoids and mitochondrial DNA, it exhibits a cholesteric organization.^{30,34} This tells us that the geometries of the LC DNA in vitro can be linked to the organization of the chromatin in vivo. Therefore, a study of the DNA LC phases found in vitro can be of great significance for a better understanding of genome packaging and biological activity.³⁴⁻³⁷

The formation of LLCs in concentrated solutions of DNA has received considerable attention since 1980s. Extensive experimental studies of DNA chains, which are obtained through enzymatic cut and close to the persistence length l_p (~ 150 bp), showed a formation of various LC phases: chiral nematic phase (N^*), columnar hexagonal (Col) and crystal phase (K).³⁸⁻⁴² The studies revealed that the LC phase sequence depends on the concentration and length of DNA duplexes, and on the electrolyte environment.^{43,44} The occurrence of LCs in DNA solutions comes from its basic rod-like shape, which can even be identified with rigid rods, if the DNA fragments are short enough. In the case of rigid rods, called hard-rods, it is expected that, with increasing the concentration, the system transits from N to smectic A. However, in the case of DNA, the formation of such a phase has not been observed. It has been stated by Livolant that the smectic phase in the case of DNA is replaced with Col .³⁹ This behaviour is explained in terms of flexibility and polydispersity.³⁰

1.3.3.2 Short DNA chains

It was already mentioned that the behaviour of short enough DNA fragments can be identified with the behaviour of the hard spherocylinders. Theories^{10,45} and simulation studies of the hard spherocylinders, presented in section 1.2.2, predicted the appearance of LC phases for the aspect ratios L/D down to 3.1, while below this value, LC phases should not occur. Analogously, it was assumed that DNA fragments with $L/D < 3.1$ would not show the formation of LCs. However, a pioneering work on ultra-short DNA fragments between 6 and 20bp, $1 < L/D < 3.5$, showed a formation of LC phases above the critical concentration.⁴⁶ This was explained in terms of blunt-end stacking interactions, where DNA duplexes form weakly bonded linear aggregates through the coaxial stacking interactions between blunt-ends of two DNA helices. This is represented in Figure 1.12, adapted from the paper from Nakata et al.⁴⁶ Linear aggregates formed this way are polydisperse in length, stiff and long enough to undergo a phase transition from I to N^* , and finally to Col phase. These blunt-ends stacking interactions are no different from the ones that act within the DNA itself and stabilize the double helix, which were already explained in section 1.3.2.

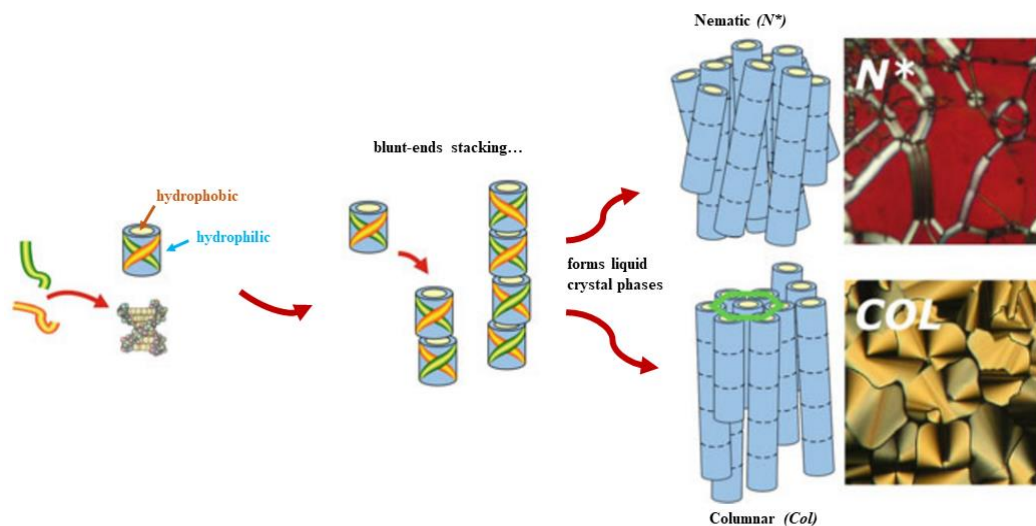


Figure 1.12 A schematic representation of the short DNA helices LC self-assembly through blunt-end stacking interactions. Helices stack on top of each other and form linear aggregates long enough to undergo a LC transition to N^* or Col phase. On the right side, POM micrographs are shown of corresponding phases.⁴⁶

1.3.4 Molecular engineering of DNA LC

The branch of DNA origami developed in the field of structural DNA nanotechnology, which gained its popularity already in 1980s. The concept of DNA nanotechnology is based on using the DNA as building material, with a carefully designed sequence, which, through the programmable molecular recognition, self-assembles into more complex two (2D)- and three-dimensional (3D) structures. The DNA origami concept additionally employs a large number of short single DNA strands, whose complementarity with specific parts of the long DNA strand controls the folding into the desired nanostructures. Over the past few years there has been a significant progress in this area, with different approaches being developed for a rapid and robust assembly into 3D-DNA origami structures. However, organizing such structures into macroscopic materials remained a significant challenge. Dogic et al. demonstrated the potential synergy between the DNA origami and the colloidal principles of assembly into macroscopic materials. DNA origami filaments, with the desired aspect ratios and microscopic twist, formed long-lasting cholesteric liquid crystals, one-dimensional supramolecular twisted ribbons and 2D colloidal membranes. Moreover, due to the remarkable possibility of the DNA origami technology to introduce changes into DNA filaments with a nanometre precision, they could explore and establish the connection between the microscopic filament structure and the macroscopic cholesteric pitch.⁴⁷

Once again, DNA demonstrated to be a molecule with endless possibilities. A detailed understanding of the DNA properties and the combination of knowledge developed in more than one area of research can create a rich variety of DNA structures

and a new area to explore. In this thesis, a simplified version of DNA LC molecular engineering will be presented, showing how the different modifications that were introduced in the DNA helices, on a sub-nanometre level, affected their LC phase sequence and behaviour.

1.4 Bibliography

1. Doi, M. Soft Matter Physics. *Soft Matter Phys.* (2013) doi:10.1093/acprof:oso/9780199652952.001.0001.
2. Dierking, I. & Al-Zangana, S. Lyotropic Liquid Crystal Phases from Anisotropic Nanomaterials. *Nanomaterials* **7**, 305 (2017).
3. Lehmann, O. Über fließende Krystalle. *Zeitschrift für Phys. Chemie* **4U**, 462–472 (1889).
4. Khokhlov, A. R. & Emelyanenko, A. V. Nanostructured liquid crystal systems and applications. *Beilstein J. Nanotechnol.* **9**, 2644–2645 (2018).
5. Mohanty, S. Liquid crystals — The ‘fourth’ phase of matter. *Resonance* **8**, 52–70 (2003).
6. Dierking, I. *Textures of Liquid Crystals. Textures of Liquid Crystals* (Wiley, 2003). doi:10.1002/3527602054.
7. Andrienko, D. Introduction to liquid crystals. *J. Mol. Liq.* **267**, 520–541 (2018).
8. Oswald, P. & Pieranski, P. *Part C: Smectic and Columnar Liquid Crystals. Liquid Crystals* (2020). doi:10.1201/9781482275285-11.
9. Grelet, E. Hexagonal Order in Crystalline and Columnar Phases of Hard Rods. *Phys. Rev. Lett.* **100**, 168301 (2008).
10. Onsager, L. the Effects of Shape on the Interaction of Colloidal Particles. *Ann. N. Y. Acad. Sci.* **51**, 627–659 (1949).
11. Kleman, M. & Lavrentovich, O. D. *Soft Matter Physics: An Introduction. Soft Matter Physics: An Introduction* (Springer New York, 2004). doi:10.1007/b97416.
12. Vroege, G. J. & Lekkerkerker, H. N. W. Phase transitions in lyotropic colloidal and polymer liquid crystals. *Reports Prog. Phys.* **55**, 1241–1309 (1992).
13. Selinger, J. V. *Introduction to the Theory of Soft Matter. Springer Handbooks* (Springer International Publishing, 2016). doi:10.1007/978-3-319-21054-4.
14. Frenkel, D. Onsager’s spherocylinders revisited. *J. Phys. Chem.* **91**, 4912–4916 (1987).
15. Frenkel, D., Lekkerkerker, H. N. W. & Stroobants, A. Thermodynamic stability of a smectic phase in a system of hard rods. *Nature* **332**, 822–823 (1988).

16. Veermm, J. A. C. & Frenkel, D. Phase diagram of a system of hard spherocylinders by computer simulation. *Phys. Rev. A* **41**, 3237–3244 (1990).
17. Stroobants, A., Lekkerkerker, H. N. W. & Frenkel, D. Evidence for one-, two-, and three-dimensional order in a system of hard parallel spherocylinders. *Phys. Rev. A* **36**, 2929–2945 (1987).
18. McGrother, S. C., Williamson, D. C. & Jackson, G. A re-examination of the phase diagram of hard spherocylinders. *J. Chem. Phys.* **104**, 6755–6771 (1996).
19. Bolhuis, P. & Frenkel, D. Tracing the phase boundaries of hard spherocylinders. *J. Chem. Phys.* **106**, 666–687 (1997).
20. Dierking, I. Chiral liquid crystals: Structures, phases, effects. *Symmetry (Basel)*. **6**, 444–472 (2014).
21. King, R. B. Chirality and Handedness. *Ann. N. Y. Acad. Sci.* **988**, 158–170 (2003).
22. Lorman, V. L. & Mettout, B. Theory of chiral periodic mesophases formed from an achiral liquid of bent-core molecules. *Phys. Rev. E* **69**, 061710 (2004).
23. Oswald, P. & Pieranski, P. *Nematic and Cholesteric Liquid Crystals: Concepts and physical properties illustrated by experiments*. CRC Press (CRC Press, 2005). doi:10.1201/9780203023013.
24. Alberts, B. *et al. Molecular Biology of the Cell. Molecular biology of the cell* (W.W. Norton & Company, 2015). doi:10.1201/9781315735368.
25. Calladine, C. R., Drew, H. R., Luisi, B. F. & Travers, A. . *Understanding DNA*. (Elsevier, 2004). doi:10.1016/B978-0-12-155089-9.X5000-5.
26. Watson, J. D. & Crick, F. H. C. Molecular Structure of Nucleic Acids: A Structure for Deoxyribose Nucleic Acid. *Nature* **171**, 737–738 (1953).
27. Tinland, B., Pluen, A., Sturm, J. & Weill, G. Persistence length of single-stranded DNA. *Macromolecules* **30**, 5763–5765 (1997).
28. Murphy, M. C., Rasnik, I., Cheng, W., Lohman, T. M. & Ha, T. Probing Single-Stranded DNA Conformational Flexibility Using Fluorescence Spectroscopy. *Biophys. J.* **86**, 2530–2537 (2004).
29. Yakovchuk, P., Protozanova, E. & Frank-Kamenetskii, M. D. Base-stacking and base-pairing contributions into thermal stability of the DNA double helix. *Nucleic Acids Res.* **34**, 564–574 (2006).
30. Bellini, T., Cerbino, R. & Zanchetta, G. DNA-Based Soft Phases. in *Peptide Based Materials*. **310**, 225–279 (2011).
31. Hunter, C. A. Sequence-dependent DNA Structure. *J. Mol. Biol.* **230**, 1025–1054 (1993).
32. Luzzati, V. & Nicolaieff, A. Etude par diffusion des rayons X aux petits angles

- des gels d'acide désoxyribonucléique et de nucléoprotéines : (note préliminaire). *J. Mol. Biol.* **1**, 127–133 (1959).
33. Robinson, C. Liquid-crystalline structures in polypeptide solutions. *Tetrahedron* **13**, 219–234 (1961).
 34. Livolant, F. Ordered phases of DNA in vivo and in vitro. *Phys. A Stat. Mech. its Appl.* **176**, 117–137 (1991).
 35. Chow, M. H., Yan, K. T. H., Bennett, M. J. & Wong, J. T. Y. Birefringence and DNA condensation of liquid crystalline chromosomes. *Eukaryot. Cell* **9**, 1577–1587 (2010).
 36. Rill, R. L., Livolant, F., Aldrich, H. C. & Davidson, M. W. Electron microscopy of liquid crystalline DNA: direct evidence for cholesteric-like organization of DNA in dinoflagellate chromosomes. *Chromosoma* **98**, 280–286 (1989).
 37. Earnshaw, W. C. & Casjens, S. R. DNA packaging by the double-stranded DNA bacteriophages. *Cell* **21**, 319–331 (1980).
 38. Davidson, M. W., Strzelecka, T. E. & Rill, R. L. Multiple Liquid Crystal Phases at High DNA Concentrations. *Nature* **331**, 457–460 (1988).
 39. Livolant, F., Levelut, A. M., Doucet, J. & Benoit, J. P. The highly concentrated liquid-crystalline phase of DNA is columnar hexagonal. *Nature* **339**, 724–726 (1989).
 40. Durand, D., Doucet, J. & Livolant, F. A study of the structure of highly concentrated phases of DNA by X-ray diffraction. *J. Phys. II* **2**, 1769–1783 (1992).
 41. Pelta, J., Durand, D., Doucet, J. & Livolant, F. DNA mesophases induced by spermidine: Structural properties and biological implications. *Biophys. J.* **71**, 48–63 (1996).
 42. Strey, H. H. *et al.* Refusing to twist: Demonstration of a line hexatic phase in DNA liquid crystals. *Phys. Rev. Lett.* **84**, 3105–3108 (2000).
 43. Rill, R. L., Strzelecka, T. E., Davidson, M. W. & Van Winkle, D. H. Ordered phases in concentrated DNA solutions. *Phys. A Stat. Mech. its Appl.* **176**, 87–116 (1991).
 44. Livolant F. Condensed phases of DNA. *Prog Polym Sci* **21**, 1115–1164 (1996).
 45. Franco-Melgar, M., Haslam, A. J. & Jackson, G. A generalisation of the Onsager trial-function approach: describing nematic liquid crystals with an algebraic equation of state. *Mol. Phys.* **106**, 649–678 (2008).
 46. Nakata, M. *et al.* End-to-End Stacking and Liquid Crystal Condensation of 6– to 20–Base Pair DNA Duplexes. *Science*. **318**, 1276–1279 (2007).
 47. Siavashpouri, M. *et al.* Molecular engineering of chiral colloidal liquid crystals using DNA origami. *Nat. Mater.* **16**, 849–856 (2017)

Chapter 2

Experimental methods and materials

In this chapter, the experimental methods employed for the synthesis, characterization and the study of the self-assembly of all-DNA liquid crystalline building blocks, will be presented. Small-angle X-ray scattering, polarized optical microscopy, and gel electrophoresis will be introduced. Monte-Carlo simulations that backed up our experimental work will be briefly described. Finally, a detailed list of the synthetic DNA oligomer sequences that were used for the fabrication of the all-DNA constructs will be given.

2.1 Instrumental methods

Small-angle x-ray scattering (SAXS) is the most powerful and non-destructive tool which we used to obtain the structural information of our samples. Combining it with polarized optical microscopy (POM) we have been able to obtain a more complete picture of our samples, since their results are complementary.

2.1.1 Small angle X-ray scattering

Introduction

Scattering, as a very important process that occurs in nature, serves as a model for the development of several robust instrumental methods. It is generally defined as: The physical process in which radiation is being deviated by local non-uniformities from straight propagation.¹ This deflected radiation carries information about the internal structure of an irradiated sample. Relying on this, scattering methods are used for the determination of the structure of matter. The instrumental techniques most frequently used in soft matter are X-ray, neutron, and light scattering. The choice of the technique depends on the size of the measured sample and on how the sample interacts with the radiation.² For scattering processes involving x-rays or neutrons, the typical wavelength scale is $\sim 0.1 \text{ nm}$, while the upper size limit for probed structure is 100 nm . For the light scattering, the typical wavelength of the used visible light is 500 nm , while the sample size can go up to $200 \mu\text{m}$. These scattering techniques are also distinguished depending on the interaction of radiation with matter. X-rays are interacting with the electrons of the sample and they are scattered due to the differences in electron density, hence the methods employing this scattering process would be appropriate for samples that have strong differences in electron density. Considering neutron scattering, these

strong-interacting particles are scattered by atoms nuclei via nuclear potential. These two methods are very good for getting the structural information of the analysed system. Finally, the light is scattered because of fluctuations in the dielectric constant of a material.^{1,3}

Curiosity in the field of x-rays was triggered after their discovery in 1895 by Wilhelm Röntgen.^{4,5} More than 10 years later, Max van Laue used X-rays for the idea of getting information of crystal periodicity when radiated with X-rays. This revolutionary idea gave birth to x-ray crystallography and brought him a Nobel prize.³ With the further evolution of x-ray crystallography, the use of x-ray scattering techniques progressed fast, bringing to the development of the small-angle x-ray scattering technique (SAXS), which gained its popularity in analyzing macromolecules in the 1970s after studies of tRNA from yeast (1967) and E.Coli (1972).⁶

As already mentioned in the previous chapter, DNA has an electron-rich phosphate backbone, thus it should strongly scatter X-rays. Taking this into account, as well as the length scale of our DNA constructs, the most suitable choice for analysing them is indeed SAXS.

For measuring our samples we used an in-house scattering setup, the Gallium Anode Low Angle X-ray Scattering(GALAXI), designed and built at the Jülich Centre for neutron Science (JCNS) in Forschungszentrum Jülich (**Figure 2.1**)⁷.

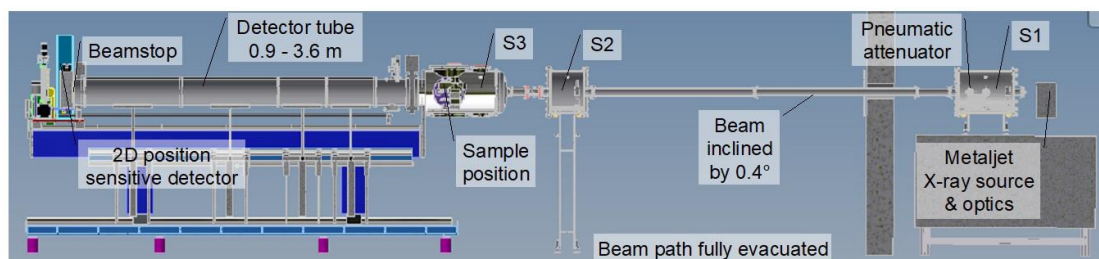


Figure 2.1 Schematic representation of GALAXI with its main components. The beam direction is from right to left.⁷

Every scattering instrument consists of a⁸:

1. Source
2. Collimation system
3. Sample holder
4. Detector

1. X-rays are usually produced by the bombardment of a metal anode with accelerated electrons. This process generates heat, so the anode should be water-cooled. There is anyway a limit to the power load that can be applied to a solid metal anode, defined by the maximum heat dissipation.³ Usually a rotating anode, microfocus x-ray tube or a sealed x-ray tube is used. The source in our case was an anode made of liquid gallium (Bruker AXS Metaljet), which can accept a much higher power load, does not need an

external cooling and produces a much brighter X-ray beam ($\lambda = 0.13414 \text{ nm}$) than other traditional sources.

2. The collimation system makes the beam narrow and defines the zero-angle position. In our case it is 4 m long and it consists of parabolic optics.

3. There is no universal sample holder built for every SAXS machine. We used a custom-made sample holder (see [Figure 2.2](#)) that could accommodate five different samples and had the possibility of temperature control. In the sample chamber of GALAXI, there is a two-axis motor that allows us to automatically change the position of the holder and irradiate our samples one after the other.



Figure 2.2 Custom-made GALAXI sample holder for five capillaries. The temperature control of the samples happens via the circulation of water in the back of the holder, allowed by the inlet and outlet.

4. We used a hybrid photon counting detector, Dectris Pilatus 1M, which has a resolution of the detector is 981×1043 pixels. The size of a pixel is $172 \times 172 \mu\text{m}^2$. SAXS data were analyzed using Fit2D software.⁹

Basics of SAXS

Generation of X-rays

In this paragraph we will clarify how x-rays are generated. During the bombardment of the metal anode with fast electrons, some of them interact with the atoms of the anode itself, losing energy in the process. Most of this energy is dissipated as heat, but a portion of it will be emitted as x-rays. When an electron passes through an atom of the anode, it gets decelerated, loses energy, which is then converted into an x-ray photon. These photons differ in energy, depending on how close to the nucleus of the atom the electron passes. This results in a broad x-ray continuous spectrum. This process is called *Bremsstrahlung*. It can also occur that an electron collides with an electron of the inner shell of the anodes atom, pushing it to a higher energy level. This electron will then return to its original energy level, emitting x-ray radiation in the process.³

Interaction of X-rays with matter

When the incident x-ray beam hits the sample, some of it interacts with the matter, while some passes through unchanged. Two kinds of interactions can happen: absorption and scattering.

When part of the incident radiation is absorbed by an atom of the sample, it can cause the expulsion of an electron from the atom, which then becomes unstable. Such an atom will then try to restore its original configuration by rearranging the remaining electrons in order to fill the hole left by the expelled one. During this process, the emission of fluorescent radiation by the atom occurs (for example x-rays with wavelengths different from the incident beam).

The relevant interaction for this thesis is the one involving the scattering of the incident beam through our sample, which can occur with or without energy loss. If a photon hits an electron and it is bounced away, a fraction of its energy is lost and absorbed by that electron. Such process is called Compton scattering, which is an inelastic scattering and does not carry structure information. On the other hand, scattering processes that carry structure information are elastic (i.e., Thompson). An elastic scattering occurs when photons recoil against strongly bound electrons without an energy transfer. The electrons start oscillating with the same frequency as the incoming radiation, re-emitting radiation with the same frequency. Since the emitted waves of nearby atoms oscillate synchronous with respect to each other, they produce coherent waves which will then interfere at the detector place. These interference patterns carry the information about the particle structure. If the irradiated sample is a very diluted solution, meaning that the average distance between the particles is much larger than the wavelength of the incident beam, the obtained interference pattern is then the sum of the waves coming from the single atoms inside one particle. This pattern changes in a fashion that is characteristic for the shape (the form) of the particle, which is therefore called **form factor**. In concentrated samples, the average distance between particles is comparable to their characteristic size. The scattering pattern will in that case not only contain the signal from a single particle, but from the neighbouring particles as well. This additional interference that we are getting from the neighbouring particles describes how the entire ensemble of particles scatters the incident radiation, giving us the so-called **structure factor**. Information about the positions of the particles with respect to each other is contained in this structure factor.⁸ The SAXS profiles of

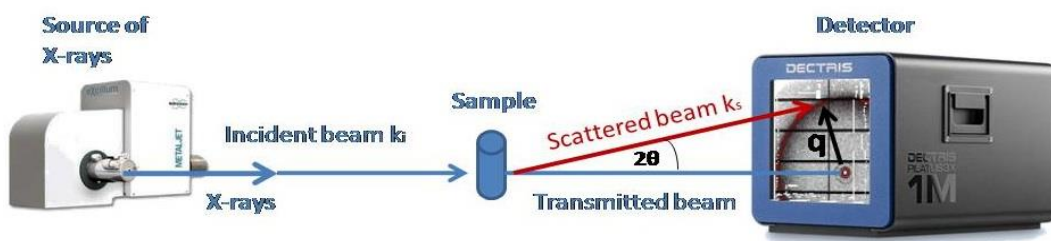


Figure 2.3 Schematic representation of a typical SAXS experiment.

our samples are a product of the form and structure factors.

The sketch of a typical small angle x-ray scattering is shown in **Figure 2.3**, where the scattering vector \mathbf{q} is the difference between the scattered wave vector \mathbf{k}_s and the incident beam wave vector \mathbf{k}_{in} .

$$\mathbf{q} = \mathbf{k}_s - \mathbf{k}_{in} \quad 2.1$$

A more detailed sketch of this scattering triangle is shown in **Figure 2.4**.

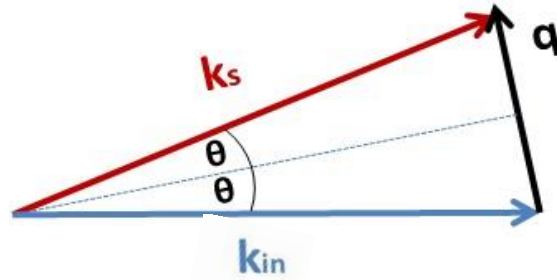


Figure 2.4 Representation of a scattering triangle where the scattering vector \mathbf{q} is defined as the difference between the scattered wave vector \mathbf{k}_s and the incident beam wave vector \mathbf{k}_{in} .

The angle between \mathbf{k}_{in} and \mathbf{k}_s is 2θ and, since there is no change in wavelength after the scattering, $|\mathbf{k}_{in}| = |\mathbf{k}_s| = k$. Using basic trigonometry we get the following:

$$q = |\mathbf{q}| = 2k \sin \theta \quad 2.2$$

The wave vector \mathbf{k} depends on the wavelength according to the relation $k = \frac{2\pi}{\lambda}$. Therefore, **Equation 2.2** becomes:

$$q = \frac{4\pi}{\lambda} \sin \theta \quad 2.3$$

From Bragg's equation, we obtain $\sin \theta = \frac{\lambda}{2d}$; substituting this into **Equation 2.3**, we get a relation between the scattering vector \mathbf{q} and the system characteristic dimension d , which corresponds to the typical distance between aligned particles in the system:

$$\mathbf{q} = \frac{4\pi}{\lambda} \cdot \frac{\lambda}{2d} \implies \mathbf{q} = \frac{2\pi}{d} \quad 2.4$$

The detector is positioned behind the sample, perpendicular to \mathbf{k}_{in} , as seen in **Figure 2.3**. It accepts only x-rays scattered in the forward direction, which limits the accessible q -values. Nevertheless, this can be influenced by changing the detector-to-sample distance.^{3,8}

Application of SAXS

The degree of structural order of a sample can be determined from the two-dimensional (2D) scattering pattern recorded by the detector. In the case of a single crystal, the 2D-SAXS pattern consists of intensive spots (reflections). Single crystals are anyway not common in soft biological systems, which our DNA constructs belong to. Soft matter materials involve instead numerous crystallites with random orientations, whose scattering patterns consist of diffraction rings around the incident beam, instead of intense spots. By applying shear or magnetic alignment to the sample, it becomes partially oriented, resulting into an intensity modulation of the diffraction rings.⁸

X-ray scattering from liquid crystals

Liquid crystals of rod-like molecules serve as attractive models for observing diverse aspects of ordering and their x-ray signature, due to their anisotropy and low-dimensional aspects. As it was already mentioned in the previous chapter, the characteristic of the nematic liquid crystal ordering is a long-range orientational order, where the centres of mass of molecules are randomly allocated. The scattering pattern of such system is characterized by a broad and diffuse large ring at high q -values (wide-angle), since there is no well-defined positional order in large regions.³ On the other hand, in smectic ordering, where molecules are packed in layers, we can observe a short-range positional order. This additional feature is indicated by the appearance of additional arcs at small q -values (small-angles; around the central beam stop) in 2D scattering patterns. It is interesting to see how the appearance of the 2D scattering pattern changes for different types of molecules packing in layers. This is represented

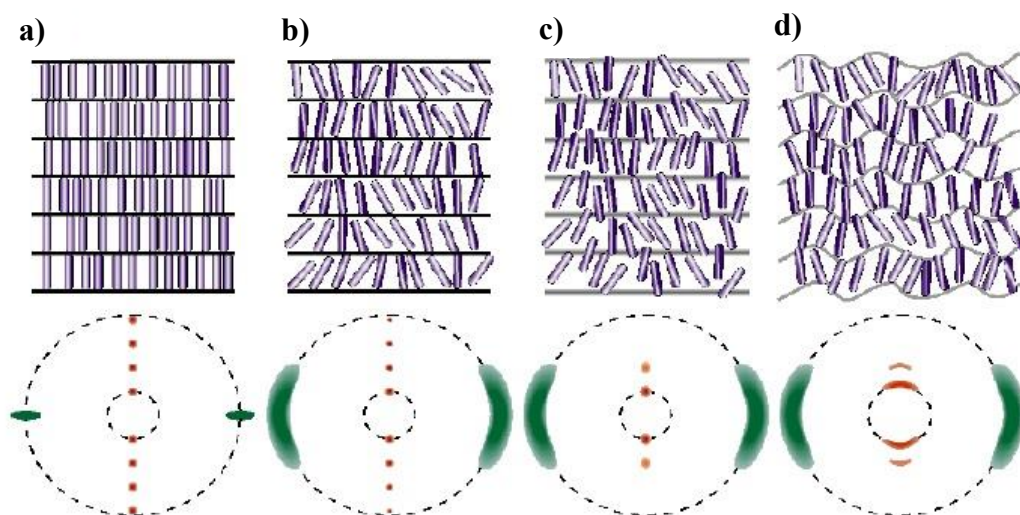


Figure 2.5 Sketches of the possible molecular orderings in a smectic-A phase and corresponding scattering patterns: **a)** ideal case with well-defined flat layers; **b)** flat layers with a certain degree of orientational disorder among particles; **c)** particles intermingle between layers which are still straight; **d)** layers and borders are not well-defined anymore¹⁰

in **Figure 2.5**. If we had the perfect case of orientational and translational order inside the layer, like in **Figure 2.5a**, the scattering pattern would consist of two sets of dots. Well-defined dots at small q -values represent order along the layers normal, while the distance between them is proportional to the sample layers thickness. The dots are well-defined because the layers are straight and the boundary between layers is very sharply defined. In-layer ordering and intermolecular distances are reflected by outer wide-angle dots. Since there is no perfect translational order along layers, these wide-angle dots are smeared radially. If some of the orientational order inside of the layers is lost, then wide-angle dots smear out azimuthally, like in **Figure 2.5b**. Small-angle dots remain well-defined because there is no disorder between the layers, while it is expected that higher order dots will become less visible. When molecules intermingle between layers, as seen in **Figure 2.5c**, but the straight layer interfaces are kept, high order small-angle dots are lost. In **Figure 2.5d**, the layer borders are not straight and well-defined anymore, which results in the smearing out of the small-angle dots and a scattering pattern with two sets of arcs.¹⁰

2.1.2 Polarized optical microscopy (POM)

As we could see from the previous section, SAXS is a very powerful tool for obtaining structural information about our samples. In order to get a complete picture, SAXS should be combined with polarized optical microscopy, since their results are complementary.

Polarized optical microscopy (POM) is a useful method for characterizing and obtaining an image of a birefringent sample. Birefringence is the optical property of a material having a refractive index that depends on the polarization and the propagation direction of light. In POM, a small part of the sample is magnified and its texture is observed. A detailed scheme of a polarizing microscope is shown in **Figure 2.6**. The microscope contains a polarizer between the pathway of incoming light and the sample, and another polarizer, called analyser, placed after the sample and before the observation tubes.¹¹ As a light source, a light halogen bulb is typically used. The incoming light is then reflected by a mirror to the polarizer, which converts it into plane-polarized light. This plane polarized light interacts with the birefringent sample that splits it into two waves that oscillate in perpendicular planes. After transmission through the sample, the waves are out of phase, to be then recombined by the analyser. Afterwards, re-combined waves oscillate along the same optical path and in same plane and the image can be observed through eyepieces or a digital camera system.¹²

In order to investigate the phase behaviour of all-DNA constructs studied in this thesis, controlled drying experiments were performed and POM images were obtained using a coloured CMOS camera (Motic) installed in a Axioplan 2 upright microscope, working in a transmission mode between crossed polarizers. Concentrated DNA solutions in the isotropic phase were loaded into hollow rectangle glass tubes (VitroCom) of thickness between 20 and 50 μm and sealed from one side. Therefore,

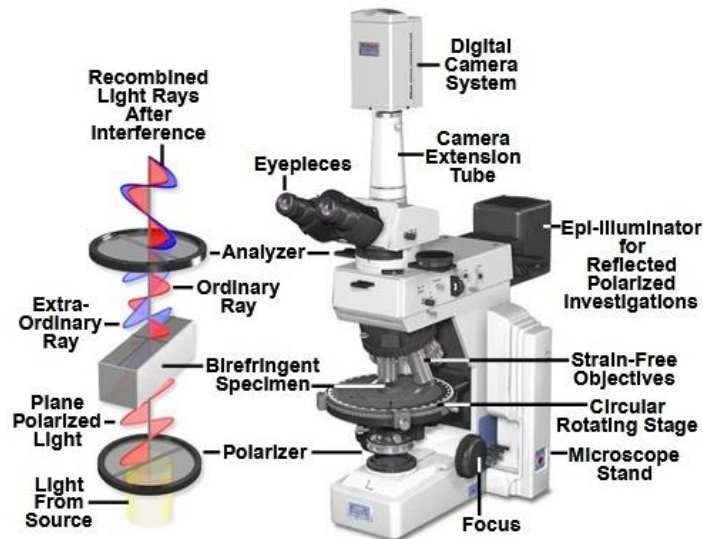


Figure 2.6 A schematic representation of a polarized light microscopy configuration with a sketch (on the left side) of a polarizing process.¹²

controlled evaporation occurred from one side only resulting in a concentration gradient of DNA across the tube. Images analysis was performed using Image J software.

2.1.3 Gel electrophoresis

Gel electrophoresis is widely used for studies of proteins and nucleic acids. It is a valuable tool for preparative, qualitative and quantitative analysis of macromolecules. Small differences in molecular weights and charges can be resolved, without affecting the sample structure. The principle of gel electrophoresis is based on a migration of charged molecules in an electric field. The electrophoretic mobility μ can be defined via the Debye-Hueckel-Henry theory as:

$$\mu = \frac{Z}{f} \quad 2.5$$

Where

$$f = 6\pi\eta r \quad 2.6$$

Z is the total molecular charge, f is the friction coefficient, η is the viscosity and r is the molecular radius. From this equation we can notice that molecules which have similar total charge will separate due to their differences in f . Since we exclusively study DNA molecules, which are all negatively charged, the only way to separate them when applying an electric field is due to their difference in size.^{13,14}

There are two types of gel electrophoresis that are mostly used: agarose and native polyacrylamide gel electrophoresis (PAGE). Agarose gels are made from a natural linear protein which, due to the hydrogen bonding, makes a gel matrix. It is used for

separating molecules with large molecular weight. Depending on the concentration of agarose we can have different pore sizes. The disadvantage of an agarose gel is the relatively low resolving power. The concentration of an agarose gel can vary from 0,2% to 3%, and it can separate a wide range of DNA sizes (100-40 000 base pairs). Compared to the agarose gel, PAGE has higher resolving power, therefore it is widely used for the separation of small molecular masses (40-2000 base pairs). PAGE is a chemically cross-linked gels of acrylamide and a cross-linking agent. The amount of acrylamide determines the pore size, which then determines the resolution of the gel. PAGE can process a bigger amount of sample without altering the resolution. Downsides of a PAGE gel are the long preparation time and the toxicity of its components. After separating our DNA molecules, the gel needs to be stained in order to visualize the DNA fragments. For this procedure, fluorescent intercalating dyes are used.

We used PAGE and agarose gel electrophoresis for evaluating and distinguishing the structural modification of our DNA constructs, after the thermal annealing procedure and all the preparation steps. The samples were dissolved and run in 1xTBE buffer (90mM Tris-Borate, 2mM EDTA, pH=8.3) at 10°C using a Mini-PROTEAN Tetra cell unit (Biorad). PAGE gels were post-stained with GelRed nucleic acid dye (Biotium), while agarose gels were pre-stained with the same dye.

2.2 Computational methods

Computer simulations enable the study of the thermodynamic properties of many-particle systems. The Monte Carlo (MC) approach, due to its simplicity and general applicability, is one of the essential and most commonly used method in scientific computing.^{15,16} MC simulations can reduce complex models to a set of basic events and interactions, when applied to physical systems, leading to the possibility of encoding the model behaviour through a set of rules which can be efficiently implemented on a computer.¹⁶ They propose random moves (translation or rotation) of a particle, which are either rejected or accepted with a given probability p , set in a way that ensure the correct sampling from a desired ensemble (typically NPT or NVT).

The experimental work presented in this thesis is supported by MC simulations, which were carried out by Prof. Cristiano De Michele and Alberto G. Orellana from Sapienza University of Rome, Italy. Besides backing up our experimental results, they allow us to better understand the self-assembly of all-DNA rods with controlled patchiness (**Chapter 3**) and blunt-ended chain-sticks (**Chapter 5**), as well as the physics behind it.

2.3 Material and synthesis

2.3.1 Oligonucleotides

From the company Biomers, the following custom-made and purified oligonucleotides were purchased and used for the synthesis of our systems:

All-DNA rods with controlled patchiness

Fully paired duplex with blunt ends (B-duplex)

Strand 1: ACA GAT GCA CAT ATC GAG GTG GAC ATC ACTTAC GCT GAG TAC TTC GAA

Strand 2: TTC GAA GTA CTC AGC GTA AGT GAT GTC CAC CTC GAT ATG TGC ATC TGT

DNA duplex with 5-Poly T tail (Poly-T-duplex)

Strand 1: ACA GAT GCA CAT ATC GAG GTG GAC ATC ACT TAC GCT GAG TAC TTC GAA

Strand 2: TTT TT TTC GAA GTA CTC AGC GTA AGT GAT GTC CAC CTC GAT ATG TGC ATC TGT

Semi-capped DNA duplex (SC-duplex)

Strand 1: ACA GAT GCA CAT ATC GAG GTG GAC ATC ACT TAC GCT GAG TAC TTC GAA TTT TTT TCG AAG TAC TCA GCG TAA GTG ATG TCC ACC TCG ACA TGT GCA TCT GT

Fully-capped DNA duplex (FC-duplex)

Strand 1: GTC CAC CTC GAC ATG TGC ATC TGT TTT TTA CAG ATG CAC ATA TCG AGG TGG ACA TCA CTT ACG CTG AGT ACT TCG AAT TTT TTT TCG AAG TAC TCA GCG TAA GTG AT

Semi-capped DNA duplex with a G-C termination (SC-duplex GC)

Strand 1: GCA GAT GCA CAT ATC GAG GTG GAC ATC ACT TAC GCT GAG TAC TTC GAA TTT TTT TCG AAG TAC TCA GCG TAA GTG ATG TCC ACC TCG ACA TGT GCA TCT GC

FC-duplex with 1T as flexible part (FC-duplex-1T-flex)

Strand 1: GTC CAC CTC GAT ATG TGC ATC TGT TTT TTA CAG ATG CAC ATA TCG AGG TGG ACT AGC ACT TAC GCT GAG TAC TTC GAA TTT TTT TCG AAG TAC TCA GCG TAA GTG CT

All-DNA repulsive rods

DNA duplex capped with 5T tail on both ends (5T_100-duplex_5T)

Strand 1: TTT TTA CAG ATG CAC ATA TCG AGG TAC AGA TGC ACA TAT
CGA GGT ACA GAT GCA CAT ATC GAG GTA CAG ATG CAC ATA TCG AGG
TAC AGA TGC ACA TAT CGA GGT TTT TT

Strand 2: ACC TCG ATA TGT GCA TCT GTA CCT CGA TAT GTG CAT CTG
TAC CTC GAT ATG TGC ATC TGT ACC TCG ATA TGT GCA TCT GTA CCT
CGA TAT GTG CAT CTG T

Semi-capped DNA 60 base pairs long with 6T tail (SC-60-duplex_6T)

Strand 1: TTT TTT ATC AAC AGA GCC ACT TTG GCC CGC TGG TCG CCG
CTA TCG ACA GGC TCA ATG CTG GAG GGT TTT TTA CCC TCC AGC ATT
GAG CCT GTC GAT AGC GGC GAC CAG CGG GCC AAA GTG GCT CTG TTG
AT

Semi-capped DNA 48 base pairs long with 6T tail (SC-48-duplex_6T)

Strand 1: TTT TTT ACA GAT GCA CAT ATC GAG GTG GAC ATC ACT TAC
GCT GAG TAC TTC GAA TTT TT TTC GAA GTA CTC AGC GTA AGT GAT GTC
CAC CTC GAT ATG TGC ATC TGT

Semi-capped DNA 40 base pairs long with 6T tail (SC-40-duplex_6T)

Strand 1: TTT TTT ACA TAT CGA GGT GGA CAT CAC TTA CGC TGA GTA
CTT CGA ATT TTT TTC GAA GTA CTC AGC GTA AGT GAT GTC CAC CTC
GAT ATG T

Semi-capped DNA 36 base pairs long with 6T tail (SC-36-duplex_6T)

Strand 1: TTT TTT ATC GAG GTG GAC ATC ACT TAC GCT GAG TAC TTC
GAA TTT TTT TCG AAG TAC TCA GCG TAA GTG ATG TCC ACC TCG AT

Semi-capped DNA 33 base pairs long with 6T tail (SC-33-duplex_6T)

Strand 1: TTT TTT GAG GTG GAC ATC ACT TAC GCT GAG TAC TTC GAA
TTT TTT TCG AAG TAC TCA GCG TAA GTG ATG TCC ACC TC

Semi-capped DNA 30 base pairs long with 6T tail (SC-30-duplex_6T)

Strand 1: TTT TTT GTG GAC ATC ACT TAC GCT GAG TAC TTC GAA TTT TTT
TCGAAG TAC TCA GCG TAA GTG ATG TCC AC

Semi-capped DNA 28 base pairs long with 6T tail (SC-28-duplex_6T)

Strand 1: TTT TTT GGA CAT CAC TTA CGC TGA GTA CTT CGA ATT TTT TTC
GAA GTA CTC AGC GTA AGT GTC C

Semi-capped DNA 26 base pairs long with 6T tail (SC-26-duplex_6T)

Strand 1: TTT TTT GTC GAA GTA CTA CCA TGT GCA TCT GTT TTT TAC AGA
TGC ACA TGG TAG TAC TTC GAC

Semi-capped DNA 24 base pairs long with 6T tail (SC-24-duplex_6T)

Strand 1: TTT TTT YCG ACA GGC TCA ATG CTG GAGF GGT TTT TTA CCC
TCC AGC ATT GAG CCT GTC GA

Semi-capped DNA 20 base pairs long with 6T tail (SC-20-duplex_6T)

Strand 1: TTT TTT GCG TCC AGT CGC AGA TGC ACT TTT TGT GCA TCT GCG
ACT GGA CGC

Semi-capped DNA 33 base pairs long with 2T tail (SC-33-duplex_2T)

Strand 1: TTG AGG TGG ACA TCA CTT ACG CTG AGT ACT TCG AAT TTT
TTT CGA AGT ACT CAG CGT AAG TGA TGT CCA CCT C

All-DNA chain-sticks

Fully paired duplex

Strand 1: ACA GAT GCA CAT ATC GAG GTG GAC ATC ACT TAC GCT GAG
TAC TTC GAA TTT TTT TTT TTT TTT TTT TTA CAG ATG CAC ATA TCG AGG
TGG ACA TCA CTT ACG CTG AGT ACT TCG AA

Strand 2: TTC GAA GTA CTC AGC GTA AGT GAT GTC CAC CTC GAT ATG
TGC ATC TGT AAA AAA AAA AAA AAA AAA AAT TCG AAG TAC TCA GCG
TAA GTG ATG TCC ACC TCG ATA TGT GCA TCT GT

Chain-sticks with 4T as the flexible spacer (G_{4T}-duplex)

Strand 1: ACA GAT GCA CAT ATC GAG GTG GAC ATC ACT TAC GCT GAG
TAC TTC GAA TTTT ACA GAT GCA CAT ATC GAG GTG GAC ATC ACT TAC
GCT GAG TAC TTC GAA

Strand 2: TTC GAA GTA CTC AGC GTA AGT GAT GTC CAC CTC GAT ATG
TGC ATC TGT

Strand 3: TTC GAA GTA CTC AGC GTA AGT GAT GTC CAC CTC GAT ATG
TGC ATC TGT

Chain-sticks with 7T as the flexible spacer (G_{7T}-duplex)

Strand 1: ACA GAT GCA CAT ATC GAG GTG GAC ATC ACT TAC GCT GAG
TAC TTC GAA TTT TTT T ACA GAT GCA CAT ATC GAG GTG GAC ATC ACT
TAC GCT GAG TAC TTC GAA

Strand 2: TTC GAA GTA CTC AGC GTA AGT GAT GTC CAC CTC GAT ATG
TGC ATC TGT

Strand 3: TTC GAA GTA CTC AGC GTA AGT GAT GTC CAC CTC GAT ATG
TGC ATC TGT

Chain-sticks with 11T as the flexible spacer (G_{11T}-duplex)

Strand 1: ACA GAT GCA CAT ATC GAG GTG GAC ATC ACT TAC GCT GAG
TAC TTC GAA TTT TTT TTT TT ACA GAT GCA CAT ATC GAG GTG GAC ATC
ACT TAC GCT GAG TAC TTC GAA

Strand 2: TTC GAA GTA CTC AGC GTA AGT GAT GTC CAC CTC GAT ATG
TGC ATC TGT

Strand 3: TTC GAA GTA CTC AGC GTA AGT GAT GTC CAC CTC GAT ATG
TGC ATC TGT

Chain-sticks with 12T as the flexible spacer (G_{12T}-duplex)

Strand 1: ACA GAT GCA CAT ATC GAG GTG GAC ATC ACT TAC GCT GAG
TAC TTC GAA TTT TTT TTT TTT ACA GAT GCA CAT ATC GAG GTG GAC
ATC ACT TAC GCT GAG TAC TTC GAA

Strand 2: TTC GAA GTA CTC AGC GTA AGT GAT GTC CAC CTC GAT ATG
TGC ATC TGT

Strand 3: TTC GAA GTA CTC AGC GTA AGT GAT GTC CAC CTC GAT ATG
TGC ATC TGT

Chain-sticks with 15T as the flexible spacer (G_{15T}-duplex)

Strand 1: ACA GAT GCA CAT ATC GAG GTG GAC ATC ACT TAC GCT GAG
TAC TTC GAA TTT TTT TTT TTT TTT ACA GAT GCA CAT ATC GAG GTG GAC
ATC ACT TAC GCT GAG TAC TTC GAA

Strand 2: TTC GAA GTA CTC AGC GTA AGT GAT GTC CAC CTC GAT ATG
TGC ATC TGT

Strand 3: TTC GAA GTA CTC AGC GTA AGT GAT GTC CAC CTC GAT ATG
TGC ATC TGT

Purely repulsive chain-stick with 4T as the flexible spacer (G_{4T}-duplex-PolyT)

Strand 1: TTT TTT ACA GAT GCA CATATC GAG GTG GAC ATC ACT TAC GCT
GAG TAC TTC GAA TTTT ACA GAT GCA CAT ATC GAG GTG GAC ATC TAC
GCT GAG TAC TTC GAA TTT TTT

Strand 2: TTC GAA GTA CTC AGC GTA AGT GAT GTC CAC CTC GAT ATG
TGC ATC TGT

Strand 3: TTC GAA GTA CTC AGC GTA AGT GAT GTC CAC CTC GAT ATG
TGC ATC TGT

Purely repulsive chain-stick with 7T as the flexible spacer (G_{7T}-duplex-PolyT)

Strand 1: TTT TTT ACA GAT GCA CATATC GAG GTG GAC ATC ACT TAC GCT
GAG TAC TTC GAA TTT TTT T ACA GAT GCA CAT ATC GAG GTG GAC ATC
TAC GCT GAG TAC TTC GAA TTT TTT

Strand 2: TTC GAA GTA CTC AGC GTA AGT GAT GTC CAC CTC GAT ATG
TGC ATC TGT

Strand 3: TTC GAA GTA CTC AGC GTA AGT GAT GTC CAC CTC GAT ATG
TGC ATC TGT

Purely repulsive chain-stick with 11T as the flexible spacer (G_{11T}-duplex-PolyT)

Strand 1: TTT TTT ACA GAT GCA CATATC GAG GTG GAC ATC ACT TAC GCT
GAG TAC TTC GAA TTT TTT TTT TT ACA GAT GCA CAT ATC GAG GTG GAC
ATC TAC GCT GAG TAC TTC GAA TTT TTT

Strand 2: TTC GAA GTA CTC AGC GTA AGT GAT GTC CAC CTC GAT ATG
TGC ATC TGT

Strand 3: TTC GAA GTA CTC AGC GTA AGT GAT GTC CAC CTC GAT ATG
TGC ATC TGT

Purely repulsive chain-stick with 20T as the flexible spacer (G_{20T}-duplex-PolyT)

Strand 1: TTT TTT ACA GAT GCA CATATC GAG GTG GAC ATC ACT TAC GCT
GAG TAC TTC GAA TTT TTT TTT TTT TTT TT ACA GAT GCA CAT ATC
GAG GTG GAC ATC TAC GCT GAG TAC TTC GAA TTT TTT

Strand 2: TTC GAA GTA CTC AGC GTA AGT GAT GTC CAC CTC GAT ATG
TGC ATC TGT

Strand 3: TTC GAA GTA CTC AGC GTA AGT GAT GTC CAC CTC GAT ATG
TGC ATC TGT

Blunt-ended DNA with a five thymine base (5T) long non-sticky single stranded DNA tail (Poly-T-duplex)

A Poly-T-duplex is made of two partially complementary DNA strands, where one strand has additional 5 thymine bases which, during the process of annealing, stay unpaired and represents a hindrance of blunt-end stacking interactions in the form of a dangling tail. Gel PAGE electrophoresis (see section 2.1.3) was employed for the evaluation of the success of annealing.

Fully-capped DNA duplex with one unpaired thymine base

Fully-capped DNA constructs with a flexible part are made of one self-complementary strand which self-folds during the annealing process. The difference between fully-capped constructs and these is that these constructs have implemented 1T in the original sequence. This implemented T base has no complementary base pair and, therefore, provides some degree of flexibility to the system. They are assembled through the same thermal annealing protocol described for the previous two systems. In the case of this system, gel PAGE electrophoresis (see section 2.1.3) was used for evaluation of the success of annealing.

Semi-capped DNA with poly-T tails

Semi-capped DNA constructs with poly-T tails consist of one self-complementary strand that folds into the desired structure. It contains a 5T hairpin loop on one side and a poly-T tail(6T) on another. The hairpin loop behaves like a lid on one blunt end, while the poly-T tail behaves as a hindrance of blunt-end stacking interactions. The system is made through the same process of thermal annealing described in the previous paragraph. The success of annealing was estimated again with PAGE gel electrophoresis (section 2.1.3).

DNA capped with a five thymine base (5T) long single stranded DNA tail on both sides (5T_100-duplex_5T)

5T_100-duplex_5T is synthesized from two partially complementary strands, where one strand contains 5 additional thymine (5T) bases on each side, that do not have complementary counterparts in another strand. In this way we get a DNA construct where dangling poly-T tails are on both sides of a duplex, blocking blunt-ends interactions. The process of thermal annealing was the same like for all previously described systems. Information about the success of annealing was estimated again with PAGE gel electrophoresis (section 2.1.3).

All-DNA chain-sticks

All-DNA chain-sticks consist of one long single-strand, called sense, and two short single strands called antisense, which are complementary to the parts of the long one, mixed in the stoichiometric amounts 1:1:1. In this way two double-stranded regions are formed, which are connected through a flexible one-stranded spacer, for which no complementary strand is present. With the described synthetic approach, it is possible to control the length of the flexible spacer, as well as its position, at a level of a single base pair. Strands are assembled into a target structure through a described process of a thermal annealing. Gel electrophoresis was employed in the evaluation of the process (section 2.1.3).

Purely repulsive all-DNA chain-sticks

Purely repulsive all-DNA chain-sticks consist as well, of one long single-strand, called sense and two short single strands called antisense, which are complementary to the parts of the long one, mixed in the stoichiometric amounts 1:1:1. The difference from the previous system is that antisense strand in this case possess additional 6 thymine (6T) bases on both sides, which do not have a complementary counterpart in the antisense strands. In this way two double-stranded regions are formed, which are connected through a flexible one-stranded DNA spacer and additionally possess 6 poly-T dangling tails on both sides. The strands are assembled into a desired structure through a described process of thermal annealing. Gel electrophoresis was employed in the evaluation of the process (section 2.1.3).

2.3.4 Sample preparation

After annealing and evaluation of the samples, they were concentrated and the buffer was exchanged using Amicon (MWCO 3k) filters. Afterwards, the samples were evaporated to high concentration using Eppendorf SpeedVac Concentrator. The solutions ready to be loaded into capillaries and measured, were prepared by step-wise diluting with 1xTE/NaCl buffer. Starting from the most concentrated one to the most diluted one, the samples were thoroughly homogenized before being loaded into capillaries.

Bibliography

1. Angst, M. *Scattering! Soft, functional and quantum materials lecture notes of the 50th IFF Spring School 2019*. (2019).
2. Cates, M. E. & Evans, M. R. *Soft and Fragile Matter*. vol. 53 (Institute of Physics Publishing, Bristol and Philadelphia, 1999).
3. de Jeu, W. H. *Basic X-ray Scattering for Soft Matter*. (Oxford University Press, 2016).
4. Röntgen, W. C. On a new kind of rays. *Nature* **53**, 274 (1896).
5. This month in physics history November 8, 1895: Roentgen's Discovery of X-Rays. *American Physical Society* (2001).
6. Burke, J. E. & Butcher, S. E. Nucleic acid structure characterization by small angle X-ray scattering (SAXS). *Curr. Protoc. Nucleic Acid Chem.* 1–25 (2012) doi:10.1002/0471142700.nc0718s51.
7. Kentzinger, E., Krutyeva, M. & Rücker, U. GALAXI: Gallium anode low-angle x-ray instrument. *J. large-scale Res. Facil.* (2016).
8. Schnablegger, H. & Singh, Y. *The SAXS Guide*. (Anton Paar GmbH, 2017).
9. THE FIT2D HOME PAGE <https://www.esrf.fr/computing/scientific/FIT2D/>.
10. Lagerwall, J. P. F. *Structures and properties of the chiral smectic C liquid crystal phases: Ferro- and antiferroelectricity in soft matter*. *Doktorsavhandlingar vid Chalmers Tekniska Hogskola* (Chalmers University of Technology, Göteborg, 2002).
11. Dierking, I. *Textures of Liquid Crystals*. *Textures of Liquid Crystals* (Wiley, 2003). doi:10.1002/3527602054.
12. Nikon-Polarized light microscopy. <https://www.microscopyu.com/techniques/polarized-light/polarized-light-microscopy> (2021).
13. Drabik, A., Bodzoń-Kulakowska, A. & Silberring, J. Gel Electrophoresis. *Proteomic Profiling Anal. Chem. Crossroads Second Ed.* 115–143 (2016) doi:10.1016/B978-0-444-63688-1.00007-0.
14. Magdeldin, S. *Gel Electrophoresis - Principles and Basics*. *Gel Electrophoresis - Principles and Basics* (2012). doi:10.5772/2205.
15. Frenkel, D. & Smit, B. *Understanding Molecular Simulation*. (Academic Press, Inc., 2002). doi:10.1016/B978-0-12-267351-1.X5000-7.
16. Kroese, D. P., Breton, T., Taimre, T. & Botev, Z. I. Why the Monte Carlo method is so important today. *Wiley Interdiscip. Rev. Comput. Stat.* **6**, 386–392 (2014).

Chapter 3

Self-assembly of all-DNA rods with controlled patchiness

Double-stranded DNA fragments exhibit non-covalent attractive interactions between their terminal base-pairs. The importance of these blunt-end attractions in the formation of DNA liquid crystals still remains not fully understood. In this chapter we demonstrate how the tuning of these interactions at a molecular level can lead to the formation of different types of lyotropic smectic-A (Sm-A) mesophases. We constructed DNA duplexes with interruption of base-stacking interactions on one (semi-capped duplex, SC-duplex) or both ends (fully-capped, FC-duplex) with hairpin loops. As a direct consequence of these DNA terminal modifications, SC-duplexes and FC-duplexes in concentrated aqueous solutions self-assemble into bilayer Sm-A (Sm_b-A) and monolayer Sm-A (Sm_m-A) phases, respectively. Moreover, control over the terminal attraction strength in SC-duplexes reveals the stabilization of the columnar (Col) phase at the expense of the bilayer Sm-A. The existence of the above-mentioned smectic phases is confirmed by Monte-Carlo simulations of hard cylinders with controlled number of attractive terminal sites. Our results reveal that DNA blunt-ends behave as well-defined monovalent attractive patches whose strength and position can be potentially precisely tuned.

3.1 Introduction

Base-paired terminal sites of a DNA duplex are called blunt-ends. Blunt-end stacking interactions refer to the weak, non-covalent attractive interactions between blunt-ends of two DNA duplexes. The origin of these attractions arises from several non-covalent forces.¹ The same stacking forces between two adjacent base pairs within the DNA duplex^{2,3} and Watson-Crick base-pairing⁴ are the two most important contributors to the thermodynamic stability of the DNA helix. Researchers from different fields have studied the importance of blunt-end stacking interactions in biological and non-biological context.⁵⁻⁹ There is a clear evidence that base-stacking interactions influence DNA polymerase activities during the replication process, and thus affect the efficiency of DNA base-pair synthesis.⁵ Moreover, recent studies on self-assembly of concentrated aqueous solutions of blunt-ended short double-stranded DNA and RNA^{7,10} suggested that these interactions could play an important role in molecular evolution in prebiotic environments.

In a non-biological context, stacking interactions were used to create a specific recognition between different DNA origami units.⁸ Employing a principle of geometric arrangement of blunt-end stacking interactions, these DNA building blocks create diverse bonds with each other assembling into super-origami structures. Programming of these diverse links using a binary-code approach allowed their specificity, thermodynamics and binding rules to be easily explored. In addition, a recent pioneered work demonstrated how the use of these weak stacking interactions allows a dynamic assembly and disassembly of DNA origami units.⁹ Specifically, it was shown how three-dimensional (3D) DNA components can create various reversibly reconfigurable DNA devices with arbitrary shapes exploiting only the principle of base-stacking and shape-complementarity. Base-stacking interactions compete against electrostatic repulsion between DNA domains interfaces and stabilize these complex multidomain structures. Interestingly, without detailed sequence programming, it was possible to influence the conformation of these DNA multidomains by employing an allosteric regulation mechanism via competitive DNA strand displacement approach within a specified temperature window. Additional control was provided with the change of cation concentration.

Base-stacking interactions also play a key role in DNA lyotropic liquid crystal (LC) self-assembly. The ability of DNA duplexes to form LC ordered phases has been extensively studied since 1980s.^{11–15} It has been found that concentrated aqueous solutions of blunt-ended DNA duplexes, close to the persistence length l_p (~150bp), undergo a spontaneous transition from isotropic (I) to chiral nematic (N^*) LC phase. The same studies also reveal that, depending on the length of the duplex and the sample preparation method, further increase of the DNA concentration leads to formation of the columnar hexagonal (Col) phase and, finally, to true crystal phases. The formation and the thermodynamic stability of these phases can be understood in terms of entropy-driven ordering, which arises from a predisposition of repulsive rigid or semi-flexible rod-shaped polymers to minimize the macromolecular excluded volume. This conceptual framework has been provided by the seminal work of Onsager¹⁶ (for more details, see chapter 1). Molecular theories^{16,17} and computer simulations^{18–21} on repulsive hard spherocylinders predicted the appearance of LC ordering for aspect ratios down to $L/D \approx 4.7$ (L is the length of the rod, and D is the diameter), while for lower aspect ratios, LC phases are not expected to occur. However, experiments showed the formation of LC phases in aqueous solutions of ultra-short DNA helices above a critical concentration.¹⁰ These rod-like, blunt-ended DNA helices with aspect ratio in the range $1 < L/D < 3.5$ exhibited a transition from I to N^* above a critical concentration. The main hypothesis for this unusual finding was the existence of blunt-end stacking interactions which drive duplexes to stuck on top of each other and by that form linear aggregates, which are polydisperse in length, stiff and long enough to form N^* phase. This conclusion was inspired by early works on lyotropic chromonic liquid crystal phases (LCLC), which are a special class of lyotropic mesophases markedly different

from the conventional amphiphilic mesogens.^{22,23} Materials forming LCLCs are composed of flat molecules with a polyaromatic central core and hydrophilic ionic groups at the periphery. The basic building block of LCLCs is a molecular stack in which the molecules are arranged face-to-face into columns with the ionic groups exposed at the water-column interface.²³ However, the stacking forces involved in the formation of the DNA columns are much weaker than in the case of the chromonics^{24,25}, leading to a formation of linear semi-flexible aggregates.¹⁰

The importance of the same stacking attractions was highlighted as a key mechanism for the formation and stabilization of the folded Sm-A phase in the solutions of blunt-ended all-DNA molecules with chain-stick architecture (gapped-DNA duplexes).²⁶ In this work, it is shown that Sm-A forms with increasing DNA flexibility by inserting an unpaired single-stranded DNA spacer in the middle of the duplex backbone. This is unusual because flexibility typically destabilizes the smectic phase.^{27–32} It is suggested that by incorporating a sufficiently long, flexible ssDNA spacer in the middle of the DNA duplex, these chain-stick molecules are able to attain a folded conformation within the smectic layers, forming a bilayer structure. In this morphology, the folded gapped-duplexes stack on top of each other through their attractive tips (blunt-ends). Such a molecular packing allows “self-protection” of the attractive DNA blunt-ends and suppresses the formation of polydisperse linear aggregates. This suppression is necessary in order to form equally thick layers which are prerequisite for such two-dimensional fluid layered phase to occur. The proposed scenario is confirmed by MC simulations of two linked hard cylinders decorated with attractive terminal sites.

The above discussed findings suggest that DNA blunt-ends could be seen as discrete, monovalent attractive sites. This raises a question whether DNA can be considered as a true anisotropic patchy particle with a possibility to engineer the patchy valence by suppression of end-to-end interactions on one or both attractive sites. In order to explore this possibility, we screened blunt-end stacking interactions by modifying the tips of the DNA duplexes (B-duplex, **Figure 3.1**) with different steric hindrances^{33,34}, and observe how it would affect the liquid crystalline behaviour. We used monodisperse, stiff and short dsDNA fragments with aspect ratio $L/D = 8.1$ and stiffness $L/l_p \sim 0.32$ (l_p is the persistence length of the DNA, 150 base pairs (bp)). In these systems L corresponds to the duplex length (48bp), while D corresponds to the geometrical diameter of DNA duplex. Based on simulations and experimental studies, repulsive, rod-like particles with such a degree of anisotropy and rigidity are expected to form various LC phases at sufficiently high concentrations^{19–21}, including a smectic phase.^{35–37} At this point, it is particularly important to emphasize that the absence of smectic phase in DNA rod-like liquid crystals is still not fully understood.

More specifically, we modified blunt-end stacking interactions on one or both sides by following two approaches: in the first approach a five (5) thymine (T)-base long non-sticky single stranded DNA tail was introduced on one end of blunt-ended DNA duplex (Poly-T-duplex, see **Figure 3.1**); in the second approach a 5T long hairpin loops

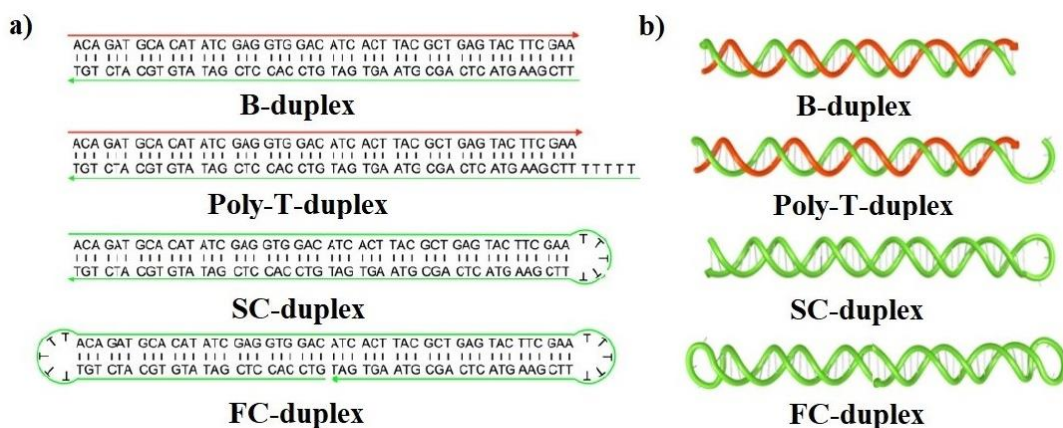


Figure 3.1 a) Schematic drawings of the DNA duplexes used for the study of LC behaviour of rod-shaped molecules with tuneable end-to-end stacking interactions. The sequences of the strands are also shown and different strands are represented with different colours. The DNA duplexes are 48bp long. From the top to the bottom: Blunt-ended DNA duplex (B-duplex); DNA duplex with 5 thymine (T) bases long tail (Poly-T-duplex); DNA duplex semi-capped by 5T hairpin loop on one end (SC-duplex) and DNA duplex fully-capped by 5T loop at both ends (FC-duplex). **b)** From the top to the bottom: The schematic cartoons of B-duplex, Poly-T-duplex, SC-duplex, FC-duplex are created with NUPACK analysis software.

were formed when the single-stranded DNA self-folds, through intramolecular base pairing, into a duplex with one or both ends capped by these hairpin loops. **Figure 3.1a** shows schematic drawings of our synthesized systems, blunt-ended duplex (B-duplex), duplex with 5-polyT tail (Poly-T-duplex), DNA duplex with a hairpin loop on one end (semi capped, SC-duplex) and DNA duplex with hairpin loops on both ends (fully-capped, FC-duplex). Schematic cartoons of these systems, designed with NUPACK analysis software³⁸, are depicted in **Figure 3.1b**. More details about the synthesis of these systems are provided in section **2.3.3**. Poly T sequence for tails and loops was the obvious choice due to the lack of tendency to form the secondary structures.³⁹ The Poly T sequence is chosen over the Poly A due to the fact that base stacking is the weakest (or almost absent) among thymines (T) and the strongest among adenines (A). Therefore, Poly T is expected to be closer to a random coil form.⁴⁰ Concerning the length of the hairpin loop, despite the fact that a four-base loop is close to the minimum sterically accepted length, in our work a 5T base long loop is chosen as a fair compromise for a stable folding, without altering the rod-like character of our DNA duplexes. B-duplex, Poly-T-duplex, SC-duplex, and FC-duplex can be distinguished in the native PAGE gel electrophoresis experiments based on the differences in their migration pattern, which is shown in **Figure 3.2**. Poly-T-duplex, SC- and FC-duplex demonstrate decreasing mobility compared to B-duplex because of the terminal modifications. The presence of only one band in each lane confirms the success of our synthesis.

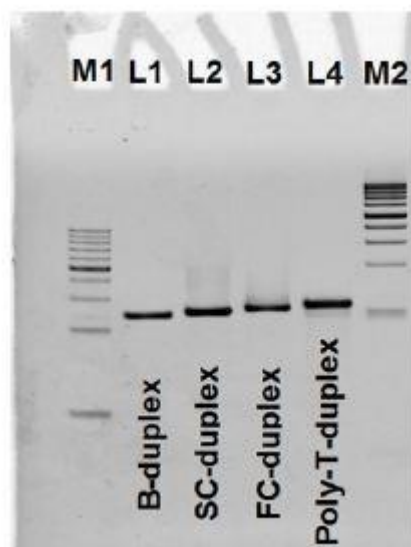


Figure 3.2 10% native PAGE gel electrophoresis of the synthesized systems. Lanes M1 and M2 contain 20bp and 50bp DNA ladder, respectively. Lanes L1 to L4 correspond to the following systems – L1 (B-duplex); L2 (SC-duplex); L3 (FC-duplex); L4 (Poly-T-duplex)

3.2 Effects of blunt-end stacking suppression on DNA LC ordering

We investigated the self-assembly behaviour of above-mentioned DNA systems using small angle X-ray scattering (SAXS) and polarized optical microscopy (POM). More details about these techniques can be found in the Methods section 2.1. The one-dimensional (1D) SAXS profiles for B-duplex, are shown in [Figure 3.3](#). We observed the expected LC phase sequence for a rod-like DNA. By increasing the concentration, B-duplex exhibits the first order transition from I (177.01 mg/ml; see [Figure 3.3d](#)) to N^* (256.9 mg/ml; green line in [Figure 3.3c](#)) phase, where I/N^* phase coexistence appears at a total concentration of 184.45 mg/ml (see the red SAXS curve, that corresponds to birefringent bottom part of the coexistent sample in [Figure 3.3c](#)). The samples around biphasic I/LC transition, observed under cross-polarizers, are presented in the inset of the panel **a**, in [Figure 3.3](#), where the most left and the most right samples are isotropic at 177.0 mg/ml and fully birefringent at 205.1 mg/ml, respectively, while the two samples in the middle are in the biphasic I/LC transition at total DNA concentrations of 184.5 mg/ml and 192.7 mg/ml, respectively.

The 1D-SAXS profiles are obtained by radially averaging the recorded 2D-scattering patterns. An example of such pattern can be seen in [Figure 3.4](#). All the profiles around the coexistence region are characterized by a single, broad peak with a maximum value of the scattered intensity located at scattering wave vector (q) value above 1nm^{-1} . By

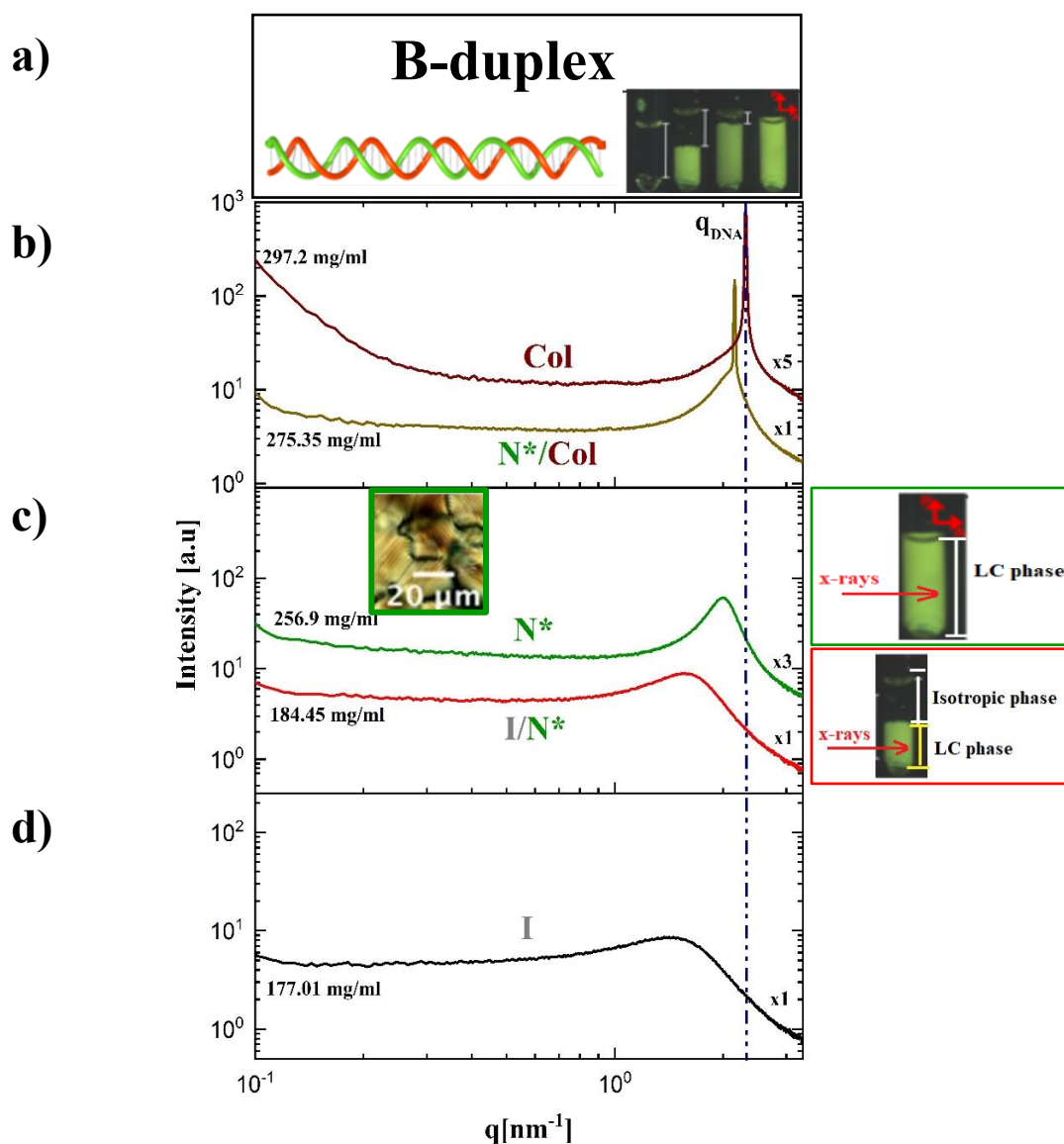


Figure 3.3 **a)** A schematic representation of the B-duplex. Concentrated B-duplex samples, loaded into 2mm glass capillaries for the SAXS studies, between cross-polarizers in the vicinity of I/N*; total DNA concentrations from left to right 177.0 mg/ml, 184.5 mg/ml, 192.7 mg/ml and 205.1 mg/ml. The white line indicates the height of the isotropic phase. **b)** 1D-SAXS profiles that correspond to Col ordering (the dark brown SAXS curve, 297.2 mg/ml) and to N*/Col coexistence (the light brown SAXS curve, 275.35 mg/ml). The blue dashed line enables easier observation of the concentration dependence of the sharp high q peak (q_{DNA}). **c)** The green SAXS curve corresponds to the one-phase N* (see the green rectangle on the right) with concentration of 256.9 mg/ml. Inset: the POM micrograph shows a typical fingerprint texture. The red SAXS curve is taken from the bottom birefringent region of the coexistent sample (see the red rectangle on the right, where the red arrow represents the location of X-rays through the birefringent part of the sample and the white and yellow bars indicate the height of the isotropic and LC regions, respectively), which corresponds to the total DNA concentration of 184.45 mg/ml. **d)** 1D-SAXS profile of the one-phase I at concentration 177.01 mg/ml

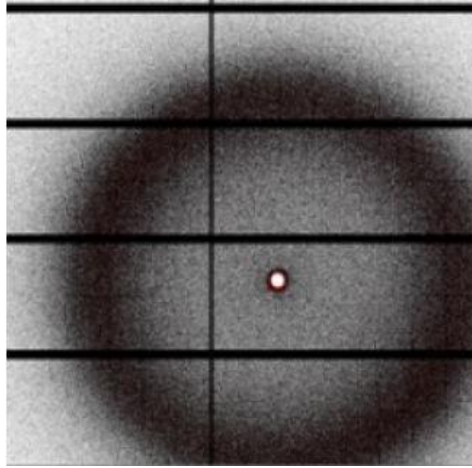


Figure 3.4 2D X-ray scattering pattern of the bottom birefringent phase, of the coexistent B-duplex sample, at the total DNA concentration of 184.5 mg/ml.

increasing the concentration above the coexistence region (184.5 mg/ml; red line in **Figure 3.3c**) to N^* (256.9 mg/ml; green SAXS curve in **Figure 3.3c**), we observe a shift of the q-peak towards higher values and a slight narrowing. Its broad character and corresponding spatial correlation values ($2\pi/q_{DNA} \approx 0.3 \text{ nm}$) indicate the presence of a liquid-like positional order between neighbouring, parallel DNA helices. Additionally, a fingerprint texture characteristic for N^* phase, with a cholesteric pitch of $2 \mu\text{m}$, was observed using POM. A further increase of the concentration up to 275.3 mg/ml (see **Figure 3.3b**; the light brown curve) leads to the appearance of one intense and narrow X-ray Bragg reflection superimposed on the broad peak. This SAXS feature can be identified as a structural signature of the coexistence between N^* and another higher-ordered LC crystal phase. At the concentration of 297.2 mg/ml, only the sharp scattering peak at high q-values is observed (see **Figure 3.3b**; the dark brown curve). In accordance with x-ray scattering experiments on polydisperse blunt-ended DNA duplexes with length close to its persistence length of 150 bp^{12,13}, the above-mentioned intense and sharp Bragg peak reflects a strong positional order between neighbouring DNA duplexes which corresponds to the formation of *Col*. However, no sign of smectic ordering is detected. The absence of the smectic phase in solutions of rod-like particles with a sufficient shape anisotropy can be explained in terms of particle flexibility and/or length polydispersity. For the synthesis of our systems, we are using synthetic single stranded DNA sequences, therefore our systems are monodisperse in length. They also have a significant stiffness ($L/l_p \sim 0.32$) and anisotropy ($L/D > 8$). The monodispersity, stiffness and an aspect ratio are the three key parameters for the stabilization of the smectic phase. Our system fulfils these three criteria, therefore, the absence of the smectic phase could be attributed to an effective length polydispersity mediated by the blunt-ends, which allowed the formation of linear aggregates. Previous studies showed that single stranded DNA overhangs can interrupt blunt-end stacking interactions¹⁰, therefore, the suggested modifications of B-duplex shown in **Figure 3.1**

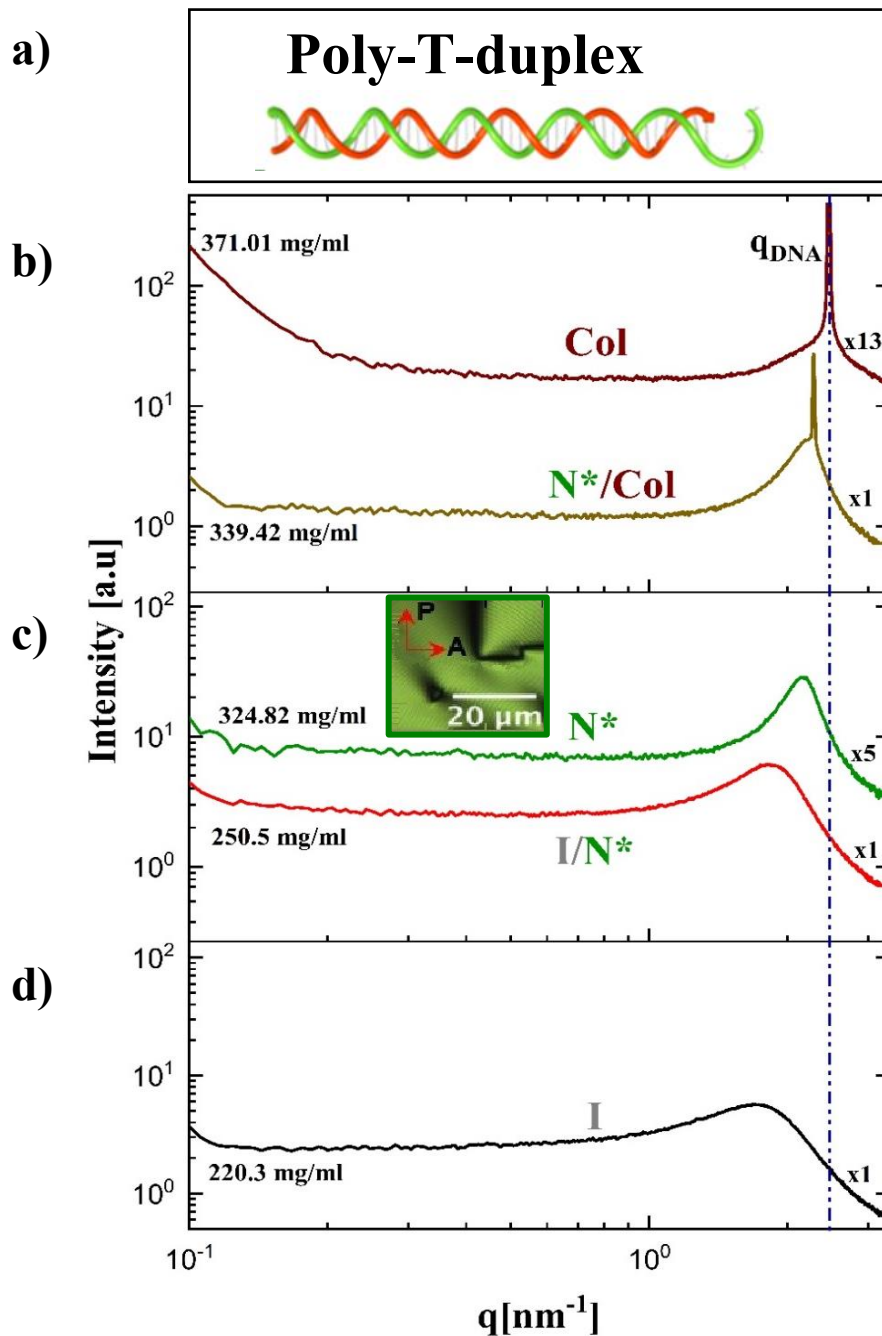


Figure 3.5 **a)** A schematic cartoon of the Poly-T- duplex. **b)** 1D-SAXS profiles that correspond to Col ordering in Poly-T-duplex solutions (dark brown SAXS curve, 371.01 mg/ml) and to the coexistence between N* and Col phase (light brown SAXS curve, 339.42 mg/ml). The dark blue dashed line enables an easier observation of the concentration-dependence of the sharp high q_{DNA} peak. **c)** The green curve corresponds to the one-phase N* with a concentration of 342.82 mg/ml. The inset in the green square shows the corresponding POM image, where a fingerprint texture is observed. The red SAXS curve is taken from the birefringent region of the coexistent sample with the total DNA concentration of 250.5 mg/ml. **d)** 1D-SAXS profile at the concentration of 220.3 mg/ml corresponding to the I phase of Poly-T-duplex

are expected to control the effective length polydispersity and lead to the formation of dimers (Poly-T-duplex, SC-duplex) and monomers (FC-duplex), which could pack into uniform smectic layers.

In the case of Poly-T-duplex, the concentration-dependent LC phase behaviour is similar to the B-duplex one. 1D-SAXS profiles for Poly-T-duplex are shown in **Figure 3.5**. At the concentration of 371.01 mg/ml (see **Figure 3.5b**; the dark brown curve), we notice one intense and sharp q_{DNA} peak at high q values, which is an indication of a *Col* phase. Decreasing the concentration to 339.4 mg/ml, the q_{DNA} peak shifts to lower q values and one broad peak appears on the shoulder of the narrow one (**Figure 3.5b**; the light brown curve). This indicates a coexistence of a *Col* and a less ordered phase. Further decreasing of concentration to 250.5 mg/ml, at almost the same q position, only a broad peak remains, which indicates the presence of a N^* phase (**Figure 3.5c**; represented with the green curve). The chiral nature of the nematic phase is confirmed by POM, where a typical cholesteric structure is observed. This micrograph of the Poly-T-duplex is shown in the green squared inset in **Figure 3.5c** above the green curve. Therefore, we identified the concentration of 339.4 mg/ml (**Figure 3.5b**; the light brown line) as the coexistence of N^* and *Col*. *I* phase is finally reached at the concentration of 220.3 mg/ml (**Figure 3.5d**). Two scenarios are possible in order to explain the absence of smectic phase in the Poly-T-duplex system. Either 5T tails were not effective enough in screening blunt-ends interactions, or there is a partial dimerization which is not enough to create a smectic phase.

However, the second scenario must be rejected since the hairpin loop seems to be effective in suppressing the end-stacking interactions. When we compare the concentration-dependant SAXS profiles of the SC-duplex with previously described systems (B-duplex and Poly-T-duplex), we can observe a significant difference in the concentration-dependant LC phase behaviour. In **Figure 3.6b**, at the concentration of 380.9 mg/ml, the 1D-SAXS profile indicates the formation of a *Col* phase. With decreasing of the concentration down to 310.5 mg/ml, we observe an intense principal peak at wave vector q^* , followed by several higher-order reflections with wave vector ratios q/q^* of 1:2:3:4 (see **Figure 3.6c**; the dark blue curve). These higher-order reflections indicate the formation of a type of smectic phase (*Sm*). From the position of the principal peak q^* , we can calculate the distance between adjacent layers:

$$d = \frac{2\pi}{q^*} = 35.6 \text{ nm}$$

The calculated value corresponds approximately to the length of two SC-duplexes. This strongly implies a bilayer-like packing scenario within the smectic layers. SC-duplexes are arranged in a coaxial stacking manner, where they are in contact with their blunt ends, forming aggregates of only two molecules (dimers). The proposed molecular scenario can be seen in **Figure 3.7a**. At the concentration of 290.3 mg/ml (**Figure 3.6d**, the green curve) the presence of the N^* was confirmed using the POM.

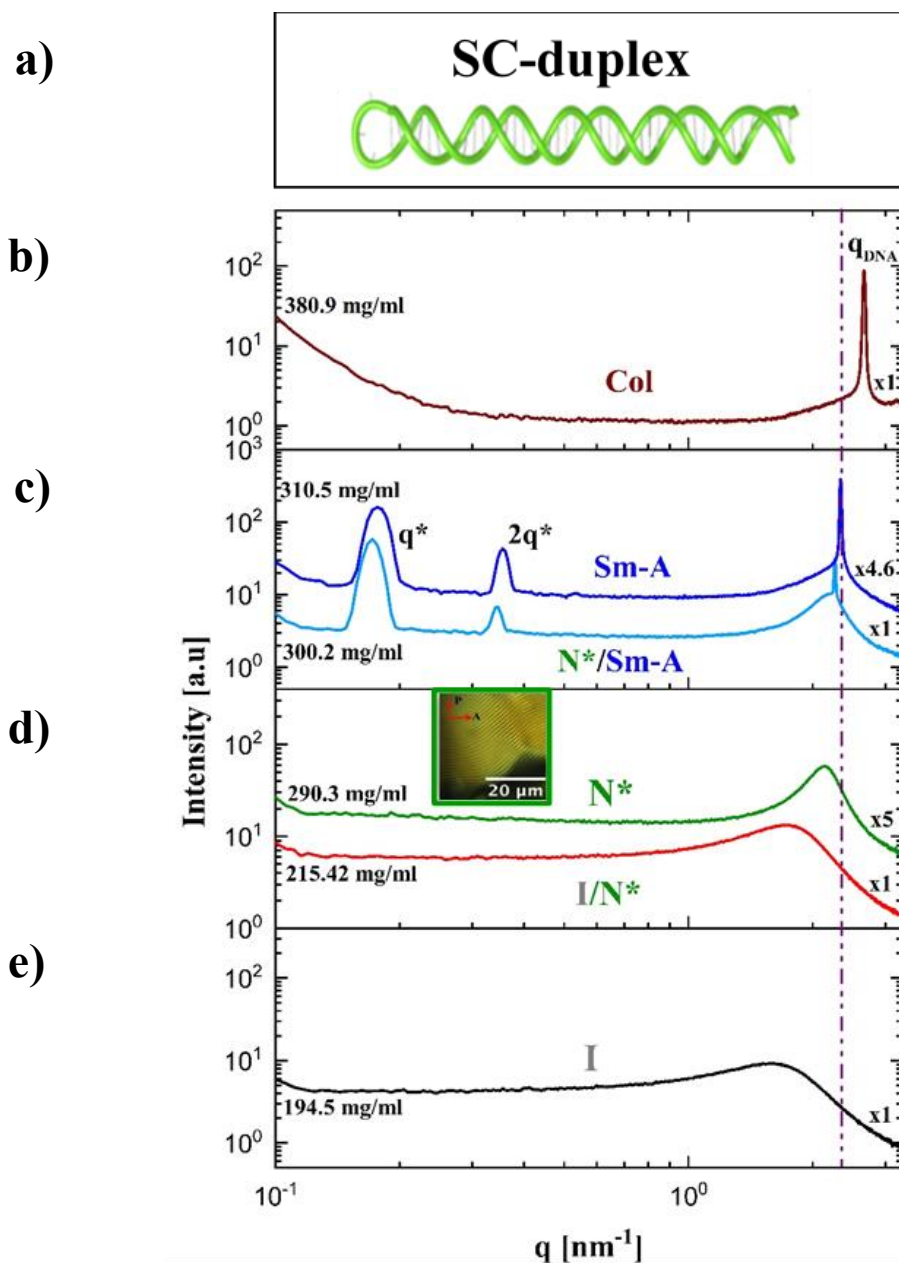


Figure 3.6 **a)** A schematic representation of the SC-duplex system **b)** 1D-SAXS profile of concentration 380.9 mg/ml that corresponds to Col ordering in SC-duplex. The purple dashed line across the whole figure enables an easier observation of the concentration dependence of the sharp high q_{DNA} . **c)** The dark blue curve at the concentration of 310.5 mg/ml shows a typical smectic x-ray scattering profile and corresponds to Sm-A type of ordering, while the light blue one, at the concentration of 300.2 mg/ml, shows the coexistence between broad and sharp high q peak and corresponds to $N^*/Sm-A$ ordering **d)** The green curve corresponds to the one-phase N^* with the concentration of 290.3 mg/ml. The inset shows a POM micrograph of this concentration, where a fingerprint texture is observed. The red SAXS curve is taken from the birefringent region of the coexistent sample which corresponds to the total DNA concentration of 215.42 mg/ml **e)** 1D-SAXS profile of the SC-duplex at the I phase with the concentration of 194.5 mg/ml.

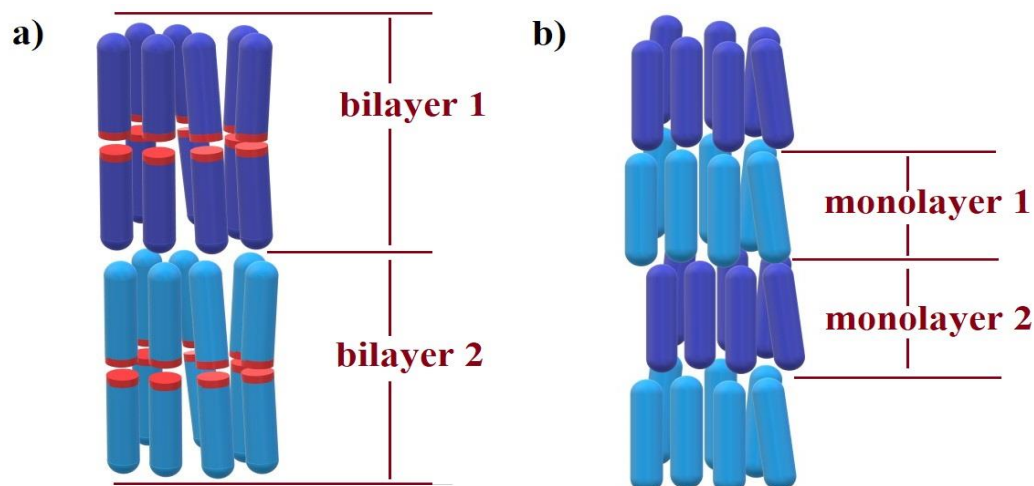


Figure 3.7 **a)** Schematic representation of the SC-duplexes self-assembly into bilayer *Sm-A* type of mesophase. SC-duplexes are arranged in coaxial stacking manner within a single layer, through the contact of their blunt ends (marked red), forming dimers. **b)** Schematic representation of the FC-duplexes self-assembly into monolayer *Sm-A* type of mesophase. Layers consist of single FC-duplexes. The layers (bilayers and monolayers) are marked with the numbers 1 and 2 and the duplexes in these layers are of different shades of blue just for the sake of better distinguishing and understanding the proposed packing scenarios.

The corresponding fingerprint texture of the sample is shown in the **Figure 3.6d** in the green square. The concentration of 300.2 mg/ml, where one sharp peak is superimposed on the broad one, indicates the N^*/Sm coexistence (**Figure 3.6c**; the light blue curve). The type of smectic phase can be determined by observing the 2D-SAXS patterns of the shear-aligned sample. This alignment is achieved by flow during the loading of samples

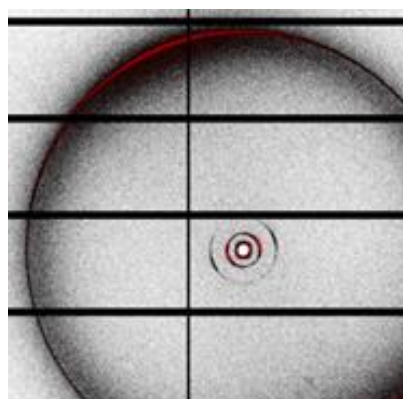


Figure 3.8 2D-SAXS pattern of the SC-duplex shear-aligned sample at the concentration of 300.2 mg/ml. The arcs close to the beam stop correspond to the correlations in the SC-duplex length, while the outer one corresponds to correlations in the duplex diameter. The fact that these two set of arcs are oriented perpendicular to each other, implies that the system self-assembled in *Sm-A* type of mesophase.

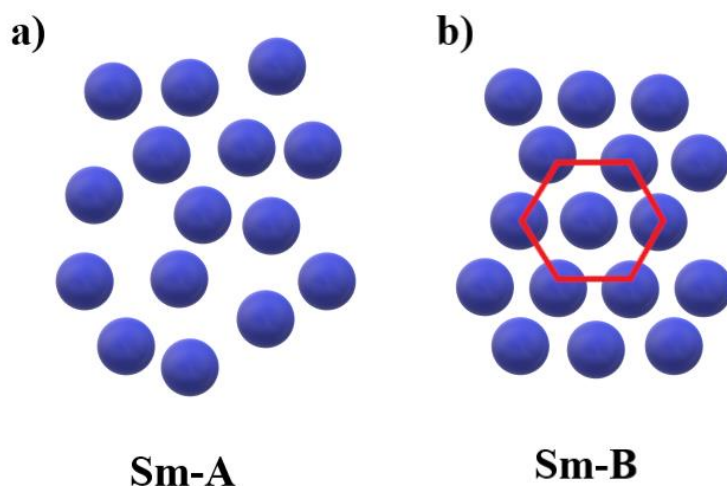


Figure 3.9 A schematic representation of the two different types of smectic structure viewed down along the duplex axis: a) *Sm-A*: close packed array of SC-duplex dimers with liquid-like ordering b) *Sm-B*: close packed array of SC-duplex dimers with hexagonal ordering

into capillaries and the corresponding 2D-SAXS pattern is presented in **Figure 3.8**. From the relative orientation of the inner arcs (close to the beam stop, which correspond to the q^* , $2q^*$ smectic peaks in the 1D-SAXS profile), and outer arc (the outer broad ring, which corresponds to the high q_{DNA} peak in the 1D-SAXS profile) we can conclude about the type of smectic mesophase in which the system is ordered. The inner arcs, which are close to the beam stop, originate from the correlations in the SC duplex length, while the outer arc corresponds to the correlations in the duplex diameter. Since these two sets of arcs are exactly perpendicular to each other, this implies that the type of internal organization is such that the SC-duplex dimers are oriented parallel to the layer's normal, which corresponds to the *Sm-A* mesophase (**Figure 3.8**). However, the narrowness of the q_{DNA} peak, at the concentration 310.5 mg/ml in **Figure 3.6c** (the dark blue curve), indicates a strong positional correlation between neighbouring SC-duplex within the smectic layers. This could be possibly associated with a hexagonally close-packed arrangement of SC-duplex dimers within the layers, so called *Sm-B* ordering (**Figure 3.9b**). However, a further investigation is needed to confirm this hypothesis.

The concentration-dependant SAXS profiles of the FC-duplex (see **Figure 3.10**) showed the phase transition sequence from *I* (262.2 mg/ml (**Figure 3.10d**)), over *I/N** at 274.2 mg/ml (red curve in **Figure 3.10c**), to *N** (325.4 mg/ml; green curve in **Figure 3.10c**). Further increase of the concentration, leads to *Sm* at 355.1 mg/ml (see the dark blue curve in the middle in **Figure 3.10b**) with the *N*/Sm* coexistence at the concentration of 335 mg/ml. The latter is characterized by the coexistence of a broad and a sharp q_{DNA} peak shown in **Figure 3.10b** (light blue curve; first from the bottom). This concentration-driven multiple order-to-order transition sequence is similar to the one of the SC-duplex. From the 1D-SAXS profile for smectic phase (**Figure 3.10b**), the

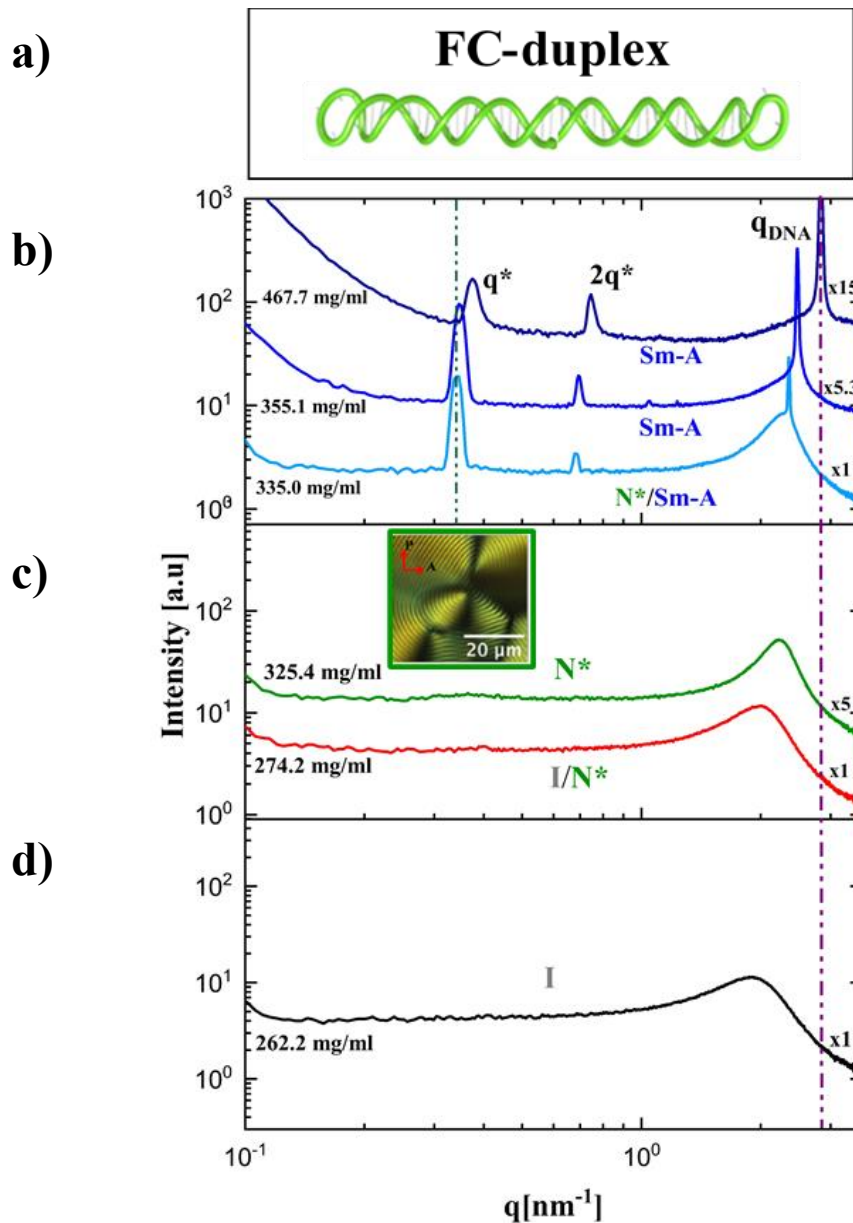


Figure 3.10 **a)** A schematic representation of the FC-duplex **b)** 1D-SAXS scattering profiles where the first from the top (navy blue curve) corresponds to a highly concentrated FC-duplex solution at 467.7 mg/ml, showing that the smectic phase persists till very high concentrations. At the concentration of 355.1 mg/ml (middle dark blue line) the Sm-A persists, accompanied with higher order reflections which suggest a long-range ordered structure. The bottom scattering profile (light blue) shows the coexistence of a broad and a narrow high q peak, corresponding to the $N^*/\text{Sm-A}$ coexistence at the concentration of 335.0 mg/ml. The dark green dashed line enables an easier observation of the concentration dependence of the q^* peak while the purple one enables easier observation of the concentration-dependence of the high q_{DNA} peak. **c)** The green SAXS curve corresponds to the one-phase N^* with the concentration of 325.4 mg/ml. The inset shows the corresponding POM micrograph, where a fingerprint texture is also observed. The red SAXS curve is taken from the birefringent region of the coexistent sample which corresponds to the total DNA concentration of 274.2 mg/ml. **d)** 1D-SAXS profile corresponding to the I phase at the concentration of 262.2 mg/ml.

position of the principal q^* peak corresponds to a layered structure, with the distance between adjacent layers calculated as follows:

$$d = \frac{2\pi}{q^*} = 18.3 \text{ nm}$$

This value is equal to the length of one FC-duplex. Based on this we can conclude that the layers are built from single FC-duplexes. A schematic representation of this monolayer smectic ordering is shown in the [Figure 3.7b](#). This finding also supports the molecular packing scenario of SC-duplex suggested earlier in [Figure 3.7a](#) and highlights the importance of blunt-end stacking interactions in DNA self-assembly. Another interesting observation is the shift of the smectic peaks towards higher values (see the dark green dashed line in [Figure 3.10b](#)) by increasing the concentration. A weak concentration dependence of the layer spacing is observed, where the spacing changes from 18.3 nm to 16.8 nm when increasing the concentration from 335 mg/ml to 467.7 mg/ml. This shrinkage in the smectic layer spacing can be attributed to the compression of the flexible hairpin loops upon increasing the SC-duplex density. Finally, worthy of mention is the fact that, in the case of FC-duplex, we couldn't detect the presence of the *Col* phase even at very high concentrations (467.7 mg/ml; see the first from the top, navy blue curve in the [Figure 3.10b](#)). However, we cannot exclude the possibility that the *Col* phase could be present even though we approached to a very high DNA density.

3.3 Phase behaviour of all-DNA rods with different terminal modifications

Phase transitions for all-DNA rods with aspect ratio $L/D \approx 8.1$, bending flexibility $L/l_p \approx 0.32$ and different terminal modifications (B-, Poly-T-, SC- and FC-duplex) are presented in the phase diagram of **Figure 3.11**. SAXS measurements and POM micrographs allow us to identify the different LC phases. At low concentration DNA, below 175 mg/ml, all systems are isotropic and a first order transition from I to N^* is present in all of them. However, modifications of the blunt-end attractive sites cause a shift of the transition boundaries. Comparing the phase behaviour of B- and SC- duplex, we notice that the I/N^* coexistence, marked red in **Figure 3.11**, is shifted towards higher DNA concentrations. Fully blocking the blunt-end attractions in the case of FC-duplex

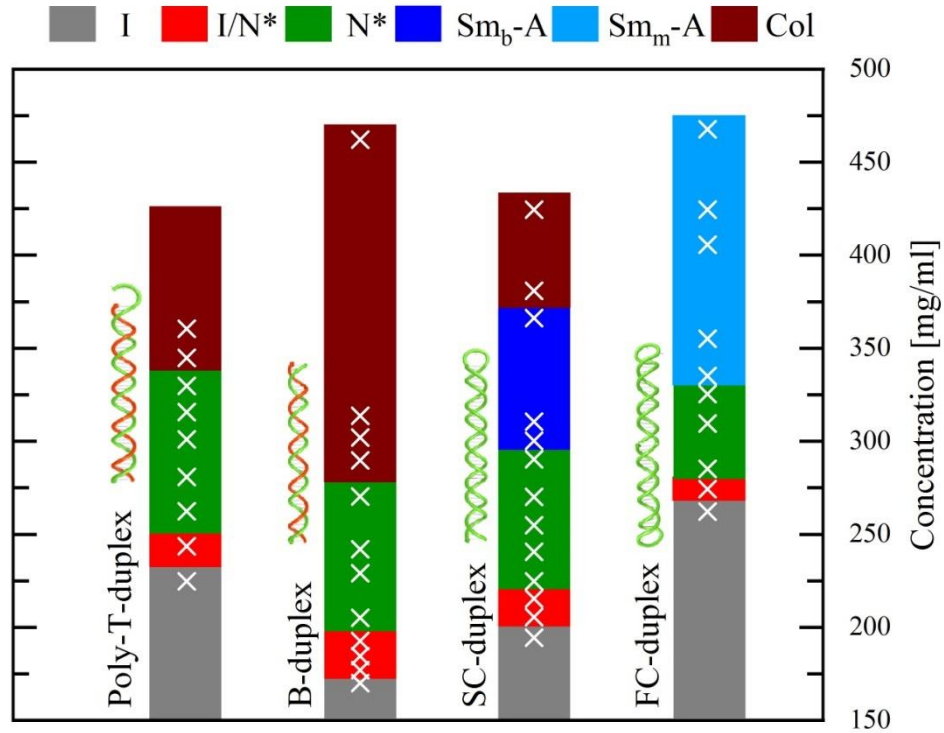


Figure 3.11 Phase diagram of DNA duplexes with various terminal modifications. Phase diagrams for the B-, Poly-T-, SC-, FC-duplex with $L_{DNA} = 48$ bp as a function of total DNA concentration. The coloured regions correspond to different LC phases, in accordance to the colour code given above the diagram. The white markers indicate the concentrations of the samples that were loaded in the capillaries for SAXS measurements. Phase identification and determination of the boundaries between the coloured regions were carried out by the combination of SAXS experiments, the visual inspection of the capillaries between cross-polarizers and the recording of the optical textures as observed by POM.

results in a further shift of I/N^* coexistence towards higher DNA concentrations, with respect to both SC- and B-duplex. This could be explained in terms of the reduction of the molecular elongation. It is expected that I/N^* transition will be postponed to higher concentrations as the effective molecular elongation decreases.^{19,21,41} To demonstrate this, we also synthesized a SC-duplex with half-duplex length (24 bp long). The influence of molecular elongation in the location of I/N^* transition in the SC-duplex is demonstrated in **Figure 3.12**, where the phase behaviour of SC-duplex 48 bp long is compared with the one of the 24 bp long. While this phase diagram encompasses the same sequence and type of phase transitions, the position of the I/N^* transition clearly shifts to larger values of the DNA concentration. In addition to the shift of the transition boundaries in the case of SC- and FC-duplex, we observe a noticeable shrinkage of the I/N^* coexistence region (see the width of the red regions in **Figure 3.11**). This can be interpreted in terms of length polydispersity since a decrease of the system's

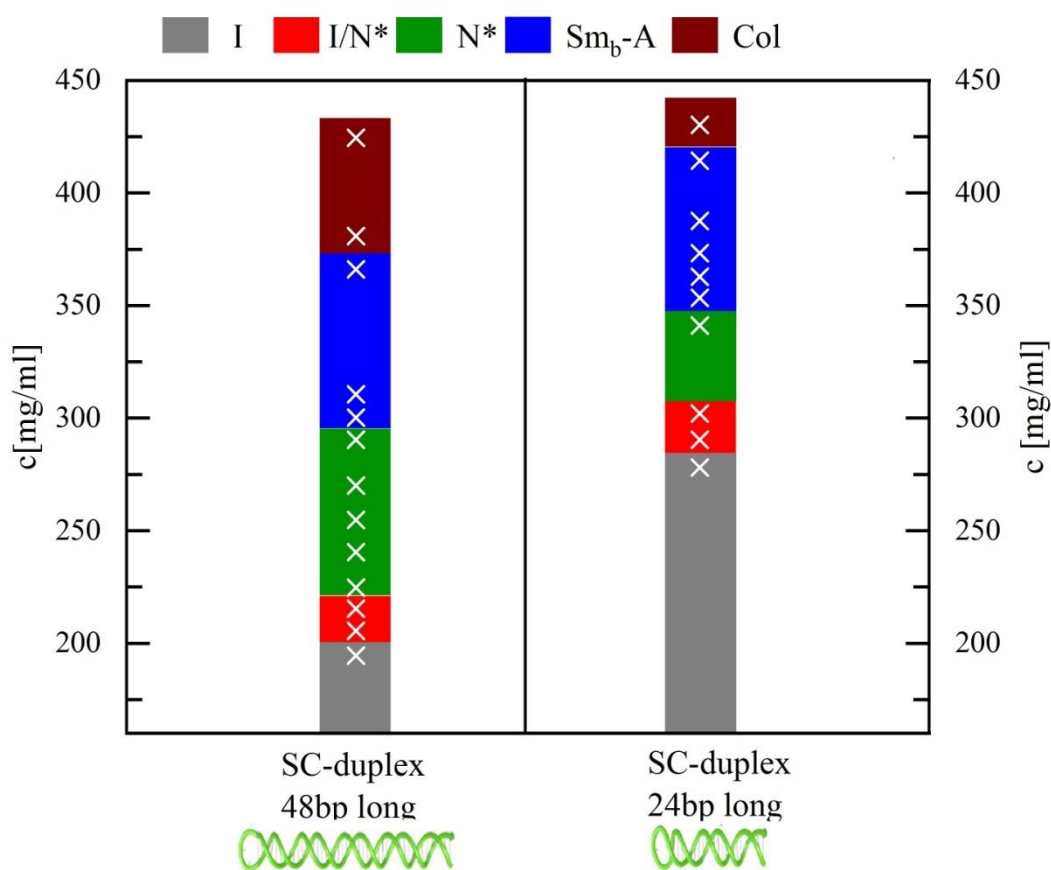


Figure 3.12 Phase diagrams for the SC-duplex $L_{dsDNA}=48bp$ (left side) and SC-duplex $L_{dsDNA}=24bp$ (right side) as a function of the total DNA concentration. Different LC phases are marked with different colours, in accordance to the colour code given above the diagram. The white markers indicate the samples that were loaded into capillaries for SAXS measurements. Phase identification and determination of the boundaries between the coloured regions were carried out by the combination of SAXS experiments, the visual inspection of the capillaries between cross-polarizers and the recording of the optical textures as observed by POM.

polydispersity results in a narrowing of the coexistence region.^{42–47} Indeed, the partial or full shielding of these monovalent terminal attractions in B-duplex significantly disturbs the formation of polydisperse linear aggregates, resulting in the formation of dimers (SC-duplex case) or monomers (FC-duplex case). Interestingly, the results of Poly-T duplex show a narrowing of the I/N^* phase (see **Figure 3.11**), which implies that the poly-T tail can disturb blunt-end stacking interactions, however without stabilizing a smectic phase. Another hint to the fact that Poly-T-duplex is not a bidisperse mixture of rod-like particles, is that the LC phase transitions happen at considerably higher DNA concentrations comparing to SC-duplex. More experiments should be conducted in order to resolve this ambiguous behaviour and understand the role of the poly-T tail as an interruption of attractive blunt-end interactions.

What is unequivocally clear from the phase diagram shown in **Figure 3.11**, is the appearance of a N^*/Sm transition when blunt-end stacking interactions are modified with hairpin loops. The stabilization of the smectic phase is a direct consequence of the controlled molecular aggregation by hairpin-mediated capping of the blunt-ends, which is a crucial parameter in order to obtain a uniform layer structure. Hence, the formation of a smectic-A phase with bilayer (SC-duplex) and monolayer molecular packing (FC-duplex) is energetically favourable. In the case of FC-duplex, we observe an increased stabilization of $Sm-A$ (blue region in **Figure 3.11**) at the expense of the N^* (green region in **Figure 3.11**). An interesting observation is that, in the case of SC-duplex and independently of the duplex length, the transition from Sm_b-A to Col is found. On the contrary, in the case of FC-duplex, the $Sm-A$ persists even at the very high DNA concentrations without any evidence of the Col .

3.4 Effects of an increasing terminal attraction strength on the self-assembly of SC-duplex

To probe how an increasing terminal attraction affects the self-assembly behaviour of the SC-duplex, without altering the chemical nature of the enthalpic contributions in our system, we exploit the sequence dependent character of base-pair stacking. The weakest stacking occurs between the A-T pair and T-A pair (-0,19 Kcal/mol), while the strongest one is at G-C/C-G (-2,17 Kcal/mol).⁴⁸

The main reason can be traced on the partial charge effect of the nucleobases, which is the one that gives a sequence-dependent character to the base-stacking interactions. Some atoms in the nucleobases can generate a charge displacement within the molecule they belong to, resulting in atoms becoming partially positively or negatively charged. This leads a positively charged atom from one base to align directly above or below the negatively charged atom from another base. If we look at the DNA nucleobases partial charges, we observe a dense accumulation of negative charge on the guanine ring (G) and a dense accumulation of positive charge on the cytosine ring (C). In contrast to the

G-C pair, the A-T one doesn't have strong joint concentrations of partial electric charge.

² In **Figure 3.11**, we present the concentration-dependant phase behaviour of a SC-duplex terminated with an A-T pair. In order to explore how an increasing terminal attraction affects the self-assembly of the SC-duplex, we have synthesized a SC-duplex ending in G-C pair. For convenience, we will refer to these SC-duplexes as SC-duplex (AT) and SC-duplex (GC), respectively. The phase diagram for the SC-duplex (AT) and the SC-duplex (GC), derived from SAXS and POM experiments, is presented in **Figure 3.13**. Comparing these two systems, we observe that, by increasing the DNA concentration the phase sequence $I/N^*/Sm-A/Col$ remains unchanged. Moreover, taking into account a 2% error in the DNA concentration measurements, the transitions borders (I/N^* and $N^*/Sm-A$) are qualitatively unaffected (see **Figure 3.13**). The difference that we notice is the shrinkage of the I/N^* phase coexistence (see the red regions of SC-duplex (AT) and SC-duplex (GC) in **Figure 3.13**) by an increasing the stacking strength. For the SC-duplex (GC) case, the narrowing of the I/N^* coexistence region in favour of the N^* , is most probably connected to the increase of the degree of dimerization due to the enhanced base stacking interactions compared to the SC-duplex (AT) case. Another interesting observation is that, in the case of SC-duplex (GC), the concentration width of the $Sm-A$ is more extended compared to the SC duplex (AT),

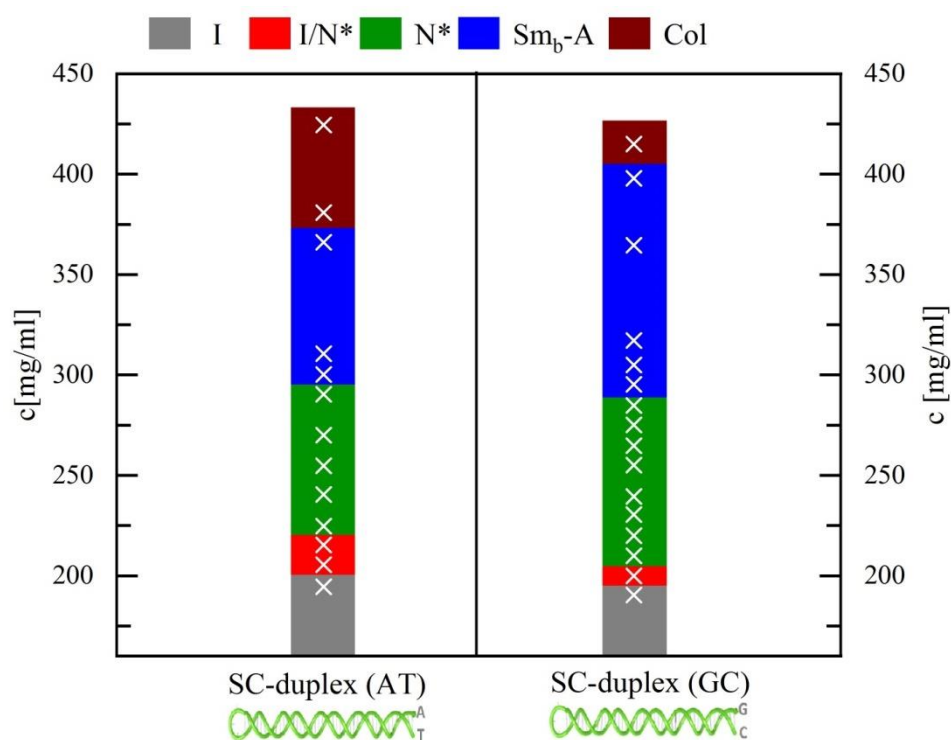


Figure 3.13 Phase diagrams of the SC-duplex (AT) (left side) and the SC-duplex (GC) (right side) as a function of total DNA concentration. Both systems are 48 bp long. Different LC phases are marked with different colours, in accordance to the colour code given in the previous phase diagrams. The white markers indicate the samples that were loaded into capillaries for SAXS measurements.

thus the *Sm-A/Col* transition is shifted to higher concentrations (see the blue/dark red interface in **Figure 3.13**). The flexibility at the contact points of the SC-duplexes is expected to be reduced with increasing the blunt-end stacking strength. This suggests, that the dimer's flexibility may play a key role in the formation of the *Col* phase. A more detailed discussion about this topic will be presented in section **3.6**.

3.5 Monte-Carlo simulations

To further investigate the effect of base stacking energies between the blunt-ends of SC-duplexes, and to gain further knowledge regarding the formation of LC mesophases in SC- and FC-duplexes, we performed Monte-Carlo simulation studies. The simulations were carried out by Prof. Cristiano De Michele from Sapienza University of Rome, Italy. Both SC- and FC-duplexes are modelled in a coarse-grained manner as hard cylinders (HCs), with length $L = 16 \text{ nm}$ and diameter $D = 2.4 \text{ nm}$. This results to a rod-like particle with aspect ratio $X_o = L/D = 6.67$. The diameter of HCs is slightly larger than the steric diameter of DNA (2 nm), to take into account the electrostatic repulsion. In the case of SC-duplex, the terminal base pair is modelled by an interacting site A (inset of **Figure 3.14a**). The site A corresponds to the centre of a small red sphere positioned on the symmetry axis with diameter δ , and imitates the blunt-end attractive terminal site of SC-duplex.⁴⁹ The latter is located on the symmetry axis of the cylinder at a distance equal to $L/2 + 0.15D/2$ from the cylinder's centre of mass. Two distinct HCs interact with their interacting sites A via a square well potential, which is defined as the following:

$$\beta u_{sw} = \begin{cases} \beta u_0, & r < \delta \\ 0, & r > \delta \end{cases}$$

where $\delta = (0.5/2.4)D$ is the interaction range (i.e diameter of the sphere associated with the interacting sites A), and r is the distance between two interacting sites. Attraction strength between the hydrophobic patches equals to $\beta u_0 = 8.0$, where the resulting stacking free energy equate approximately to the one determined previously from the phase behaviour⁴⁹⁻⁵¹ and cholesteric properties⁵² of self-assembling ultra-short DNA duplexes. It should also be noted that SC- and FC-duplex systems in our simulations consists of $N_L = 6$ particle layers, unless otherwise stated. The results of the simulations (i.e. pair-distribution function, concentration, energy etc.) were obtained by discarding the initial equilibrium state and by performing a huge number of MC steps (10^8). This was possible by employing a recently developed algorithm for simulating hard cylinders⁵³, which relies on a novel and very efficient algorithm for finding the roots of a quartic equation.⁵³

In order to characterize the phase behaviour of SC- and FC- duplexes, we calculated the equation-of-state (EOS) presented in **Figure 3.14a** and **b**, respectively. The DNA concentration is plotted on the x-axis, while the dimensionless pressure $P^* = \beta P v_0$ is

plotted on the y-axis, with v_0 the volume of a single cylinder. The EOS of the SC-duplex, shown in **Figure 3.14a**, clearly shows the first-order transition from I to N phase by increasing the concentration. Further increase of concentration results to a second

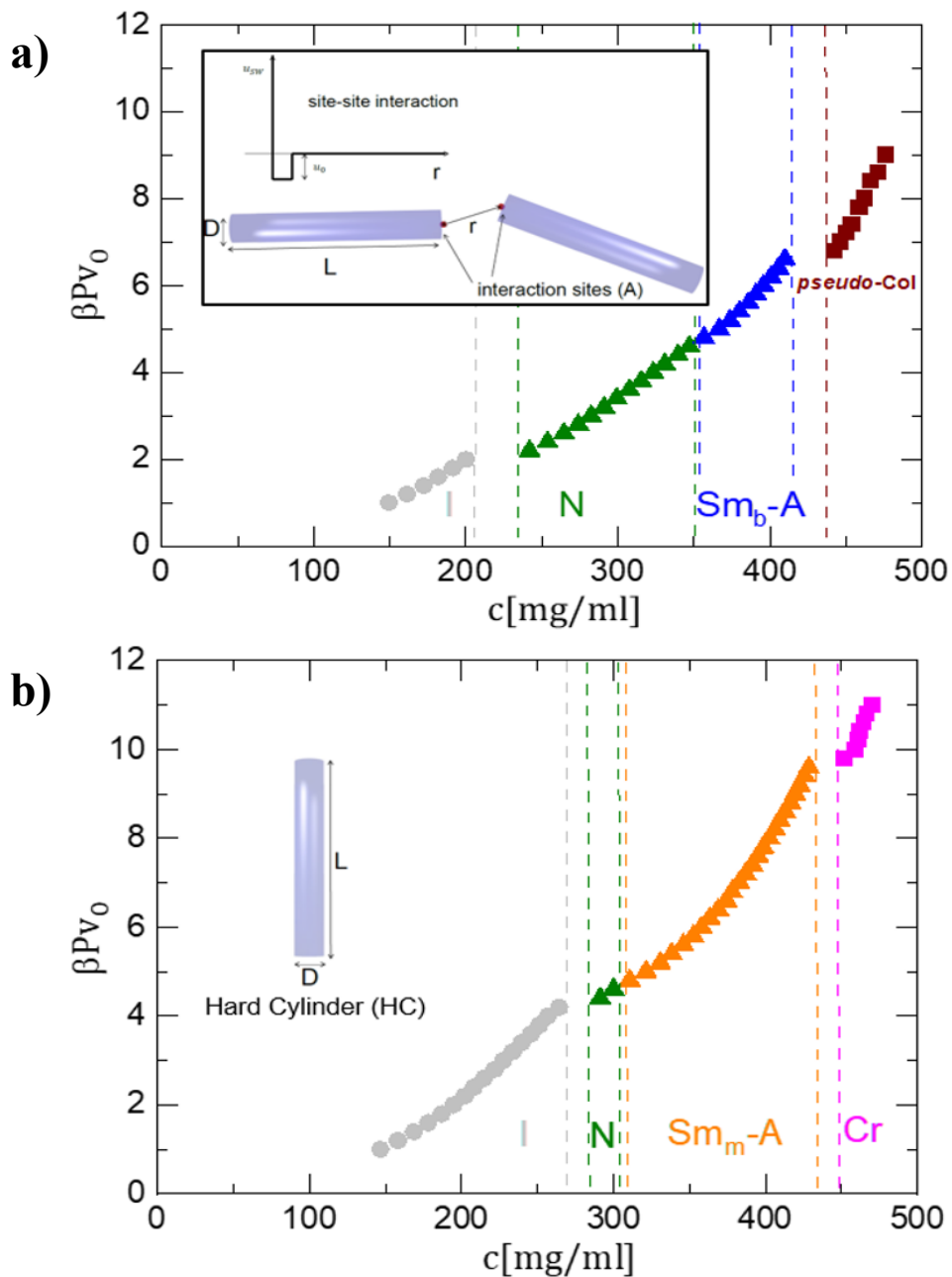


Figure 3.14 a) The equation of state for SC-duplex obtained from MC simulations. The inset shows a schematic representation of the model SC-duplexes where interacting sites A are represented with two small red spheres interacting via the square well (SW) potential. The red spheres diameter indicates the interaction range and corresponds to the width of the well. The depth of the well u_0 corresponds to the binding energy. The cylinder diameter is D and its length L . **b)** The equation of state for the FC-duplex (modelled as a hard cylinder of length L and diameter D) obtained from MC simulations. The type of phase behavior in the EOS of SC- and Fc-duplex systems is also indicated (I : isotropic, N : uniform nematic, Sm_b -A: Bilayer smectic-A type, pseudo-Col: columnar phase due to finite-size effects, Cr : hexagonal)

transition from the $Sm-A$ to a metastable columnar phase (pseudo- Col , see [Figure 3.16](#)). The I/N and $Sm-A/pseudo-Col$ are indicated by a noticeable break in the P^* versus concentration curve. The transition between the N and $Sm-A$ phases is indicated by a small jump in concentration (see the dashed lines between the green and blue curves in [Figure 3.14a](#)), which implies either a weak first-order transition or a second-order one. The EOS of the FC-duplex is shown in [Figure 3.14b](#), where the I to N and N to $Sm-A$ transitions are visible. Furthermore, we observe pronounced stabilization of the smectic phase compared to the nematic phase, resulting to a significant shrinkage of the nematic region, in contrast to the SC-duplex case (see width of N region in [Figure 3.14 a](#) and

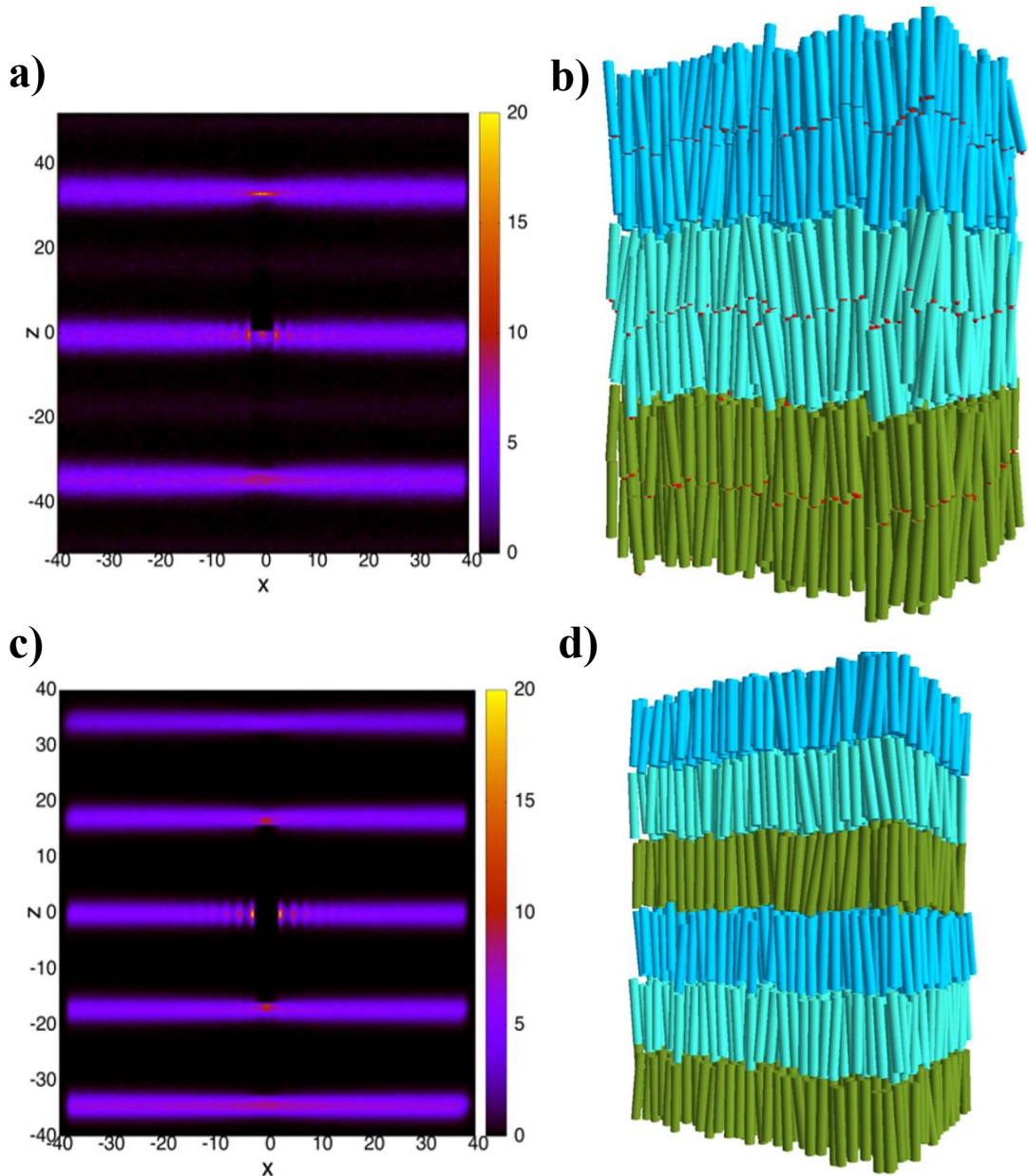


Figure 3.15 a) 2D pair-distribution function $g_{||}(\mathbf{r}_{||})$ for SC-duplex parallel to the nematic director from the patchy unit's centre of mass b) Snapshot of Sm_b-A at $\beta P v_0 = 6$, where duplexes stuck on top of one another through their blunt-ends (red dots) c) 2D pair-distribution function $g_{||}(\mathbf{r}_{||})$ from the cylinders' center of mass for FC-duplex d) Snapshot of Sm_m-A at $\beta P v_0 = 9.4$.

b). The widening of the smectic phase at the expense of nematic in the LC behaviour of our model FC-duplex with aspect ratio $X_0 = 6.67$ is in agreement with results from HSCs (data for $X_0 = 4.0$ ²¹). The very wide nematic region in the case of the SC-duplex can be understood in terms of length bidispersity, using a simple packing argument. This will be better explained later through the degree of dimerization shown in [Figure 3.18](#).

Observing the smectic structures of SC- and FC-duplexes, as obtained by computing the 2D pair-distribution functions $g_{||}(\mathbf{r}_{||})$, and the snapshots of the corresponding LC mesophases, we notice strikingly different $Sm-A$ structures. In the case of SC-duplex, where the monovalent attractive units are localized exactly in the middle of the dimer-based smectic layers. This is also demonstrated in the computed 2D pair-distribution function $g_{||}(\mathbf{r}_{||})$ from the patchy unit's centre of mass (sites A in the inset of the [Figure 3.14a](#)) parallel to the nematic director. ([Figure 3.15a](#)) In the case of FC-duplex, the 2D pair-distribution function $g_{||}(\mathbf{r}_{||})$ from the cylinder's centre of mass in [Figure 3.15c](#), suggests that the $Sm-A$ phase has a monolayer morphology (see snapshot in [Figure 3.15d](#)) with the layer thickness comparable to the length of one FC-duplex, similarly to the case of the monodisperse hard spherocylinders.^{18,21}

Concerning the appearance of the pseudo-*Col* phase in the case of SC-duplex system consisting of 6 particle layers ($N_L=6$), the 2D pair-distribution function $g_{\perp}(\mathbf{r}_{\perp})$ of the cylinders centre of mass perpendicular to the nematic director, ([Figure 3.16a](#)) and the

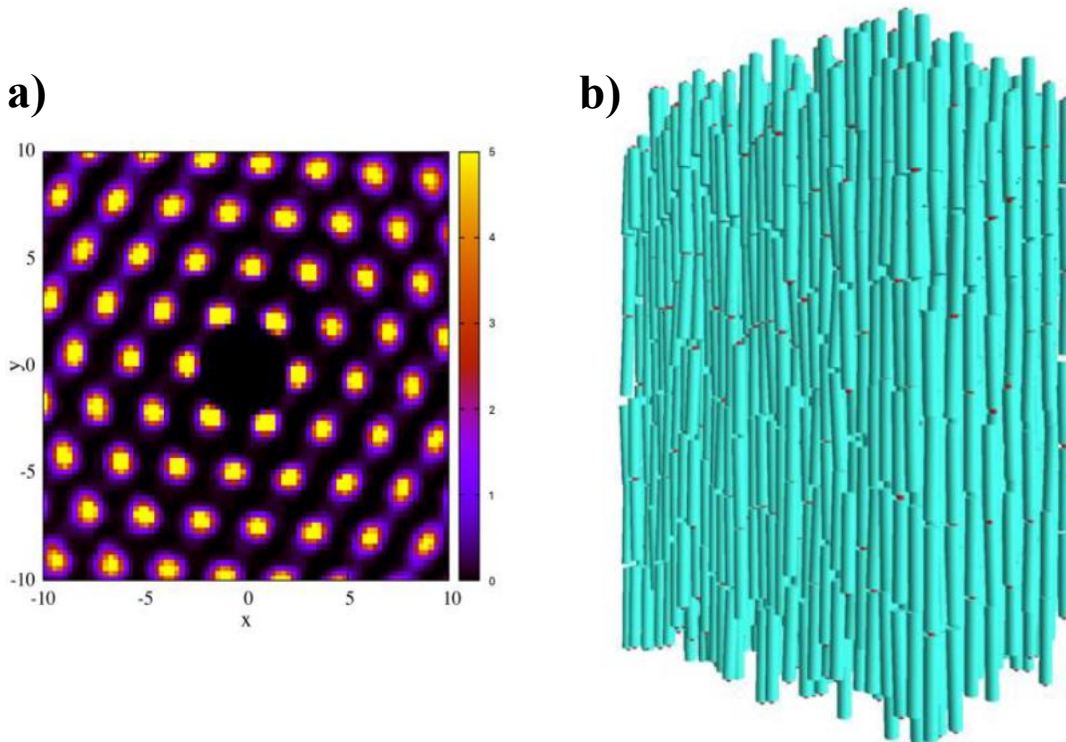


Figure 3.16 a) 2D pair-distribution function perpendicular to the nematic axis $g_{\perp}(\mathbf{r}_{\perp})$
b) Snapshot of the metastable columnar phase for $\beta P v_0 = 8.4$. The SC-duplex consists of 6 particle layers.

corresponding snapshot (**Figure 3.16b**) indicate the arrangement of linear aggregates of SC duplex into a 2D hexagonal lattice with a rather random orientation of the patchy units. We also concluded that the thermodynamic stability of the columnar phase is strongly simulation box dependent, which is in agreement with previous studies^{54,55}, that it is just due to the finite-size effects, if the simulation box size along the nematic axis is not significantly larger than the length of each particle. Starting from the same initial configuration, when the simulation box consists of 6 particle layers, *Col* is observed, but when we enlarge it to 16, then *Col* becomes unstable and it transforms into a hexagonal crystalline phase (*Cr*). (see **Figure 3.17**) However, for the rest of the phase diagram, there is no noticeable system size dependence, as demonstrated in the SC-duplex's EOS for $N_L = 6$ and $N_L = 16$ in **Figure 3.17**.

A particular intriguing information concerning the concentration-dependence of the fraction of reversibly bonded SC-duplex η_f can be extracted from the simulated SC-duplexes. The experimental determination of such a quantity is a challenging task. In **Figure 3.18**, the dimerization degree η_f of SC-duplex is plotted against the DNA concentration for SC-duplex system with $N_L = 6$ and $N_L = 16$. Similar to EOS, no noticeable system size dependence is observed in the concentration-dependence of η_f

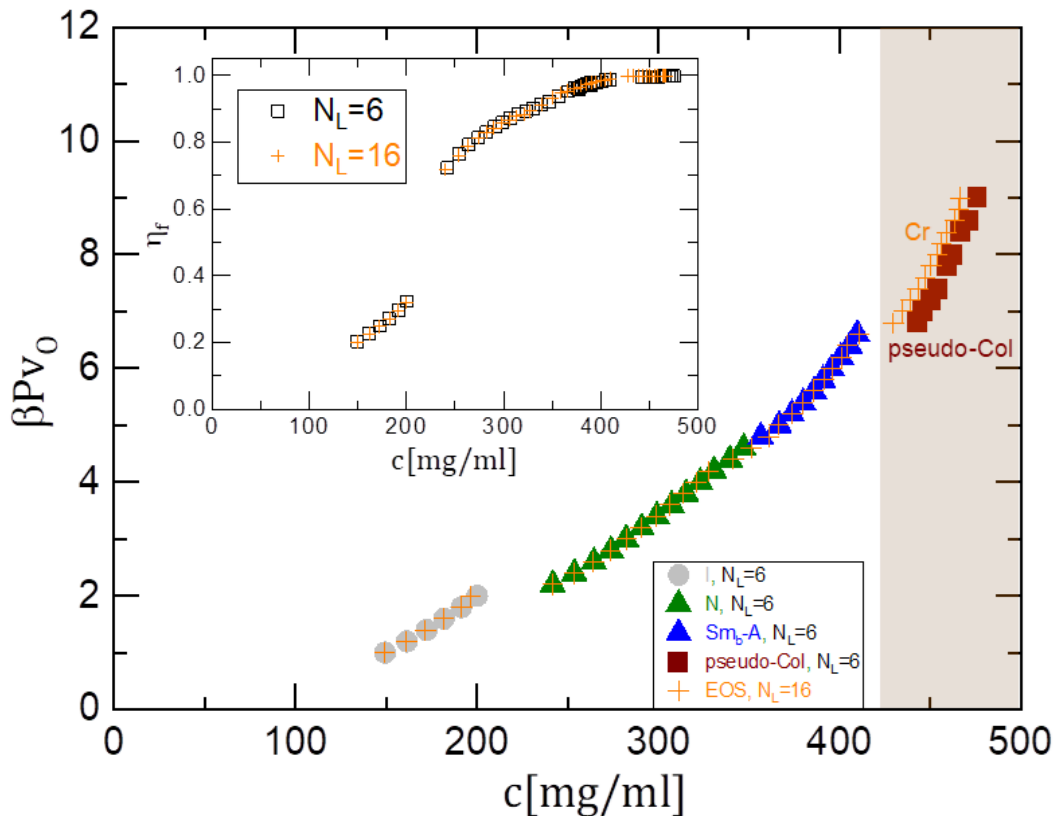


Figure 3.17 Simulated EOS for the SC-duplex, starting from the same initial configuration with different number of particle layers, N_L . The shadowed region represents the concentration interval where the discrepancy in the SC-duplex EOS for $N_L = 6$ and $N_L = 16$ is observed. In the top left inset, the corresponding concentration-dependent fractions of SC-duplex dimers η_f are presented.

(inset of **Figure 3.17**). The sudden jump in η_f , from 0.32 (*I*, grey dots) to 0.72 (*N*, green triangles) in **Figure 3.18**, indicates that the nematic phase consists of a large portion of dimers. Increasing the concentration within the *N* region, the degree of dimerization increases from 0.72 to 0.92, where in this range, the co-existence of cylinders with two different lengths (monomers and dimers) is expected to interfere with the strict layer thickness requirements pertaining to the smectic order. Therefore, the *N/Sm-A* will be shifted to higher concentrations in comparison with the case of FC-duplex. This conclusion gives us an explanation, in terms of length bidispersity, of the wide nematic region in the case of SC-duplex. This finding is also supported by MD simulation studies in the binary mixtures of HSCs^{56,57} and HCs⁵⁸ at the equivalence point, which demonstrate the destabilization of smectic phase on the benefit of the nematic. Finally, the degree of SC-duplex dimerization approaches the value of 1 near *Sm-A/pseudo-Col* transition, suggesting that our system consists solely of dimers. Furthermore, with the increase of the dimensionless pressure $\beta P v_0$, restrictions in the bond angle θ between two SC-duplexes (see the left inset of **Figure 3.18**) appear around the *I/N* transition. These are shown in the right side inset of **Figure 3.18**, where the computed angular distributions $P(\theta)$ is plotted versus θ . When the dimensionless pressure increases, $P(\theta)$ distribution narrows down, while its peak shifts towards larger angle values. This behaviour becomes especially pronounced in the *Sm-A* region (blue curve in the inset of **Figure 3.18**), reaching a full straight configuration of SC-duplex dimers ($\theta=180^\circ$) in the pseudo-*Col* phase. Finally, we would like to attract the attention to an earlier MC simulation work on the liquid crystalline phase behaviour of dimerizing HSCs.⁵⁹ The

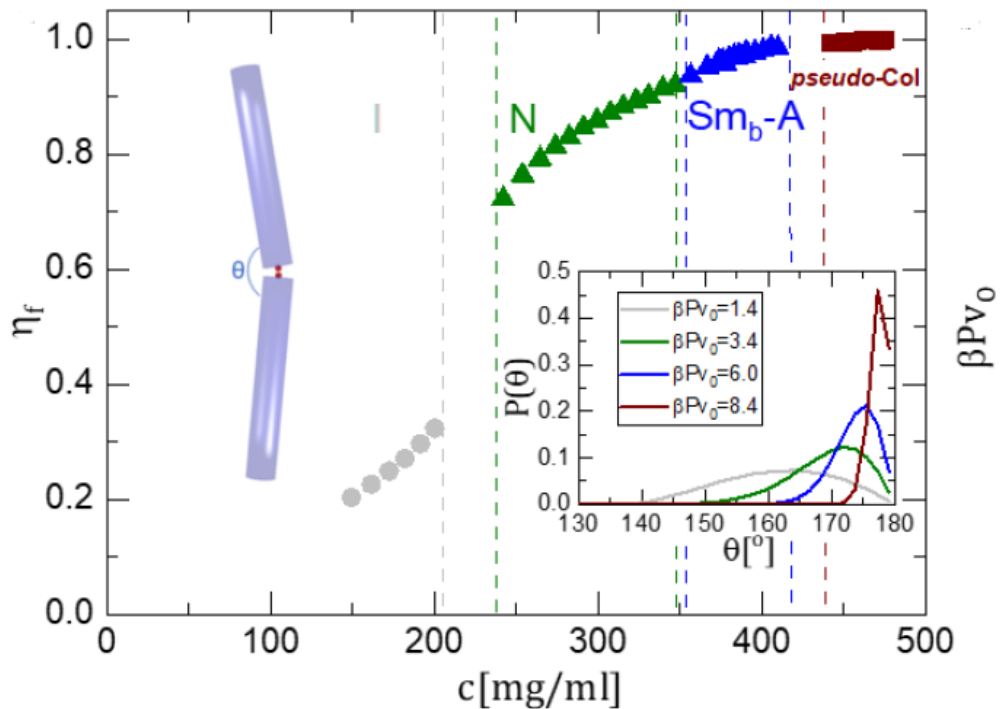


Figure 3.18 Fraction of SC-duplex dimers. Inset: Angle dimer distribution for selected state points – *I* ($\beta P v_0=1.4$), *N* ($\beta P v_0=3.4$), *Sm_b-A* ($\beta P v_0=6.0$) and *Col* ($\beta P v_0 = 8.4$).

authors employed HSCs with an attractive square well of depth $\beta u_0 = 7.0$ at one end, and aspect ratio of $L/D = 5$. These parameters are quite similar to those used for modelling the SC-duplexes. Interestingly, no evidence for the existence of $Sm-A$ phase bilayer morphology (Sm_b-A) is found. Instead, only the formation of a monolayer $Sm-A$ phase has been revealed, essentially the same as that of purely repulsive HSCs system. The discrepancies of our and mentioned work, suggest that the stabilization of the Sm_b-A , mediated by the presence of single attractive sites on the tips of the HSCs, may be particularly sensitive to the details of geometry of these attractive patches. We can speculate that the lack of Sm_b-A in the latter study, can be likely ascribed to the high flexibility of dimer bonds due to the large volume available for bonding of the patches. However, further studies are necessary for verifying this speculation.

In order to investigate in more detail, the effect of base stacking energies between the blunt ends of the SC-duplexes, we carried out MC simulations for attraction strengths between $6.7 k_B T$ (weak limit) and $11.9 k_B T$ (strong limit). The chosen geometry

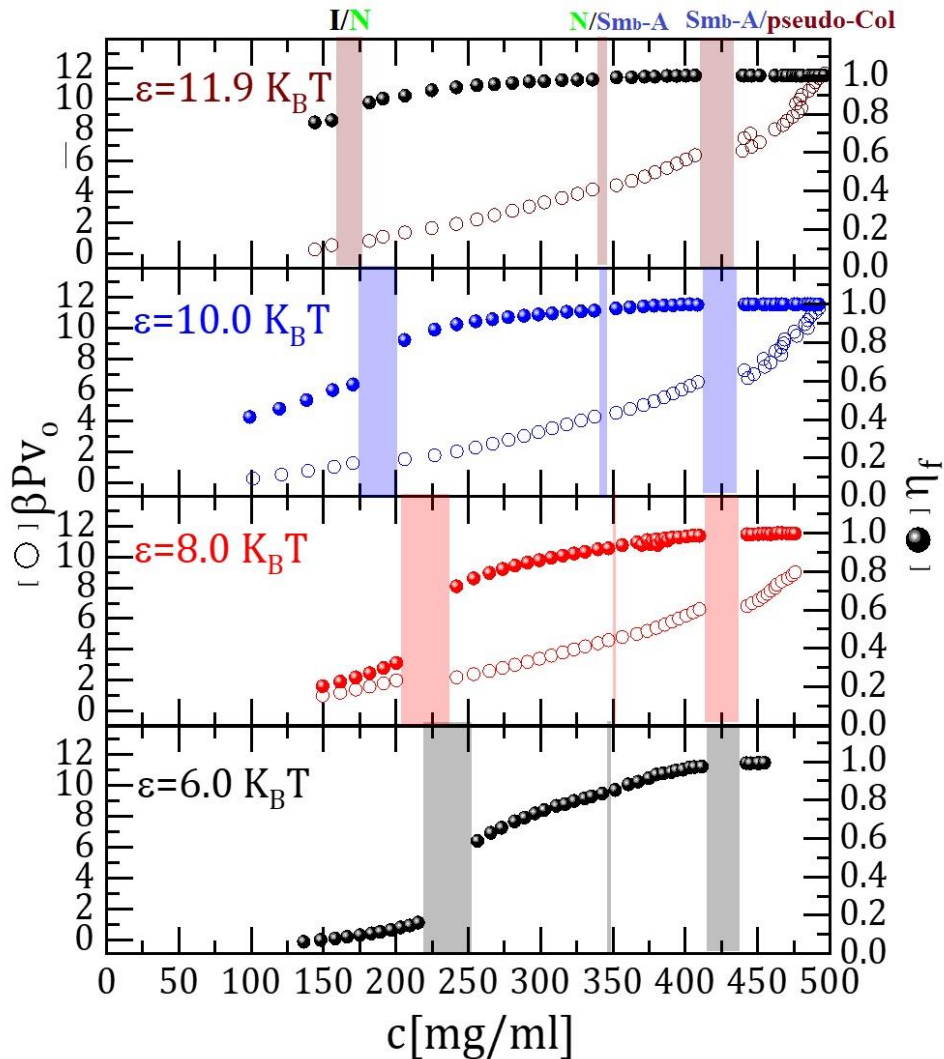


Figure 3.19 Equation of state $\beta P V_0$ (empty circles) and fraction of SC-duplex dimers η_f as a function of concentration for a different attraction strengths $k_B T$.

and the interaction potential of the interactive sites A don't allow us to perceive the changes in the flexibility at the association points of the SC-duplexes. In **Figure 3.19** an interesting overview on the concentration-dependence of the dimensionless pressure $\beta P v_0$ (see the empty circles in the graph) and the dimer's fraction η_f (see filled circles in the graph) is presented, for different attraction strengths. The first thing we notice is that the same phase sequence is present for all the attraction strengths. With the increase of the attractive strength, the I/N coexistence region (the first shadowed region from the left in the graph) shifts towards lower concentrations and shrinks. The N/Sm_b-A coexistence region (the middle, shadowed region in the graph) weakly shifts towards lower concentrations when the attractive strength increases, with the widening of the biphasic region. It can be seen that, increasing the attraction strength, the abrupt change in the degree of dimerization at the I/N transition is diminished. For a blunt-end attraction strength above $8.0 k_B T$, η_f already reaches the value of 0.8 just above the I/N region. Lastly, no significant changes to the Sm_b-A /pseudo- Col coexistence region are visible. This is not surprising, since in the $Sm-A$ /pseudo- Col transition, we are almost in the regime of full dimerization (η_f above 0.97 for the explored attraction strengths) and in our model the flexibility of the bonds at the association points of the SC-duplexes is independent of the attraction strength.

3.6 On the molecular origin of a columnar phase in SC-duplexes

Understanding the appearance of a Col liquid crystalline phase in SC-duplexes requires to consider the balance of many factors including effective molecular elongation (change in aspect ratio),⁶⁰ length polydispersity,^{56–58,61,62} and flexibility^{60,63}. For the SC-duplexes with duplex length of 48bp, the possibility that the aspect ratio increase upon dimerization may lead to the formation of Col has to be ruled out, since the Sm_b-A/Col transition is also observed in the experimental phase diagram of SC-duplexes with duplex length of 24 bp (see **Figure 3.12**). Concerning the length polydispersity, or in the case of SC-duplex bidispersity (monomers coexisting with dimers), it is a rather improbable scenario since MC simulations showed that SC-duplexes are completely dimerized near the $Sm-A$ /pseudo- Col transition (see values of η_f in **Figure 3.18**). Hence, the most obvious reason for the stabilization of Col phase lies in the bending flexibility at the junction point of the SC-duplex dimer. This is supported by the fact that by increasing the terminal attraction strength of SC-duplex by exchanging the terminal A-T pair the with G-C one, the Sm_b-A/Col transition is shifted to higher concentrations (blue/brown interface in **Figure 3.13**). Since the dimerization and the bending flexibility of the SC-duplex are strongly intertwined, a new system is synthesized in order to address the stabilization of Col phase solely to the duplex flexibility. As demonstrated in the bottom panels a-b of **Figure 3.20**, a 48bp long FC-duplex is fabricated with one unpaired thymine base T (marked with red color in **Figure**

3.20a) located at the middle of the DNA duplex, and it will hereby be referred to as FC-duplex-1T-flex. It is expected that the above-mentioned DNA scaffold modification will



Figure 3.20 a) Schematic drawings of a stiff(top) and a flexible(bottom) fully-capped DNA duplex. The sequences of the strands are also shown, where the site-specific flexibility in the FC-duplex-1T-flex is indicated by the red thymine (T) base located in the middle of the DNA duplex backbone. Both of the DNA duplexes are 48bp long. **b)** Schematic cartoons of FC-duplex and FC-duplex-1T-flex created with NUPACK analysis software.

capture the effect of bending flexibility in SC-duplex dimers with duplex length of 24 bp at high DNA densities.

For determining the phase behaviour of the FC-duplex-1T-flex, presented in the bottom panels of **Figure 3.20**, SAXS was used. In **Figure 3.21** a representative series of 1D-SAXS patterns at 20°C, for various concentrations of FC-duplex-1T-flex aqueous saline solutions, are shown. By increasing the DNA concentration, similar to the FC-duplex case, a multiple concentration-induced transition sequence from I , over I/N^* to N^* and to Sm_m -A is observed (**Figure 3.21e-c**). In the latter liquid crystalline phase, the position of the first Bragg's reflection q^* corresponds to a layered structure with a distance between the neighbouring layers of $d = 2\pi/q^* = 17.9 \text{ nm}$, which roughly corresponds to the length of one FC-duplex-1T-flex (**Figure 3.21c**). Contrary to the FC-duplex case, a further increase of the FC-duplex-1T-flex concentration leads to the formation of a Col phase (**Figure 3.21b**), implying that the above-mentioned type of the flexibility, which is introduced in the middle of the FC-duplex, dramatically alters the system's phase behaviour at high DNA densities.

The concentration-dependent phase diagram of FC-duplex-1T-flex is presented in **Figure 3.22** together with the corresponding FC-duplex and the SC-duplex (with duplex length of 24 bp), in order to easily demonstrate the influence of this site-specific flexibility on the formation of liquid crystalline states. Comparison between the liquid crystalline phase behaviour of FC-duplex and FC-duplex-1T-flex demonstrates that the I/N^* transition is shifted to higher densities by increasing the flexibility. These results are in accordance with the predictions and computer simulations.^{28,57,64-66} However, the critical concentration at which N^*/Sm_m -A transition occurs is virtually unaffected.

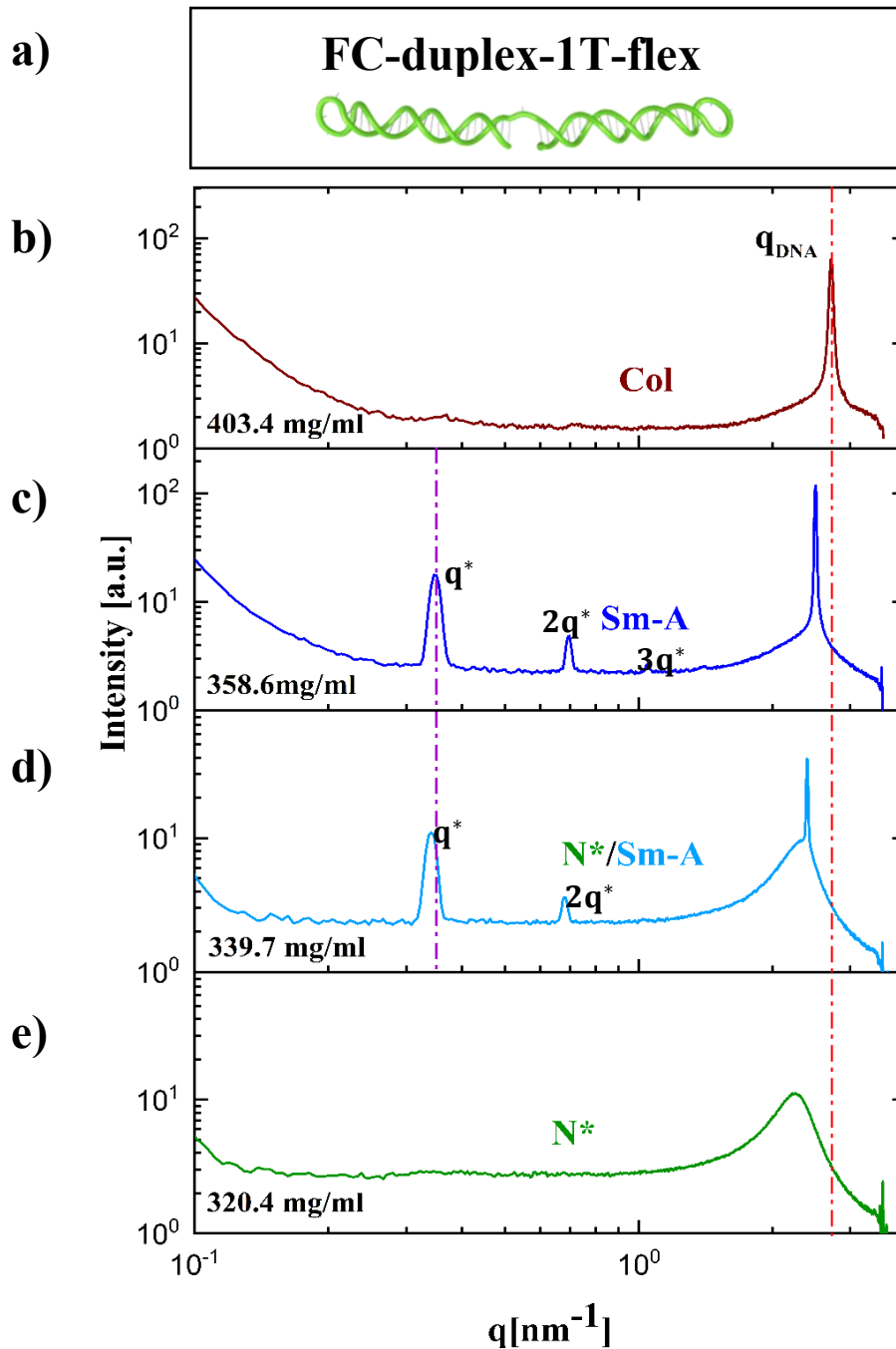


Figure 3.21 *a)* A schematic representation of FC-duplex-1T-flex *b)* 1D-SAXS profile of concentration 403.4 mg/ml that corresponds to Col ordering. The red dashed line across the whole figure enables an easier observation of the concentration dependence of the sharp high q_{DNA} . *c)* The dark blue curve at the concentration of 358.6 mg/ml shows a typical smectic x-ray scattering profile and corresponds to Sm-A type of ordering. The purple dashed line is centred around the principal q^* peak and demonstrates how this peak shifts towards lower q -values as the DNA concentration decreases. *d)* The light blue X-ray scattering curve, at the concentration of 339.7 mg/ml, reveals a coexistence between the broad and the sharp high q_{DNA} peak, suggesting a $N^*/Sm-A$ coexistence. *e)* 1D-SAXS curve corresponds to the one-phase N^* with the concentration of 320.4 mg/ml.

Finally, the appearance of the *Col* phase in the FC-duplex-1T-flex, significantly shrinks the smectic region, in accordance with the phase behaviour of SC-duplex. Taken together, the phase diagram of **Figure 3.22** reveals that the flexibility at the SC-duplexes' association points (dimer's junction) and the introduction of site-specific flexibility in a rod-like particle (FC-duplex-1T-flex) can stabilize the columnar phase at the expense of the smectic.

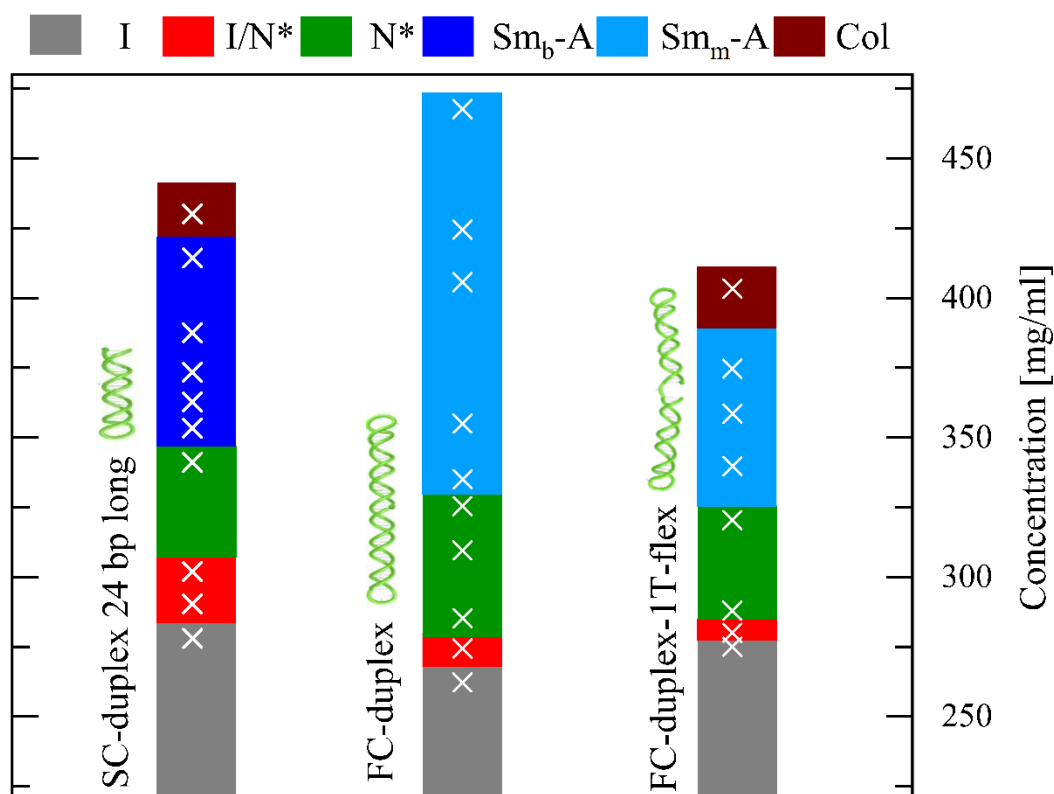


Figure 3.22 Phase diagrams for the SC-duplex with $L = 24$ bp, FC-duplex and FC-duplex-1T-flex with $L = 48$ bp as a function of total DNA concentration. The coloured regions correspond to different LC phases, in accordance to the colour code given above the diagram. The white markers indicate the concentrations of the samples that were loaded in the capillaries for SAXS measurements. Phase identification and determination of the boundaries between the coloured regions were carried out by the combination of SAXS experiments, the visual inspection of the capillaries between cross-polarizers and the recording of the optical textures as observed by POM.

3.7 Summary and conclusions

The importance and the role of the weak blunt-end base stacking interactions in DNA LC self-assembly have been confirmed through experiments and simulations. It was demonstrated how the screening of these terminal attractive interactions can significantly affect the DNA self-assembly. Modifications were imposed on one or both ends of the DNA helix by selectively blocking the blunt-ends with hairpin loops or poly-T tails, or by altering the type of the terminal base-pair. Here it was shown that as a direct result of blocking these attractive end-stacking interactions on one (SC-duplex) or both sides (FC-duplex), the thermodynamically stable bilayer and monolayer smectic-A phase is stabilized. These findings provide concrete evidence that the so far elusive smectic phase in concentrated solutions of stiff DNA duplexes with a sufficient anisotropy is a direct consequence of the presence of blunt-ends.

Experimentally found LC phases, except the *Col* phase in the phase diagram of SC-duplex, were confirmed by MC simulations. In addition, despite the coarse-grained character of the SC- and FC-duplex models, it also demonstrated a remarkable quantitative agreement between experiments and simulations on the position of *I/LC* transition. Furthermore, simulation and experimental studies are in agreement regarding the reported changes in the LC phase behaviour caused by different types of end-modifications of the DNA duplexes. As already mentioned, MC simulations did not report the presence of a stable *Col* phase. This is in agreement with other simulation studies of dense suspensions of monodisperse, purely repulsive, rod like particles with moderate aspect ratios ($L/D \leq 11$) and varying degrees of internal flexibility.^{19,30,32,55,67} In the case of the FC-duplex, the transition *Sm_m-A/Col* is not present, in contrast to the SC-duplex, where the single blunt-end seems to stabilize *Col* phase. Also, the experiments revealed that the concentration range stability of the *Col* phase is reduced when increasing the strength of blunt-end attractions. Indeed, the phase diagram of **Figure 3.13**, demonstrates that the *Col* phase is shifted towards higher concentrations while *Sm_b-A* widens. The latter is supported by the simulation findings on the effects of the end-attraction strength in the LC phase behaviour of the SC-duplex system. Several theoretical, experimental and computer simulation studies suggest the following key factors for the formation of stable phase: enhanced aspect ratio,⁶⁰ length polydispersity,^{56-58,61,62} and flexibility^{60,63}. However, the experiments with SC-duplex of half duplex length (24bp) and reported experimental studies on the suspensions of filamentous phages^{35,36,60,68,69} rule out the first two factors, raising flexibility as the main hypothesis for the stabilization of *Col*. This issue is addressed in section 3.6 by the synthesis and study of the self-assembly of FC-duplex with one unpaired thymine base located in the middle of the DNA duplex (FC-duplex_1T-flex). The results offered a conclusive evidence that the flexibility at the SC-duplex dimer's junction is the key mechanism for the stabilization of *Col* phase at high DNA densities. It is worth mentioning that, molecular dynamics simulations of model rod-like particles with

similar values of aspect ratio and flexibility to our experimental SC-duplex system, which are decorated with a single weak attractive tip modelled by a Lennard– Jones potential, predict the existence of a Sm_b-A phase without any evidence of a stable Col phase. However, a recent experimental study on the LLC behaviour of aqueous solutions of monodisperse rod-like filamentous viruses⁷⁰, having one tip functionalized with hydrophobic fluorescent dyes and with a similar flexibility as considered in the work of Menegon et al.⁷¹, but one order of magnitude higher aspect ratio, did not reveal the formation of an equilibrium Sm_b-A phase. The lack of clear evidence of an experimental bilayer smectic phase is attributed to the multivalent character of this type of terminal modification which, most probable, allows branching at the viruses association points. The results presented in this chapter suggest therefore that, at least from an experimental point of view, the key element for the existence of thermodynamic stable Sm_b-A phase is the monovalent attractive character of the blunt-end stacking interactions, which gives rise to a stiff enough bond.

Here it was demonstrated how non-covalent blunt-end stacking interactions enable the creation of well-defined monovalent attractive patches in DNA. The presented work opens a pathway for the re-examination of the phase diagram of short DNA duplexes with $L \leq L_p$. This research topic is addressed in the following chapter.

Bibliography

1. Guckian, K. M. *et al.* Factors contributing to aromatic stacking in water: Evaluation in the context of DNA. *J. Am. Chem. Soc.* **122**, 2213–2222 (2000).
2. Calladine, C. R., Drew, H. R., Luisi, B. F. & Travers, A. . *Understanding DNA*. (Elsevier, 2004). doi:10.1016/B978-0-12-155089-9.X5000-5.
3. Bellini, T., Cerbino, R. & Zanchetta, G. DNA-Based Soft Phases. in *Peptide-Based Materials*. **310**, 225–279 (2011).
4. Watson, J. D. & Crick, F. H. C. Molecular Structure of Nucleic Acids: A Structure for Deoxyribose Nucleic Acid. *Nature* **171**, 737–738 (1953).
5. Kool, E. T. H Hydrogen Bonding , Base Stacking , and. *Annu. Rev. Biophys. Biomol. Struct.* **30**, 1–22 (2001).
6. Nakata, M. *et al.* End-to-end stacking and liquid crystal condensation of 6-to 20-base pair DNA duplexes. *Science*. **318**, 1276–1279 (2007).
7. Zanchetta, G., Bellini, T., Nakata, M. & Clark, N. A. Physical polymerization and liquid crystallization of RNA oligomers. *J. Am. Chem. Soc.* **130**, 12864–12865 (2008).
8. Woo, S. & Rothmund, P. W. K. Programmable molecular recognition based on the geometry of DNA nanostructures. *Nat. Chem.* **3**, 620–627 (2011).
9. Gerling, T., Wagenbauer, K. F., Neuner, A. M. & Dietz, H. Dynamic DNA devices and assemblies formed by shape-complementary, non-base pairing 3D components. *Science*. **347**, 1446–1452 (2015).

10. Nakata, M. *et al.* End-to-End Stacking and Liquid Crystal Condensation of 6– to 20–Base Pair DNA Duplexes. *Science* (80-.). **318**, 1276–1279 (2007).
11. Davidson, M. W., Strzelecka, T. E. & Rill, R. L. Multiple Liquid Crystal Phases at High DNA Concentrations. *Nature* **331**, 457–460 (1988).
12. Livolant, F., Levelut, A. M., Doucet, J. & Benoit, J. P. The highly concentrated liquid-crystalline phase of DNA is columnar hexagonal. *Nature* **339**, 724–726 (1989).
13. Durand, D., Doucet, J. & Livolant, F. A study of the structure of highly concentrated phases of DNA by X-ray diffraction. *J. Phys. II* **2**, 1769–1783 (1992).
14. Strey, H. H. *et al.* Refusing to twist: Demonstration of a line hexatic phase in DNA liquid crystals. *Phys. Rev. Lett.* **84**, 3105–3108 (2000).
15. Pelta, J., Durand, D., Doucet, J. & Livolant, F. DNA mesophases induced by spermidine: Structural properties and biological implications. *Biophys. J.* **71**, 48–63 (1996).
16. Onsager, L. the Effects of Shape on the Interaction of Colloidal Particles. *Ann. N. Y. Acad. Sci.* **51**, 627–659 (1949).
17. Franco-Melgar, M., Haslam, A. J. & Jackson, G. A generalisation of the Onsager trial-function approach: describing nematic liquid crystals with an algebraic equation of state. *Mol. Phys.* **106**, 649–678 (2008).
18. Frenkel, D. Onsager’s spherocylinders revisited. *J. Phys. Chem.* **91**, 4912–4916 (1987).
19. Bolhuis, P. & Frenkel, D. Tracing the phase boundaries of hard spherocylinders. *J. Chem. Phys.* **106**, 666–687 (1997).
20. Frenkel, D., Lekkerkerker, H. N. W. & Stroobants, A. Thermodynamic stability of a smectic phase in a system of hard rods. *Nature* **332**, 822–823 (1988).
21. McGrother, S. C., Williamson, D. C. & Jackson, G. A re-examination of the phase diagram of hard spherocylinders. *J. Chem. Phys.* **104**, 6755–6771 (1996).
22. Lydon, J. Chromonic liquid crystalline phases. *Liq. Cryst.* **38**, 1663–1681 (2011).
23. Nastishin, Y. A. *et al.* Optical characterization of the nematic lyotropic chromonic liquid crystals: Light absorption, birefringence, and scalar order parameter. *Phys. Rev. E - Stat. Nonlinear, Soft Matter Phys.* **72**, 1–14 (2005).
24. Dickinson, A. J., Laracuenta, N. D., McKitterick, C. B. & Collings, P. J. Aggregate structure and free energy changes in chromonic liquid crystals. *Mol. Cryst. Liq. Cryst.* **509**, 9/[751]-20/[762] (2009).
25. Maiti, P. K., Lansac, Y., Glaser, M. A. & Clark, N. A. Isodesmic self-assembly in lyotropic chromonic systems. *Liq. Cryst.* **29**, 619–626 (2002).
26. Salamonczyk, M. *et al.* Smectic phase in suspensions of gapped DNA duplexes. *Nat. Commun.* **7**, 13358 (2016).
27. Pouget, E., Grelet, E. & Lettinga, M. P. Dynamics in the smectic phase of stiff viral rods. *Phys. Rev. E - Stat. Nonlinear, Soft Matter Phys.* **84**, 1–6 (2011).

28. Van Der Schoot, P. The nematic-smectic transition in suspensions of slightly flexible hard rods. *J. Phys. II* **6**, 1557–1569 (1996).
29. Tkachenko, A. V. Effect of chain flexibility on the nematic-smectic transition. *Phys. Rev. E* **58**, 5997–6002 (1998).
30. De Braaf, B., Oshima Menegon, M., Paquay, S. & Van Der Schoot, P. Self-organisation of semi-flexible rod-like particles. *J. Chem. Phys.* **147**, (2017).
31. Bladon, P. & Frenkel, D. Simulating polymer liquid crystals. *J. Phys. Condens. Matter* **8**, 9445–9449 (1996).
32. Cinacchi, G. & De Gaetani, L. Phase behavior of wormlike rods. *Phys. Rev. E* **77**, 051705 (2008).
33. Li, L., Pabit, S. A., Lamb, J. S., Park, H. Y. & Pollack, L. Closing the lid on DNA end-to-end stacking interactions. *Appl. Phys. Lett.* **92**, 2–5 (2008).
34. Wang, R., Kuzuya, A., Liu, W. & Seeman, N. C. Blunt-ended DNA stacking interactions in a 3-helix motif. *Chem. Commun.* **46**, 4905–4907 (2010).
35. Dogic, Z. & Fraden, S. Smectic phase in a colloidal suspension of semiflexible virus particles. *Phys. Rev. Lett.* **78**, 2417–2420 (1997).
36. Grelet, E. Hard-rod behavior in dense mesophases of semiflexible and rigid charged viruses. *Phys. Rev. X* **4**, 021053 (2014).
37. Kuijk, A., Byelov, D. V., Petukhov, A. V., Van Blaaderen, A. & Imhof, A. Phase behavior of colloidal silica rods. *Faraday Discuss.* **159**, 181–199 (2012).
38. Zadeh, J. N. *et al.* NUPACK: Analysis and design of nucleic acid systems. *J. Comput. Chem.* **32**, 170–173 (2011).
39. Riley, M., Maling, B. & Chamberlin, M. J. Physical and chemical characterization of two- and three-stranded adenine-thymine and adenine-uracil homopolymer complexes. *J. Mol. Biol.* **20**, 359–389 (1966).
40. Ke, C., Humeniuk, M., S-Gracz, H. & Marszalek, P. E. Direct measurements of base stacking interactions in DNA by single-molecule atomic-force spectroscopy. *Phys. Rev. Lett.* **99**, 1–4 (2007).
41. Salamonczyk, M. *et al.* Smectic phase in suspensions of gapped DNA duplexes. *Nat. Commun.* **7**, 1–9 (2016).
42. Merchant, K. & Rill, R. L. DNA length and concentration dependencies of anisotropic phase transitions of DNA solutions. *Biophys. J.* **73**, 3154–3163 (1997).
43. Fraden, S., Maret, G. & Caspar, D. L. D. Angular correlations and the isotropic-nematic phase transition in suspensions of tobacco mosaic virus. *Phys. Rev. E* **48**, 2816–2837 (1993).
44. Lekkerkerker, H. N. W., Coulon, P., Van Der Haegen, R. & Deblieck, R. On the isotropic-liquid crystal phase separation in a solution of rodlike particles of different lengths. *J. Chem. Phys.* **80**, 3427–3433 (1984).
45. Birshtein, T. M., Kolegov, B. I. & Pryamitsyn, V. A. Theory of athermal lyotropic liquid crystal systems. *Polym. Sci. U.S.S.R.* **30**, 316–324 (1988).

46. Vroege, G. J. & Lekkerkerker, H. N. W. Phase transitions in lyotropic colloidal and polymer liquid crystals. *Reports Prog. Phys.* **55**, 1241–1309 (1992).
47. Wensink, H. H. & Vroege, G. J. Isotropic-nematic phase behavior of length-polydisperse hard rods. *J. Chem. Phys.* **119**, 6868–6882 (2003).
48. Protozanova, E., Yakovchuk, P. & Frank-Kamenetskii, M. D. Stacked-unstacked equilibrium at the nick site of DNA. *J. Mol. Biol.* **342**, 775–785 (2004).
49. Nguyen, K. T., Sciortino, F. & De Michele, C. Self-Assembly-Driven Nematization. *Langmuir* **30**, 4814–4819 (2014).
50. De Michele, C., Bellini, T. & Sciortino, F. Self-assembly of bifunctional patchy particles with anisotropic shape into polymers chains: Theory, simulations, and experiments. *Macromolecules* **45**, 1090–1106 (2012).
51. De Michele, C., Rovigatti, L., Bellini, T. & Sciortino, F. Self-assembly of short DNA duplexes: From a coarse-grained model to experiments through a theoretical link. *Soft Matter* **8**, 8388–8398 (2012).
52. De Michele, C., Zanchetta, G., Bellini, T., Frezza, E. & Ferrarini, A. Hierarchical Propagation of Chirality through Reversible Polymerization: The Cholesteric Phase of DNA Oligomers. *ACS Macro Lett.* **5**, 208–212 (2016).
53. Orellana, A. G. & Michele, C. De. Algorithm 1010. *ACM Trans. Math. Softw.* **46**, 1–28 (2020).
54. Veerman, J. A. C. & Frenkel, D. Relative stability of columnar and crystalline phases in a system of parallel hard spherocylinders. *Phys. Rev. A* **43**, 4334–4343 (1991).
55. Dussi, S., Chiappini, M. & Dijkstra, M. On the stability and finite-size effects of a columnar phase in single-component systems of hard-rod-like particles. *Mol. Phys.* **116**, 2792–2805 (2018).
56. Stroobants, A. Columnar versus smectic order in binary mixtures of hard parallel spherocylinders. *Phys. Rev. Lett.* **69**, 2388–2391 (1992).
57. Stroobants, A. Liquid crystal phase transitions in bidisperse hard-rod systems. *J. Phys. Condens. Matter* **6**, (1994).
58. Bohle, A. M., Hołyst, R. & Vilgis, T. Polydispersity and Ordered Phases in Solutions of Rodlike Macromolecules. *Phys. Rev. Lett.* **76**, 1396–1399 (1996).
59. McGrother, S. C., Sear, R. P. & Jackson, G. The liquid crystalline phase behavior of dimerizing hard spherocylinders. *J. Chem. Phys.* **106**, 7315–7330 (1997).
60. Grelet, E. & Rana, R. From soft to hard rod behavior in liquid crystalline suspensions of sterically stabilized colloidal filamentous particles. *Soft Matter* **12**, 4621–4627 (2016).
61. Bates, M. A. & Frenkel, D. Influence of polydispersity on the phase behavior of colloidal liquid crystals: A Monte Carlo simulation study. *J. Chem. Phys.* **109**, 6193–6199 (1998).
62. Varga, S., Velasco, E., Mederos, L. & Vesely, F. J. Stability of the columnar and smectic phases of length-bidisperse parallel hard cylinders. *Mol. Phys.* **107**,

- 2481–2492 (2009).
63. Grelet, E. Hexagonal Order in Crystalline and Columnar Phases of Hard Rods. *Phys. Rev. Lett.* **100**, 168301 (2008).
 64. Chen, Z. Y. Nematic Ordering in Semiflexible Polymer Chains. *Macromolecules* **26**, 3419–3423 (1993).
 65. Tkachenko, A. L. Nematic-smectic transition of semiflexible chains. *Phys. Rev. Lett.* **77**, 4218–4221 (1996).
 66. Dijkstra, M. & Frenkel, D. Simulation study of the isotropic-to-nematic transitions of semiflexible polymers. *Phys. Rev. E* **51**, 5891–5898 (1995).
 67. Wilson, M. R. Molecular dynamics simulation of semi-flexible mesogens. *Mol. Phys.* **81**, 675–690 (1994).
 68. Purdy, K. R. & Fraden, S. Influence of charge and flexibility on smectic phase formation in filamentous virus suspensions. *Phys. Rev. E - Stat. Nonlinear, Soft Matter Phys.* **76**, (2007).
 69. Barry, E., Beller, D. & Dogic, Z. A model liquid crystalline system based on rodlike viruses with variable chirality and persistence length. *Soft Matter* **5**, 2563–2570 (2009).
 70. Repula, A., Oshima Menegon, M., Wu, C., Van Der Schoot, P. & Grelet, E. Directing Liquid Crystalline Self-Organization of Rodlike Particles through Tunable Attractive Single Tips. *Phys. Rev. Lett.* **122**, 128008 (2019).
 71. Oshima Menegon, M., Kusters, G. L. A. & van der Schoot, P. Self-organization of tip-functionalized elongated colloidal particles. *Phys. Rev. E* **100**, 042702 (2019).

Chapter 4

Liquid crystal phase diagram of all-DNA repulsive rods

Purely repulsive DNA rods were synthesized by suppressing the intermolecular base-stacking interaction between blunt-ended DNA helices. Specifically, we designed a semi-capped DNA duplex (SC-duplex) where one blunt-end is blocked with a short non-sticky single-stranded DNA dangling chain. The phase diagram of these purely repulsive all-DNA rods, where the DNA concentration is plotted against the duplex length, is constructed by a combination of small-angle X-ray scattering and polarized optical microscopy measurements. Our work confirms the results from earlier seminal simulation studies of Frenkel and co-workers on self-assembly of hard spherocylinders. With increasing all-DNA rods aspect ratio, the smectic-A phase becomes stable before the nematic phase. A two-phase coexistence appears at the transition from the isotropic to the smectic-A phase in rods with $L/D=3.3$. For larger aspect ratios, $L/D=4.95$, the chiral nematic phase becomes first stable and as a result the smectic-A phase is preceded by this liquid crystalline phase. The reported DNA duplexes with these particular terminal modifications can be viewed as a new model system platform for rigid rods, covering an important shape anisotropy gap in the area of rod-like lyotropic liquid crystals, where direct comparison with results from simulation studies is feasible.

4.1 Introduction

In 1949, Onsager's theoretical work¹ on extremely thin spherocylinders with $L/D \rightarrow \infty$ showed that, at sufficiently high densities, they undergo a solely entropy-drive transition from isotropic to nematic liquid crystal phase due to the excluded volume effects. This transition is accompanied by an unusual increase of order and entropy, explained in terms of the gain in translational entropy at the expenses of the orientational one.¹ This was a "wind tail" for the development of research on the topic of the phase behavior of rod-like colloidal particles with less extreme shape and short-ranged repulsive interactions²⁻⁷ and silica rods⁸⁻¹⁰. To a first approximation, hard spherocylinders (HSCs) are considered as a good model for the above-mentioned experimental systems, due to its simplicity and the fact that they are easy to compute in simulations. They are cylinders with diameter D and length L , capped on both sides with hemispheres of the same diameter. The parameter that characterizes the phase behaviour of such particles is the shape anisotropy, which is described by the particle's aspect ratio L/D . A schematic drawing of such spherocylinder is presented in [Figure 4.1a](#).

Computer simulations involving stochastic Monte Carlo (MC) techniques have been very useful for determining equilibrium LC phases and LC phase boundaries of rod-shaped particle systems.¹¹⁻²¹ A first attempt to determine the HSC phase diagram, which was involving such a computer simulation method, was reported by Veerman and Frenkel.²² However, this study focused on only a small number of sparse L/D values. For this reason, McGrother et al. conducted more extensive simulations in the region $3 < L/D < 5$.¹⁴ A detailed phase diagram of HSC model with various shape anisotropy (L/D) is computed by Bolhuis and Frenkel.¹⁶ This work significantly advanced our understanding of the phase behaviour of this model system by providing evidence for the entropic-driven formation of the nematic, smectic and columnar phases. However, it is important to emphasize that the columnar phase observed in the seminal simulation studies on HCSs by Frenkel et al.¹² proved by the same group to be mechanically unstable for sufficiently large simulation system sizes.²³ Finally, the work from Dussi et al.²⁰ confirm that the columnar phase is indeed unstable for a system of freely rotating HSCs even at aspect ratio as extreme as $L/D = 100$.

Some fair understanding of a phase behaviour of rods polydisperse in length, was provided by the study of Bates and Frenkel.²¹ It was shown that, when the polydispersity is relatively small, the phase behaviour remains essentially the same as monodispersed systems. However, as the polydispersity increases, the smectic (Sm) phase destabilizes relative to the N phase at lower densities and the columnar phase (Col) at higher densities and is fully suppressed above some critical level of polydispersity.

Molecular dynamics (MD) and other deterministic approaches, which use short-range soft-core or pseudo-hard-core potentials, have also been employed to understand the phase behaviour of rodlike particles.^{13,24-29} This approach have been used by Naderi and van der Schoot²⁵ in order to study how flexibility affects the phase behaviour of rod-like particles and their dispersion in the smectic-A ($Sm-A$) phase. The study showed that transition from N to Sm shifts to higher particle densities for more flexible rods. Moreover, they also confirmed that flexibility decreases the diffusion of particles in the direction perpendicular to the director significantly while not affecting the diffusion along the director. The shift in the phase transitions towards higher particle densities, when flexibility of the rodlike particles is increased, was also confirmed by the work of De Braaf et al.²⁷ Additionally, through this study of the LC phase behaviour of four different L/D of semi-flexible rod-like particles, they found that the increase in L/D shifts phase transitions to lower particle densities. Repula et al.²⁴ and Oshima Menegon et al.²⁹ both studied the phase behaviour of semiflexible colloidal rod systems with a single attractive tip. Both groups observed that as the tip attractions are increased, the Sm phase region significantly widens at the expense of N , until N is completely preceded by Sm .

Experimental research on rodlike particles progressed at a pace similar to theory and simulations. One of the first experimental systems ideally suited as a test system for the

Onsager theory was tobacco mosaic virus (TMV), which is successfully isolated from infected tomato plants.³⁰ Back in the 1930s the existence of liquid crystalline behaviour is observed in aqueous suspensions of the TMV.³¹ This observation have inspired Lars Onsager to work on his seminal theory of the isotropic-to-nematic phase transition in colloidal rod liquid crystals. More specific, a phase separation into a thin optical isotropic and a thick birefringent phase was detected when the virus concentration exceeded 2%.³² Detailed small angle X-ray scattering (SAXS) experiments, from Oldenbourg and co-workers³³, revealed a transition from isotropic through a biphasic region into a nematic phase with increasing TMV concentration. The complete phase diagram of the TMV was later predicted from theory and simulations by Graf and Löwen as a function of the virus and salt concentration.³⁴ This work did not only describe the isotropic to nematic transition with its two-phase coexistence region, but also further higher ordered liquid crystalline phase transitions into stable smectic phases and colloidal crystal phases.

In addition to TMV, liquid crystalline behaviour is also observed in solutions of filamentous bacteriophages, called fd-viruses.³⁵ Since these two types of virus represent the closest experimental equivalents to hard particles, they were considered as unique model systems for rodlike liquid crystals that could be found in nature. After screening their charge, particles interact only through short-range and purely repulsive interactions.³⁶ However, due to a number of TMV deficiencies including: long time required to grow tobacco plants and isolate the virus, the relative ease with which particles aggregate end-to-end yielding polydisperse suspensions, and the difficulty of introducing genetic modifications, filamentous phages have supplanted TMV as a choice model system of rod-like particles³⁷ Filamentous virus has a very high degree of monodispersity and large aspect ratio. In addition, since the virus DNA can be can systematically mutated, it was possible to vary its contour length, flexibility and chirality. These unique properties of filamentous bacteriophages not only enabled the first quantitative test of the Onsager theory but also revealed that their moderately concentrated aqueous solutions exhibit a very rich concentration-dependant liquid crystalline behaviour, including smectics, columnar and crystal phases.^{3,4,6,7,38} Comparison between semiflexible fd rods, theoretical models and simulations enabled deeper insight into how slight flexibility affects liquid crystal phase transitions, especially the nematic-to smectic (*N-Sm*) phase transition.^{3,6} Finally, the fact that single fd-virus can be visualized with fluorescence optical microscopy provided a valuable insight into the dynamics of this system at different liquid crystalline states.³⁹⁻⁴²

Very recently, silica rods^{8,43}- a synthetic rod-like system with uniform length- has demonstrated a rich liquid crystalline behaviour. They are proposed as a very close experimental realization of HSC system. Indeed, the phase diagram of silica rods with L/D between 3.7 and 8 has shown a considerable match with the one extracted from the previously mentioned simulations on HSCs, both for a single^{8,9} and binary component system.¹⁰

Long before the fd virus, another long, thin, semi-rigid biological polymer was explored for its intriguing properties. Already in the 1940s it was established that DNA molecules can form various liquid crystal phases when hydrated. Extensive experimental studies of long DNA chains extracted from natural sources⁴⁴, semi-rigid sonicated, fragments close to the persistence length of the DNA^{45–50} and short fragments of DNA 6-10 bp long⁵¹, showed the presence of chiral nematic and columnar mesophases. In the previous chapter, we explored the role of end-to-end stacking interactions, which are considered as the main hypothesis for the appearance of the LC phases in the solutions of short duplexes.

We introduced the interruption of end-stacking interactions on one or both terminal sites of a DNA duplex employing hairpin loops. This resulted in the appearance of the smectic phase. By using hairpin loops on both sides, a fully capped duplex (FC-duplex), we created purely repulsive rodlike molecules. Since the DNA's length is very easy to be modified at sub-nanometre level, this implies that FC-duplexes could be an intriguing experimental realization of hard spherocylinders (**Figure 4.1**). Therefore, we decided re-examine the phase diagram of DNA-based rod-like systems using FC-duplexes with different L/D , expecting significantly richer phase behaviour than in the case of polydisperse blunt-ended DNA fragments.^{47,50}

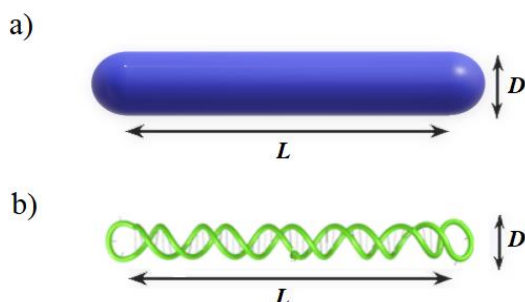


Figure 4.1 a) A hard spherocylinder (HSC) with length L and diameter D b) A schematic drawing of the fully capped DNA duplex (FC-duplex) with length L and diameter D

4.2 Design and fabrication of all-DNA repulsive rods

In the previous chapter, we showed that a DNA fragment with duplex length L below its persistence length ($L_p^{dsDNA} \sim 150 \text{ bp}$) with both blunt-ends capped with hairpin loops (FC-duplex, **Figure 4.1b**), behaves like a rigid repulsive rod. Initially, FC-duplexes of variable aspect ratios, ranging from 7.92 (48bp) to 2.97 (18bp), were fabricated. For the calculation of aspect ratio, we used a steric diameter D , which equals to 2nm, while the length of duplexes, L , we calculated by multiplying the number of base pairs with the thickness of one base pair (0.33 nm). The synthetic procedure is already described in **Chapter 2**.

We checked the success of our synthesis with gel electrophoresis. Small amount of the sample was collected during several preparation steps (thermal annealing and concentration procedure) and subjected to electrophoresis in 10% polyacrylamide gel electrophoresis (PAGE). PAGE experiments confirmed the successful assembly of the

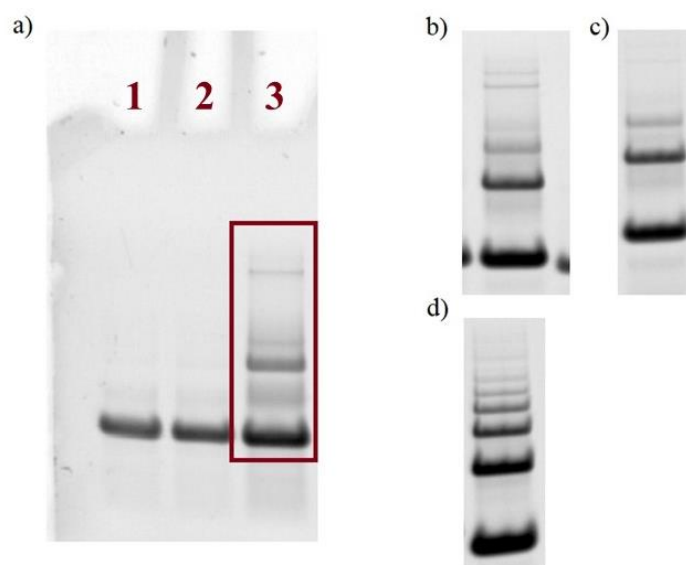


Figure 4.2 Multiple bands in gel electrophoresis of FC-duplexes with various L/D : a) A non-denaturing 10% PAGE for FC-duplex with $L = 30bp$. From the left to right: Lane 1- the sample after sequences annealing, Lane 2- the sample after dispersion in Milli-Q water and Lane 3- the sample after reaching the highest concentration in $1xTE/Na$ buffer solution ($10mM$ Tris-HCl, $150 mM$ NaCl, $pH=8$) b-d) A non-denaturing 10% PAGE for FC-duplexes, taken from highly DNA concentrated solutions with duplex length, L , equal to $26bp$ (b), $24bp$ (c) and (d) $20bp$

abovementioned FC-duplexes. However, PAGE experiments performed on FC-duplexes with $L/D \leq 5$, which are collected from highly concentrated aqueous saline solutions, revealed the existence of multiple sharp bands. A typical example of such an experiment is presented in **Figure 4.2a** for a FC-duplex with $L = 30bp$. The lack of a single sharp band in lane 3 clearly indicates the formation of aggregates, since the extra bands demonstrate the decreased mobility compared to the most intense band. Similar behaviour is observed also for shorter FC-duplexes ($L = 20bp, 24bp, 26bp$), as depicted in **Figure 4.2b-d**.

We employed the UNAFold (“Unified Nucleic Acid Folding”) analysis package from the IDT (Integrated DNA Technologies), a free software package for nucleic acid folding prediction, in order to further increase the stability of FC-duplexes. Different sequences, rich in G-C pairs, together with a careful sequence design in close vicinity of the hairpin loop, did not lead to a noticeable stability improvement. In addition, FC-duplex stability is tested with PAGE during the sample concentration procedure revealing that, as more concentrated the FC-duplex solution becomes, the number of the bands in the PAGE images is increasing. The same tendency is also observed by

decreasing the duplex length (**Figure 4.2b-d**). This suggests that the FC-duplex aggregation is concentration-dependent below a critical aspect ratio L/D . As evident from the above findings, the presence of two non-bonded (hairpin) loops in partially paired DNA duplexes promotes their destabilization below a critical stem duplex length ($L \leq 30$ bp) in aqueous solutions of moderately concentrated FC-duplexes. In order to overcome this obstacle, we designed an alternative candidate for an all-DNA repulsive rod system. This is a SC-duplex with its blunt-end capped by a six-thymine (6T) bases-long dangling tail (**Figure 4.3**). We will refer to FC- and modified SC-duplexes as FC-xx-duplex and SC-xx-duplex_xT, respectively. The symbols “xx” and “x” indicate the number of base-pairs (bp) and the number of unpaired T bases, respectively. In the previous chapter, we have demonstrated that unpaired, single-stranded DNA dangling chain can disturb the base-stacking forces, however, without full screening this type of terminal adhesion. Surprisingly, the combination of two types of terminal duplex modifications, a tail and a loop, proved to be an efficient way to fabricate stable all-DNA repulsive rods ranging in duplex length from 60 to 20 bp. This is clearly illustrated in the PAGE image of **Figure 4.5**, which confirms that SC-xx-duplex_6T constructs of varying length migrate as single sharp bands. Furthermore, the liquid crystalline transition boundaries are not significantly impacted by the above combination of terminal modifications in a blunt-ended DNA duplex. An example is presented in **Figure 4.4**, where the concentration-dependent phase diagrams of FC-48-duplex and SC-48-duplex_6T are presented. These two systems exhibit the same concentration-dependent liquid crystalline phase sequence. In addition, the width of I/N^* biphasic region and the location of I/N^* and N^*/Sm phase transitions appeared to be affected slightly by the abovementioned terminal duplex modifications.

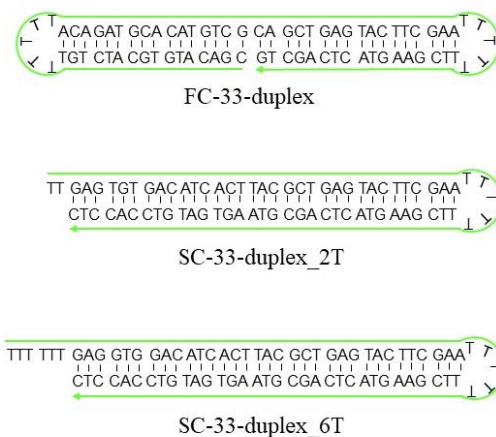


Figure 4.3 A schematic representation of FC-duplex 33base pairs long, SC-duplex 33 base pairs long with 2 thymine bases as tail, and SC-duplex 33 base pairs long with 6T-tail

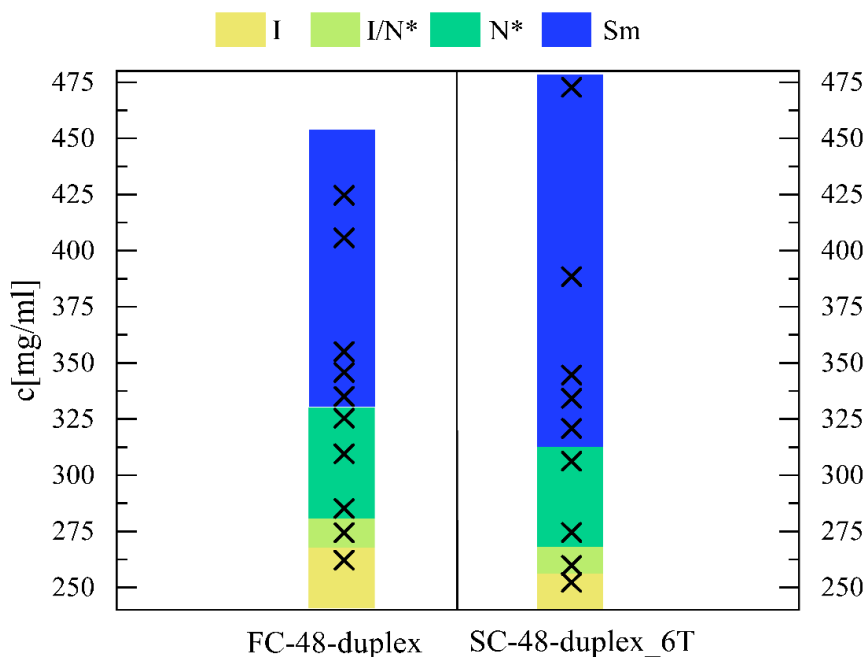


Figure 4.4 Phase diagrams of the FC-48-duplex (left side) and the SC-48-duplex_6T (right side), with $L = 48\text{bp}$, as a function of total DNA concentration. Different LC phases are marked with different colours. The colour code is given at the top of the graph. The black markers indicate the samples that were loaded into capillaries for SAXS measurements.

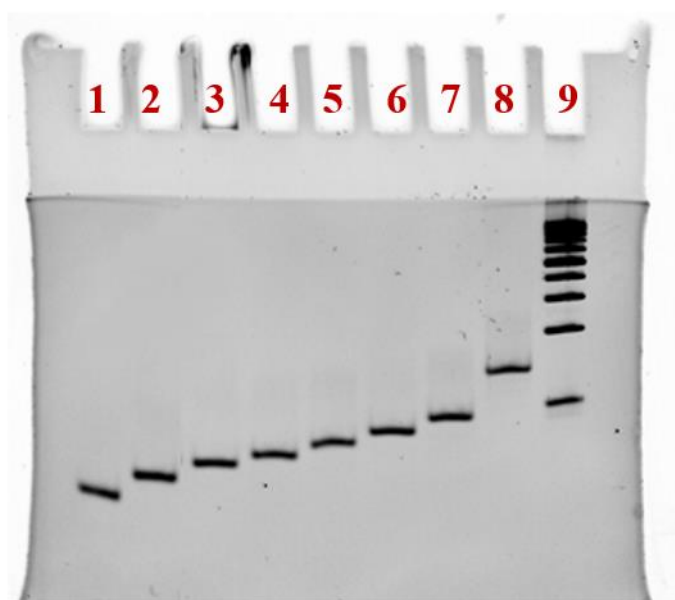


Figure 4.5 10 % PAGE electrophoresis of selected modified SC-duplexes. Going from left to right - Lane 1: SC-20-duplex_6T, Lane 2: SC-24-duplex_6T, Lane 3: SC-28-duplex_6T, Lane 4: SC-30-duplex_6T, Lane 5: SC-33-duplex_6T, Lane 6: SC-36-duplex_6T, Lane 7: SC-40-duplex_6T, Lane 8: SC-60-duplex_6T, Lane 9: 50 bp DNA ladder that consists of 10 DNA fragments ranging from 50 bp to 500 bp

It is worth mentioning, that six-base (6T) tail was the minimum sterically length for fulfilling two important requirements: (a) the formation of short duplexes with stable folding structures under crowded conditions and (b) preserving the same sequence of phase transitions from lower to higher DNA concentrations. Comparison between liquid crystalline behavior of SC-33-duplex_2T and SC-33-duplex_6T, at similar concentration, in **Figure 4.6** demonstrates that the stability of the smectic phase is significantly affected by the length of the terminal tail, which is related with its efficiency to suppress the blunt-end stacking.

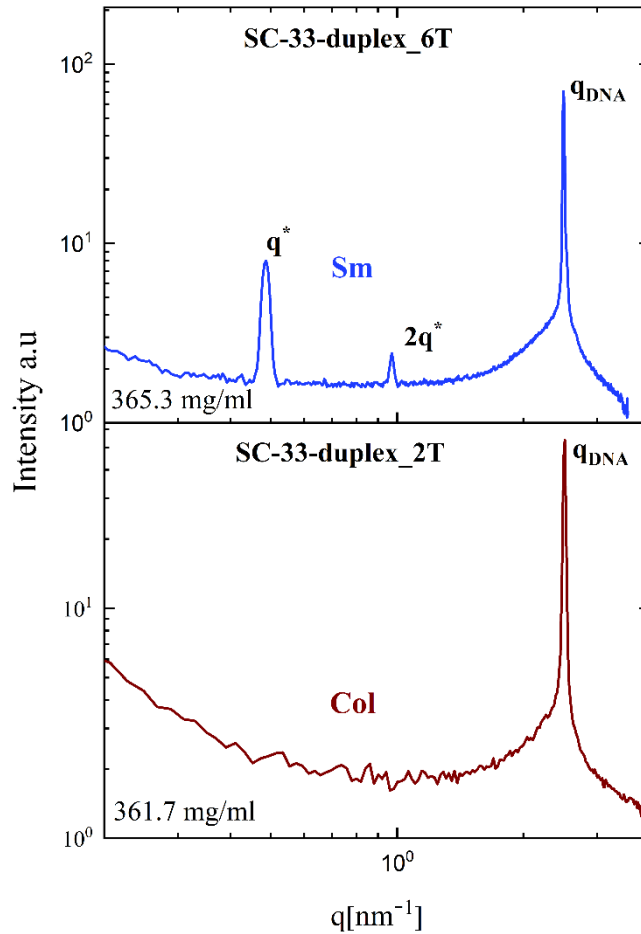


Figure 4.6 1D-SAXS profiles of 33 base pairs long SC-duplexes with 2T (bottom panel) and 6T as terminal tail (top panel). In the case of SC-33-duplex_2T, at the concentration of 361.7 mg/ml, Col phase is formed (dark brown curve), while in the case of SC-33-duplex_6T at the similar concentration (365.3 mg/ml), we observe Sm phase (blue curve). Comparison between these two scattering profiles demonstrates the influence of the tail length on the stability of smectic phase.

4.3 Phase behaviour of all-DNA repulsive rods with tunable aspect ratio

4.3.1 Structural characterization of all-DNA rod-like liquid crystals

Small-angle X-ray scattering measurements served as the basis for determining the phase behaviour of the all-DNA repulsive rod-like constructs presented in **Figure 4.3**. A representative concentration-dependant series of one-dimensional (1D) SAXS profiles at 20°C for three different systems SC-60-duplex_6T, SC-36-duplex, SC-20-duplex_6T will be presented.

One-dimensional (1D) SAXS profiles for the SC-60-duplex_6T, with an aspect ratio $L/D = 9.9$, are shown in **Figure 4.8** for various concentrations. By increasing the DNA concentration, a rich phase transition pathway from disordered to various ordered phases is observed, similar to those encountered in the SC-48-duplex_6T system (see **Figure 4.4**). Over the concentration range $217.1 \text{ mg/ml} \leq c \leq 241.96 \text{ mg/ml}$, a phase transition from an isotropic (I) to cholesteric N^* (**Figure 4.8e**), through a two-phase coexistence (I/N^*) at total DNA concentration of 226.0 mg/ml , is observed. This type of liquid crystalline phase it is identified by the appearance of a cholesteric stripe texture of the sample under cross-polarizers (**Figure 4.7**). The N^* phase persists up to a DNA concentration of 287.2 mg/ml , with the q_{DNA} peak moving slowly towards higher q values. Striking different is the appearance of small-angle ($q < 1.0 \text{ nm}^{-1}$) scattering peaks for DNA concentration of 298.1 mg/ml , as can be seen in **Figure 4.8d**. The corresponding SAXS profile displays two distinguishable peaks centered at $q/q^* = 1:2$, providing conclusive evidence that SC-60-duplex_6T have self-

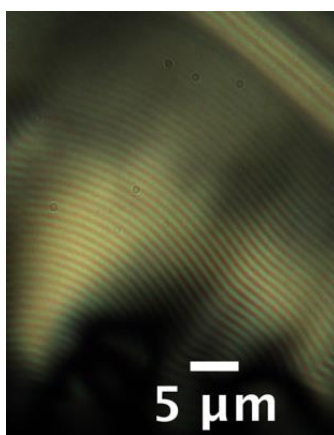


Figure 4.7 Typical cholesteric stripe texture of one-phase liquid crystalline sample with concentrations close to I/N^* coexistence observed with polarization optical microscopy (POM) for SC-60-duplex_6T.

assembled into a smectic phase with distance between neighboring layers of $d = 2\pi/q^* = 22.5 \text{ nm}$. The observed layer spacing nicely matches the duplex length L of

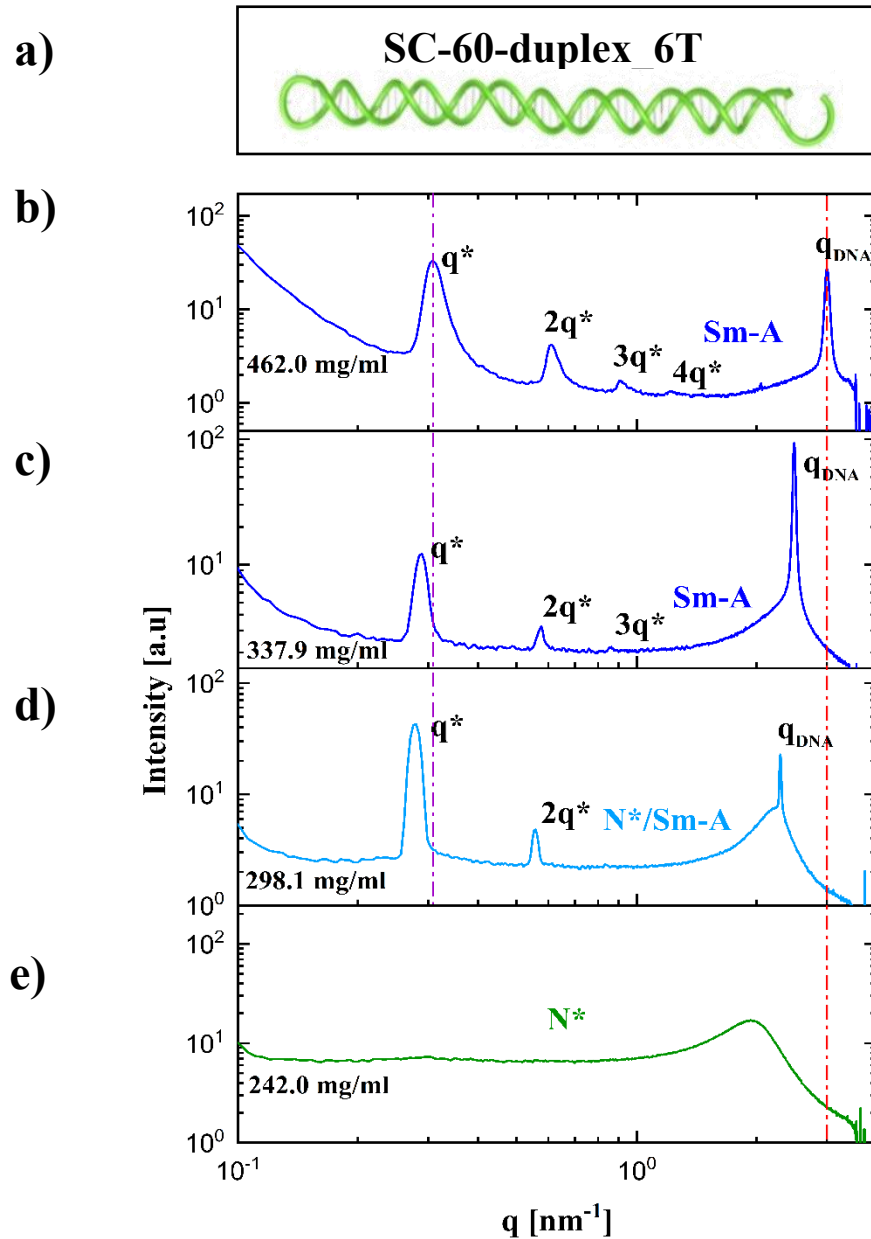


Figure 4.8 *a)* A schematic representation of the SC-60-duplex_6T *b)* X-ray scattering profile of SC-60-duplex_6T at concentration $\gamma = 462 \text{ mg/ml}$, that corresponds to a Sm-A ordering. The dashed red line is centred around the high q_{DNA} peak, while the purple line is centred around the principal q^* peak and both show how these peaks shift towards lower q -values when the concentration decreases. *c)* The dark blue curve at the concentration of 337.9 mg/ml shows a typical smectic x-ray scattering profile and corresponds to Sm-A type of ordering. *d)* 1D-SAXS profile of concentration 298.1 mg/ml that shows the coexistence between broad and sharp high q peak and corresponds to $N^*/\text{Sm-A}$ ordering. *e)* The green curve corresponds to the one-phase N^* with the concentration of 290.3 mg/ml .

one SC-60-duplex_{6T} molecule ($L_{SC-60-duplex_{6T}} = 60bp \times 0.33 \text{ nm/bp} = 19.8 \text{ nm}$). The difference between the above-mentioned characteristic lengths ($d - L_{SC-60-duplex_{6T}} = 2.1 \text{ nm}$) corresponds to the presence of the duplex-end modifications (loop and tail). Information regarding the molecular organization of the SC-60-duplex_{6T} molecules within the smectic layers can be extracted by the visual inspection of the corresponding 2D-SAXS pattern (**Figure 4.9**) of a partially aligned sample by shear. The high-angle reflections associated to correlations along the symmetry axis of SC-60-duplex_{6T} (arcs close to the beam stop) are oriented exactly perpendicular to the small-angle reflections which originate from correlations in duplex diameter (the outer broad arc, which corresponds to the q_{DNA} peak in the 1D-SAXS profile). This reveals that the SC-60-duplex_{6T} system self-organized in a smectic-A (*Sm-A*) type of mesophase. Also, a particularly intriguing observation is that in the q -region around the q_{DNA} peak, a single intense and narrow X-ray Bragg reflection superimposed with a broad peak reminiscent of the N^* phase (**Figure 4.8d**). This suggests the coexistence of a $N^*/Sm-A$ phase.

Upon further increasing of the DNA concentration to 337.9 mg/ml , the corresponding SAXS profile reveals the formation of a *Sm-A* phase with a significant long-range order as evidenced by the presence of a third higher order reflection at $q/q^* = 3$. (see **Figure 4.8c**) We also observed a shrinkage in the smectic layer thickness ($d = 22.0 \text{ nm}$) which persists at notably high DNA concentrations (a decrease from 22.0 to 20.6 nm on increasing the DNA concentration from 350.8 to 462.0 mg/ml (**Figure 4.8b**)) without any evidence of a columnar (*Col*) phase. The smectic periodicity for the highly concentrated solution ($d = 20.6 \text{ nm}$, $c = 462.0 \text{ mg/ml}$) indicates that the thickness of the smectic layers approach almost the duplex length of the SC-60-duplex_{6T} molecule, suggesting that the all-DNA loop and tail are highly compressed.

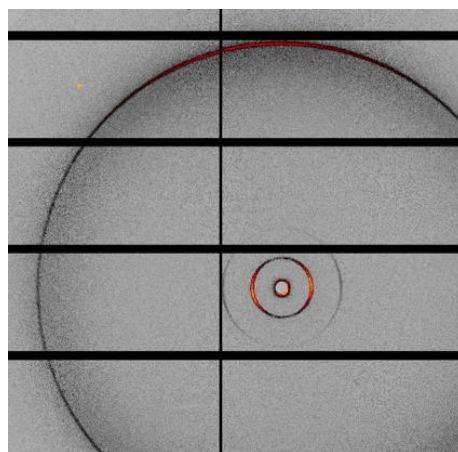


Figure 4.9 2D-SAXS pattern for a shear-aligned sample of the SC-60-duplex_{6T} system at a DNA concentration of 298.1 mg/ml . The red color corresponding to the highest intensity.

The abovementioned concentration-dependent LC phase sequence is found to be similar for all-DNA rods with shape anisotropy down to $L/D = 5.4$. This is demonstrated in **Figure 4.10** by a series of SAXS profiles acquired at different DNA concentrations for the SC-33-duplex_6T system. The depolarized image of the sample (shown in **Figure 4.10a**), taken close to two-phase coexistence (I/N^*), region is presented in **Figure 4.11**. Comparison with the corresponding POM image for SC-60-

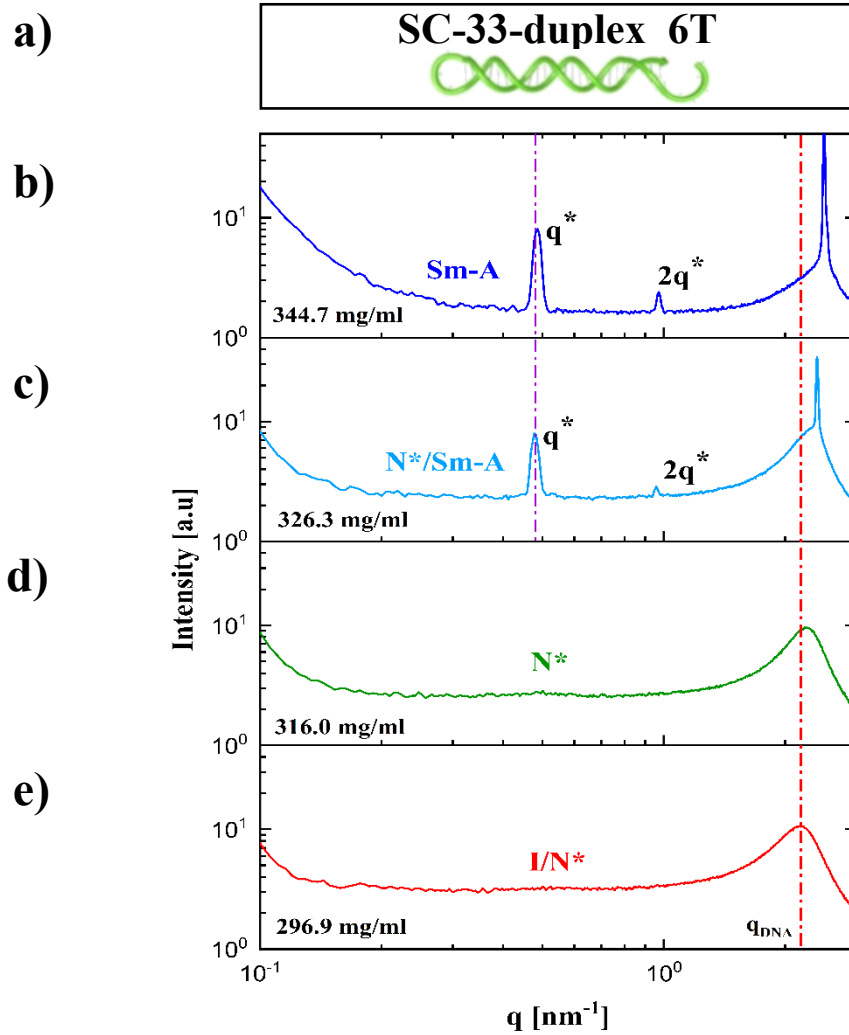


Figure 4.10 **a)** A schematic representation of SC-33-duplex_6T **b)** X-ray scattering profile of the SC-33-duplex_6T at the concentration of 344.7 mg/ml, that shows a typical smectic profile and corresponds to the Sm-A type of ordering. The purple dashed line across the panels **b)** and **c)** enables an easier observation of the concentration dependence of the principle smectic q^* peak. **c)** 1D-SAXS scattering profile of SC-33-duplex_6T at the concentration of 326.3mg/ml, where the coexistence between broad and sharp peak indicates $N^*/Sm-A$ ordering. **d)** The green curve corresponds to the one-phase N^* with the concentration of 316.0 mg/ml. **e)** The scattering curve taken from the birefringent region of the coexistent sample which corresponds to the total DNA concentration of 296.9 mg/ml

duplex_6T (**Figure 4.9**) indicates that the distance between the bright stripes becomes larger by decreasing the duplex length. This suggests that upon decreasing the aspect ratio the cholesteric pitch (P) becomes longer. This finding is in agreement with similar studies on filamentous viruses' suspensions⁵, which indicate the following dependence of the pitch with the length ($L_{fd-virus}$) of the virus at a given concentration $P \sim 1/L_{fd-virus}^{0.25}$. Finally, at high densities, a stable $Sm-A$ phase is formed (top two panels of **Figure 4.10**) with smectic layer thickness of $d = 2\pi/q^* = 13.0 \text{ nm}$, which is quite close to the length of one SC-33-duplex_6T molecule ($L_{SC-33-duplex_6T} = 10.9 \text{ nm}$).

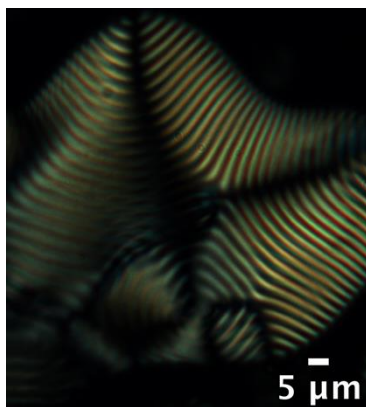


Figure 4.11 Polarization optical microscopy (POM) for SC-33-duplex_6T taken within the liquid crystalline phase, close to the I/LC coexistence.

Slightly different, however, is the concentration-dependent phase behavior of all-DNA rods on further decreasing their aspect ratio. For $L/D = 4.95$, the SC-30-duplex_6T system exhibits a I/N^* coexistence. The 1D-SAXS profile taken from the birefringent region (bottom liquid phase) of a SC-30-duplex_6T solution at total DNA concentration of 311.44 mg/ml that exhibits two-phase coexistence (see **Figure 4.12c**), together with the corresponding POM image (right image in **Figure 4.12c**) indicate that the liquid crystalline region is a cholesteric phase. However, we were not able to detect a single-phase nematic since further increase of concentration (**Figure 4.12b**) reveals the formation of a $Sm-A$ phase with the position of the primary peak q^* corresponds to a layer structure with a spacing between adjacent layers of $d = 2\pi/q^* = 11.9 \text{ nm}$. This layer spacing is in good agreement with the duplex length of the SC-30-duplex_6T molecule ($L_{SC-30-duplex_6T} = 9.9 \text{ nm}$). Based on these data, we conclude that the concentration range of a single phase nematic in solution of the SC-30-duplex_6T is rather narrow.

The expansion of the smectic region at the expense of the nematic phase by decreasing the aspect ratio of the all-DNA rods is further supported by the phase behavior of SC-28-duplex_6T. Contrary to the SC-30-duplex_6T where a I/N^* coexistence occurs at the transition from isotropic to liquid crystalline phase, the SC-28-duplex_6T undergoes an isotropic-to-smectic phase coexistence upon increasing the

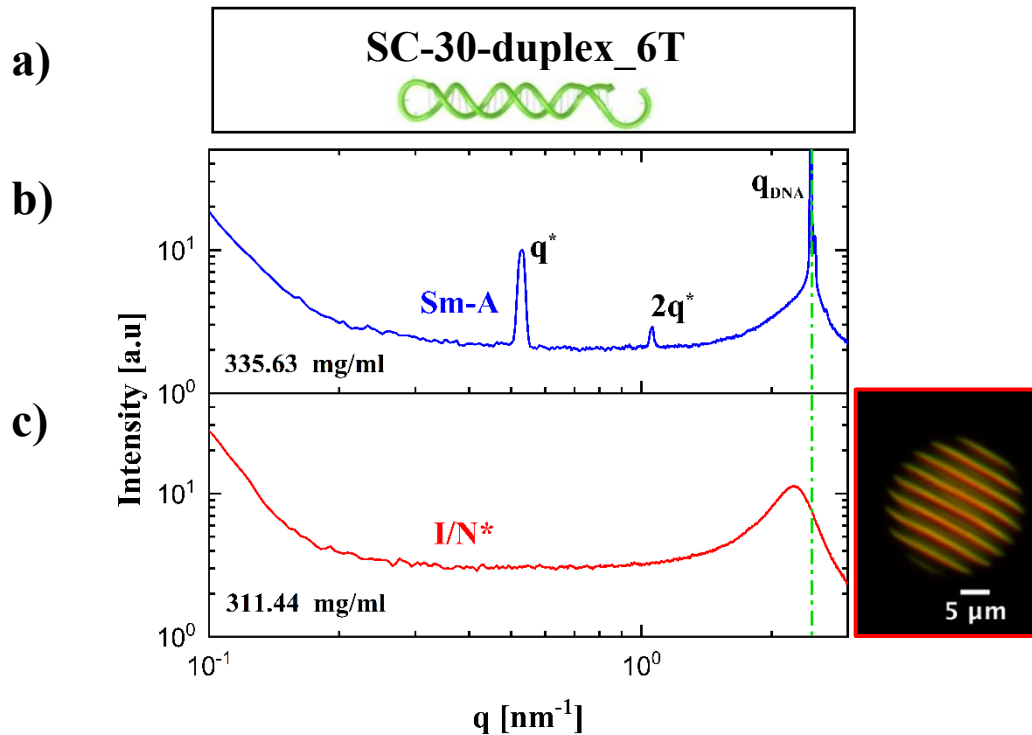


Figure 4.12 *a)* A schematic representation of SC-30-duplex_6T *b)* 1D-SAXS profile at 20°C for the SC-30-duplex_6T, with the total DNA concentration of 335.6 mg/ml (one-phase birefringent sample), which corresponds to the Sm-A ordering. *c)* X-ray scattering profile of the birefringent region for a two-phase (isotropic-liquid crystalline) coexistence sample at the concentration of 311.44 mg/ml. The red rectangle on the right: Representative POM image of the SC-30-duplex_6T liquid crystalline tactoid. This is an isotropic-nematic domain which nucleates from an unstable isotropic phase exhibiting a uniaxial cholesteric configuration of the director field under homeotropic boundary conditions.

DNA concentration. A combination of SAXS measurements and birefringent textures of the samples as recorded by POM undoubtedly confirms this intriguing phase transition. The 1D-SAXS profiles taken from the birefringent region of the two-phase coexistence sample (**Figure 4.13d**) and the one-phase liquid crystalline sample (**Figure 4.13c**) show a smectic-A type of ordering with $d = 2\pi/q^* = 11.2 \text{ nm}$. Consistent with previous findings from self-assembly of longer all-DNA rods, the layer spacing in the smectic phase is in reasonably good agreement with the molecular length of one SC-28-duplex_6T ($L_{\text{SC-28-duplex}_6T} = 9.2 \text{ nm}$). It is particularly important to emphasize that the spot-like appearance of the corresponding 2D-SAXS pattern (right side of the **Figure 4.13d**) suggests the presence of large monodomains in our samples. Furthermore, the *I/Sm-A* coexistence is attested by the absence of the characteristic stripe texture of the sample under cross-polarizers. In **Figure 4.13b**, the POM image of the above-mentioned two-phase coexistence sample confined in a 30 μm thickness-wall

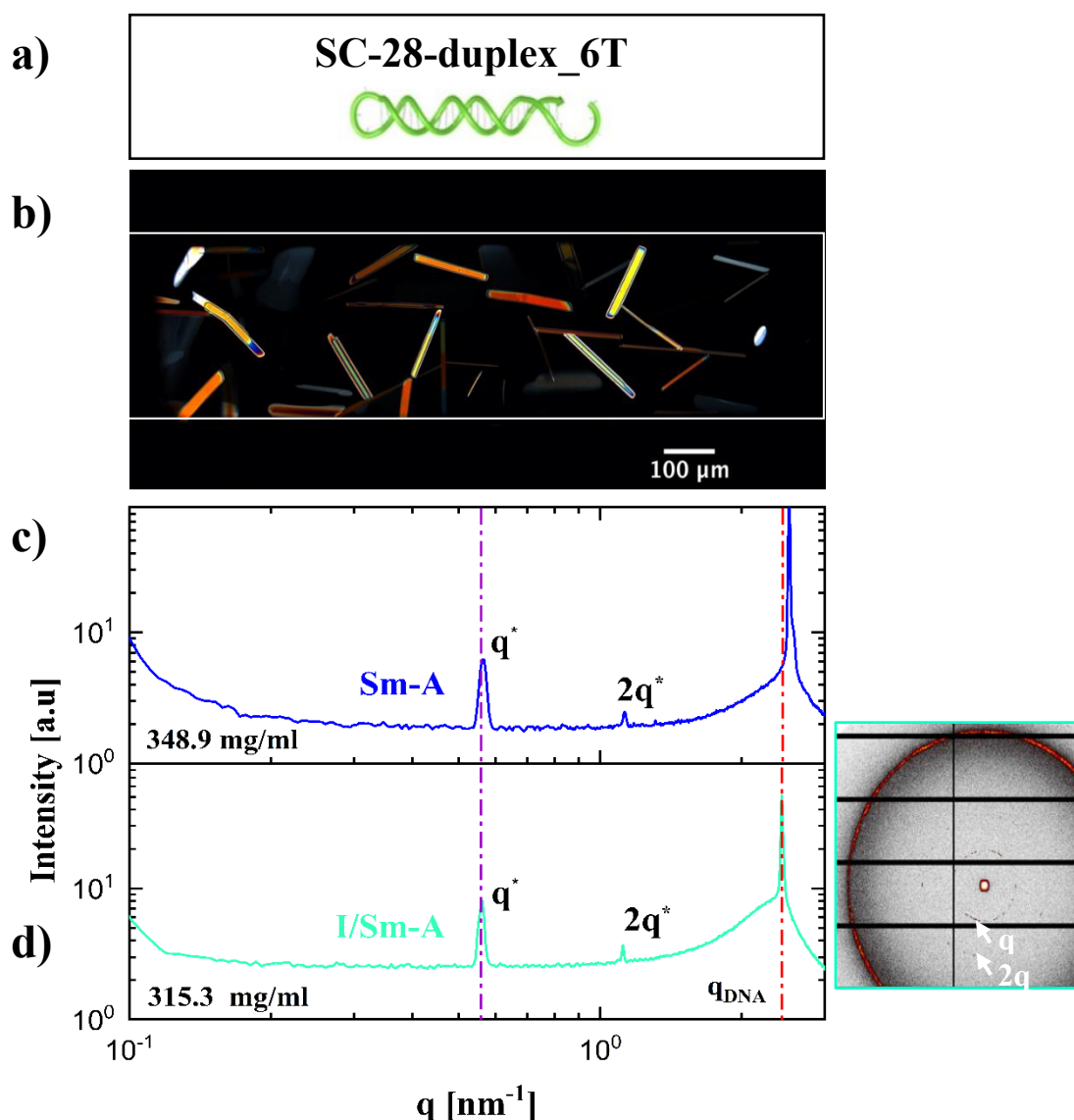


Figure 4.13 **a)** A schematic representation of SC-28-duplex_6T **b)** POM image of a highly elongated board-like tactoids in the two-phase coexistence sample (I/Sm-A), confined in a 30 μm thick glass-capillary **c)** 1D-SAXS profiles at 20°C for the SC-28-duplex_6T, with the total DNA concentration of 348.9 mg/ml, shows the Sm-A ordering. **d)** X-ray scattering profile of a birefringent region for a two-phase (isotropic-smectic) coexistence sample. 2D-SAXS pattern on the right shows the appearance of spots instead of inner arcs, which correspond to the presence of large monodomains in the sample. The dashed red line is centred around the high q_{DNA} peak, while the purple line is centred around the principal q^* peak and both show how these peaks shift towards higher q -values when the concentration is increased.

glass capillary, reveals the formation of highly elongated board-like tactoids. The background is dark because the tactoids float in the coexisting isotropic liquid phase. These high-aspect-ratio tactoids are smectic liquid crystal monodomains as demonstrated by the optical texture of a homogeneous tactoid with uniform change in brightness when the tactoid is rotated clockwise with respect to polarizer by

approximately 9 degrees step. A perfect extinction is observed when the tactoids are aligned along the polarizer or analyzer direction, as depicted in most right panel of **Figure 4.14**. In addition, in the **Figure 4.15**, time-lapse POM images of the early stage of isotropic-smectic phase separation show an intriguing nucleation-and-growth pathway of these tactoids form a spindle shaped-microdroplets spontaneously nucleated in the isotropic phase. This process continues until macroscopic phase separation is reached through coalescence and sedimentation.

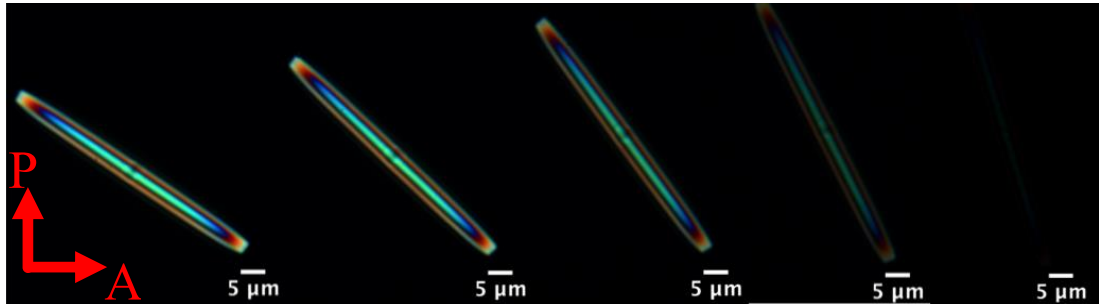


Figure 4.14 Rotation of a smectic SC-28-duplex_6T tactoid in a flat glass capillary with wall thickness of 30 μm under cross polarizers. The most left image corresponds to tactoid with the brightest transmission at 45° with respect to polarizer.

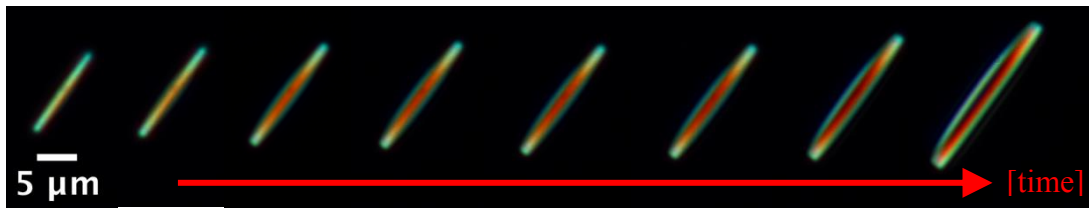


Figure 4.15 POM images of homogenous smectic tactoid which nucleates from an unstable isotropic phase in an aqueous solution of SC-28-duplex_6T. Time images were acquired every 10sec.

At further decreasing rod's aspect ratio L/D , our DNA construct design proved to be unstable. The shortest stable all-DNA purely repulsive rod that we were able to fabricate was a modified SC-duplex with $L/D = 3.3$ (SC-20-duplex_6T). Electrophoresis experiments on rods with the duplex length, L below 20 bp revealed a concentration-dependent aggregation behaviour similar to the case of FC-duplex system (**Figure 4.2**). Nevertheless, the investigation of self-assembly of the SC-20-duplex_6T system revealed a peculiar concentration-dependent phase behaviour in this low L/D region. The main findings are summarized in **Figure 4.16**, through a combined presentation of SAXS and POM measurements at selected DNA concentrations. With increasing SC-20-duplex_6T concentration, a two-phase coexistence appears at the transition from isotropic to liquid crystalline phase. The POM image taken in the biphasic region (see the right panel in **Figure 4.16b**) reveals the presence of high-aspect-ratio tactoids similar to the SC-28-duplex_6T case (POM image in **Figure 4.13b**), suggesting an isotropic-to-smectic phase transition. Indeed, the solution becomes fully liquid

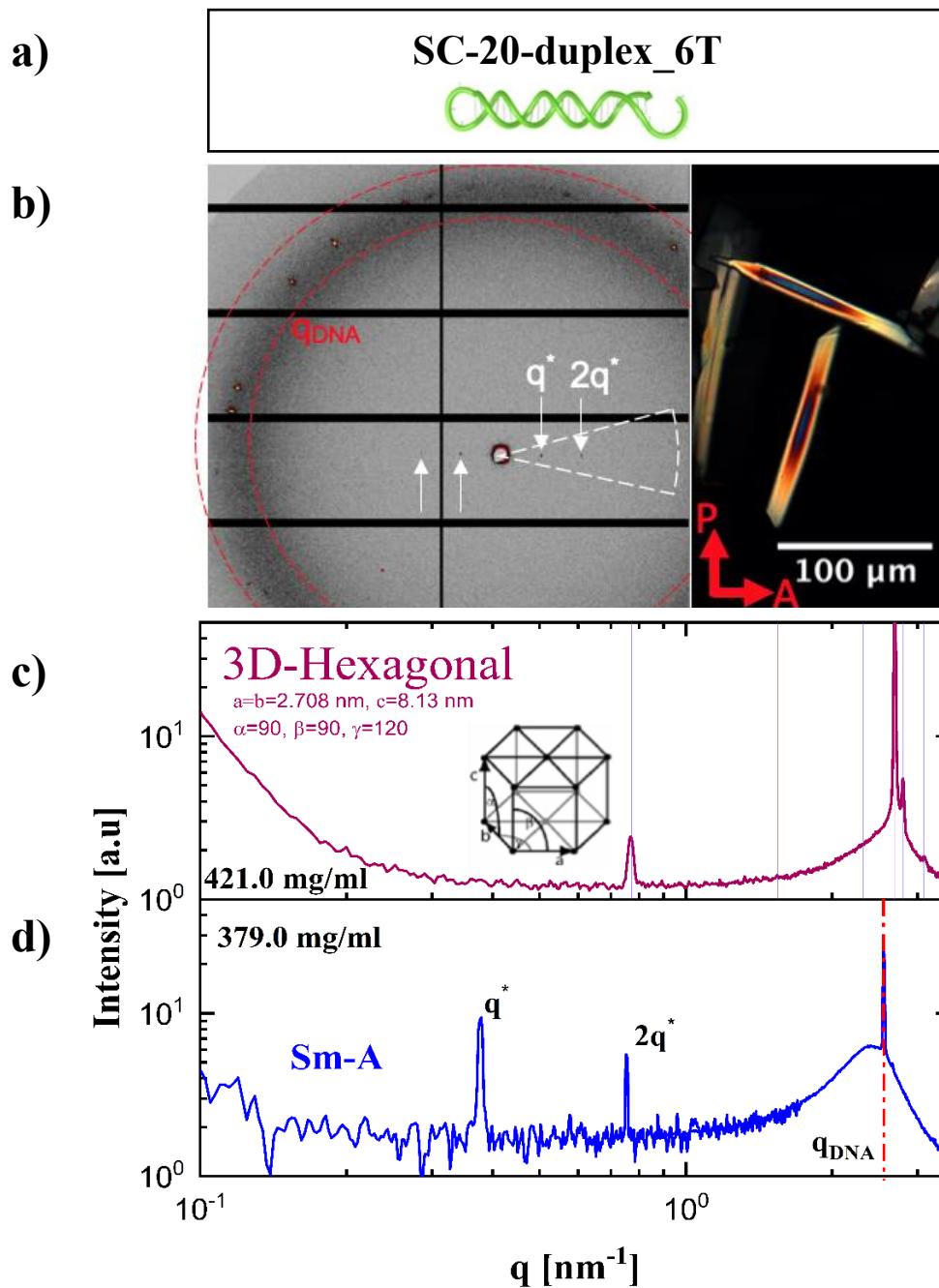


Figure 4.16 *a)* A schematic representation of SC-20-duplex_6T *b)* Left panel: 2D-SAXS pattern where a diffuse ring with clear diffraction spots at large angles is marked with the red ring, while the set of two intense spots at small angles is marked with white arrows. Right panel: POM image taken in the biphasic region of the sample showing high-aspect-ratio tactoids, suggesting an I/Sm-A transition. *c)* 1D-SAXS profile for the system SC-20-duplex_6T, at the total DNA concentration of 421.0 mg/ml showing formation of the 3D-hexagonal lattice, which is presented in the inset where the dimensions of the hexagonal cell units a, b and c are marked on the left side of the panel. Blue lines show the typical positions of the Bragg reflections for the 3D-hexagonal lattice. *d)* X-ray scattering profile at the concentration of 379.0 mg/ml that shows Sm-A ordering. The red dashed line is centred around the high q_{DNA} peak.

crystalline at DNA concentration of 379.0 mg/ml and the corresponding SAXS profile (**Figure 4.16d**) exhibits smectic peaks following the ratio $q/q^* = 1:2$. The noisy data at scattering wave vector values $q \leq 1.0 \text{ nm}^{-1}$ is due to the type of circular averaging of the 2D-SAXS pattern which is depicted in the left panel of **Figure 4.16b**. The corresponding X-ray pattern shows one diffuse ring decorated with clear diffraction spots at large angles (q_{DNA} peak, red ring area in the left panel of **Figure 4.16b**) and one set of two intense spots at small angles (white arrows in the left panel of **Figure 4.16b**). The latter corresponds to the layer structure and a typical circular averaging will result to significant smoothing or even disappearance of the observed smectic spots in the computed 1D-SAXS profile. Therefore, the 1D-SAXS profile presented in **Figure 4.16d**, is obtained by averaging all directions of radially symmetrical 2D pattern for $q \geq 0.8 \text{ nm}^{-1}$ and only the white cake-like region for $q \leq 0.8 \text{ nm}^{-1}$ (left panel, **Figure 4.16b**). Contrary to SC-28-duplex_6T system, the observed smectic layer spacing, extracted from the position of the first and most intense diffraction peak q^* , is close enough to the length of two SC-20-duplex_6T molecules ($d = 2\pi/q^* = 16.6 \text{ nm}$, $L_{SC-20-duplex_6T} = 6.6 \text{ nm}$). This implies a molecular packing scenario in which SC-20-duplex_6T dimers are arranged in a coaxial stacking manner within the layers, with their long molecular axis to be oriented orthogonal to the layer's plane. The particular intriguing feature of this packing is that without the presence of end-to-end attractions (like in the case of SC-duplexes, **Chapter 3**) these short all-DNA purely repulsive rods prefer the aspect ratio enhancement upon dimerization, suggesting that smectic phase may become unstable for lengths smaller than a critical aspect ratio value. At further increasing the DNA concentration, the X-ray pattern changes and becomes more structured around the q_{DNA} peak (**Figure 4.16c**). The Bragg reflections can be indexed considering the formation of a 3D-hexagonal phase with a hexagonal unit cell dimensions of $a = b = 2.708 \text{ nm}$, $c = 8.13 \text{ nm}$ with $\alpha = \beta = 90, \gamma = 120$ (Bravais lattice in 3D, inset of the SAXS panel in **Figure 4.16c**). The values for the short and long axis of this unit cell nicely match the centre-to-centre distance of the rods and the length of the rods, respectively. It is worth mentioning that, similar 3D-hexagonal phase has been found in early SAXS studies on concentrated solutions of polydisperse blunt-ended DNA helices with contour length of the order of the persistence length.⁵²

The largest aspect ratio of the aforementioned modified SC-duplexes (SC-xx-duplexes_6T) accessible with our DNA construct design (section 4.2) was $L/D = 9.9$, which corresponds to a 60 bp long DNA duplex. This is due to restrictions on the synthesis and purification of extra-long DNA oligonucleotides. To this end, we modified the DNA duplex by capping both terminal sites with non-sticky single-stranded DNA (ssDNA) dangling tails with length of 5 thymine bases (5T). We will refer to these all-DNA rods as 5T_xx-duplex_5T, where xx indicates the number of base-pairs. The tail-modified DNA duplexes were obtained by the self-assembly of two complementary synthetic ssDNA strands in 1:1 stoichiometric ratio (red and green

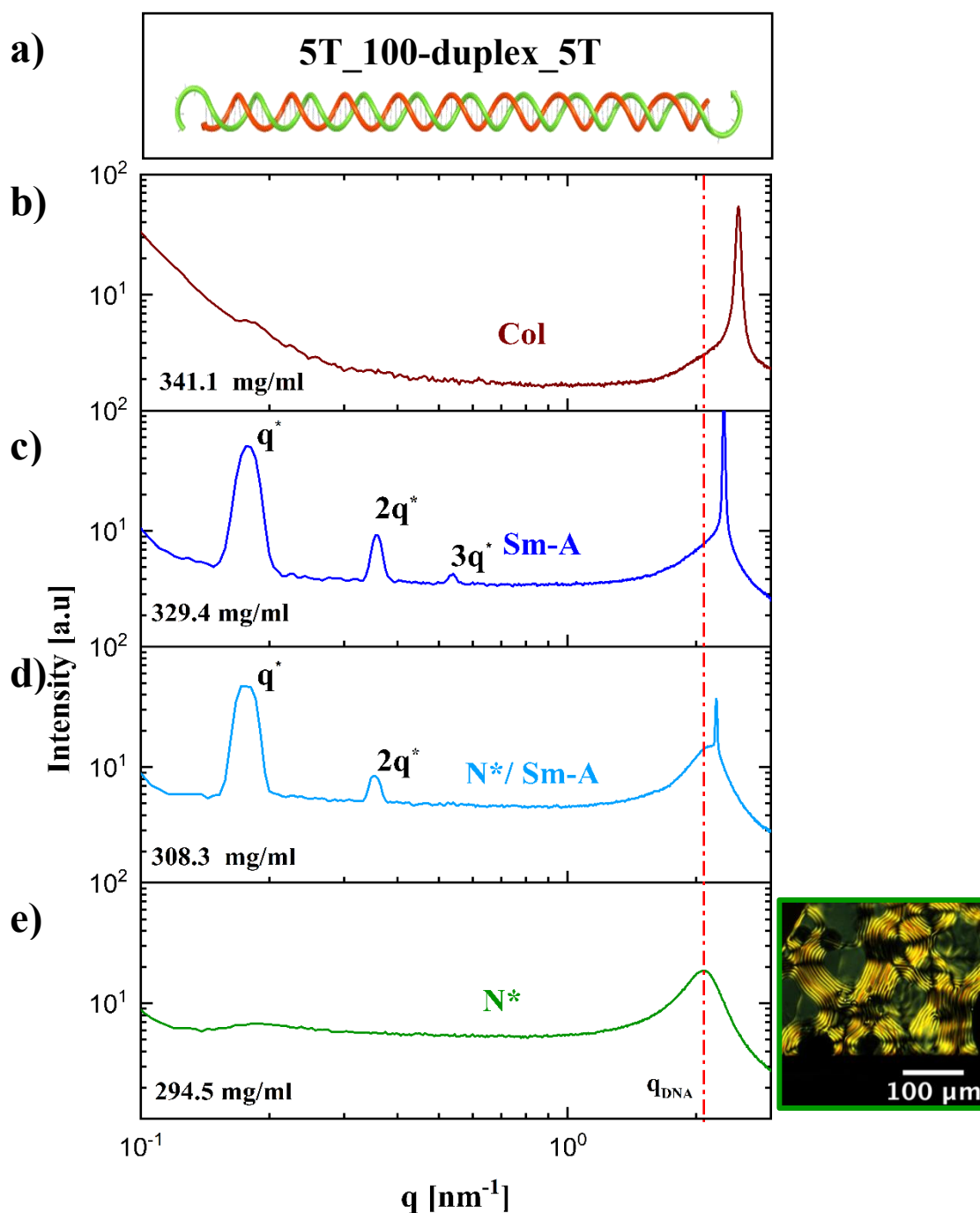


Figure 4.17 **a)** A schematic representation of the 5T_100-duplex_5T **b)** X-ray scattering profile of 5T_100-duplex_5T at concentration 341.1 mg/ml, that corresponds to a Col ordering. The dashed red line is centred around the high q_{DNA} peak and shows how this peak shift towards lower q -values when the concentration decreases. **c)** 1D-SAXS curve at the concentration of 329.4 mg/ml shows a typical smectic x-ray scattering profile and corresponds to a Sm-A type of ordering. **d)** 1D-SAXS profile of concentration 308.3 mg/ml that shows the coexistence between broad and sharp high q peak and corresponds to $N^*/$ Sm-A ordering. **e)** The green curve corresponds to the one-phase N^* with the concentration of 290.3 mg/ml. The POM image in the square on the right presents a typical fingerprint texture for a nematic ordering.

ssDNA sequences in **Figure 4.17a**). We have synthesized a stable 5T_100-duplex_5T which corresponds to an all-DNA rod with duplex contour length $L_{5T_{100}\text{-duplex}_{5T}} = 33.0 \text{ nm}$ and aspect ratio $L/D = 17.0$. 1D-SAXS data, at room temperature for the 5T_100-duplex_5T, are shown in **Figure 4.17** for concentrations well above the two-phase coexistence region. Similar to the SC-60-duplex_6T system, the sequence of phase transitions from lower to higher DNA concentrations ($I/N^*/Sm-A$) remains unchanged (**Figure 4.17c,d** and **e**). In addition, the observed smectic layer spacing $d = 2\pi/q^* = 35.7 \text{ nm}$ as extracted from the position of the first and most intense diffraction peak q^* , matches the length of one 5T_100-duplex_5T molecule. We find, however, that on further increasing the 5T_100-duplex_5T concentration, a transition from Sm-A to columnar (*Col*) phase is obtained (**Figure 4.17b**), which could suggest that *Col* ordering is dependant from the aspect ratio of the rod.

4.3.2 Phase diagram of purely repulsive all-DNA rods

The SAXS and POM measurements described in the previous section served as the basis for determining the phase behaviour of the all-DNA rod-like constructs. The properties of the systems of nanosized DNA rods that were used in this thesis are summarized in **Table 4.1**.

System name	Number of base pairs	Aspect ratio (L/D)	Effective aspect ratio $(L/D)_{eff}$	Molecular weight (g/mol)
5T_100-duplex_5T	100	16.5	14.58	64 730
SC-60-duplex_6T	60	9.9	9.08	40 364
SC-48-duplex_6T	48	7.92	7.43	32 637
SC-40-duplex_6T	40	6.6	6.33	27 998
SC-36-duplex_6T	36	5.94	5.78	25 528
SC-33-duplex_6T	33	5.45	5.37	23 674
SC-30-duplex_6T	30	4.95	4.96	21 820
SC-28-duplex_6T	28	4.62	4.68	20 584
SC-26-duplex_6T	26	4.29	4.41	19 349
SC-24duplex_6T	24	3.96	4.13	18 112
SC-20-duplex_6T	20	3.3	3.58	15 645

Table 4.1 System parameters of the nanosized all-DNA rods that were used in this study. Here, $(L/D)_{eff}$ is the effective aspect ratio, assuming $L_{eff} = L + 2 \text{ nm}$ and $D_{eff} = 2.4 \text{ nm}$

The phase diagram of all-DNA rods, as a function of the shape anisotropy L/D and the total DNA concentration, is presented in **Figure 4.18** (top panel). The phase boundaries of six (6) different phases were identified: the isotropic (I), the chiral nematic (N^*), the monolayer smectic (Sm_m-A), with layer thickness comparable to one rod length, the bilayer smectic (Sm_b-A), with layer thickness comparable to two rod lengths, the columnar (Col) and the crystalline phase with orientationally ordered lattice (3D-hexagonal). In the bottom panel of **Figure 4.18**, the phase behaviour of all-DNA rods is depicted as a function of the $\log(L/D + 1)$ in order to offer a clearer view of the phase diagram region corresponding to the systems with low aspect ratio. It is found that the one-phase liquid crystalline N^* is stable from about $L/D \approx 5.6$. The I/N^* coexistence shifts towards lower concentrations with an increase of L/D (black dashed line in **Figure 4.18**). The $Sm-A$ phase becomes stable at $L/D \approx 4$. The $I/Sm-A$ transition occurs as a strong first order transition for $3.96 \leq L/D \leq 4.62$, which is evidenced by the presence of a noticeable $I/Sm-A$ biphasic concentration region. The $N^*/Sm-A$ transition starts off, without any evidence of a coexistence, for $L/D \geq 5.45$, and the DNA concentration at which this transition occurs is nearly L/D -independent (blue dashed line in **Figure 4.18**). However, when we consider the dependence of the I/N^* coexistence on L/D , shown in the phase diagram of **Figure 4.18**, we clearly see that the DNA concentration width at which the N^* phase is stable becomes narrower as the L/D decreases. At the $L/D = 4.95$, the birefringent phase in the isotropic-to-liquid crystal coexistence is found to be the N^* phase with no evidence of stable one-phase N^* . The $Sm-A$ persists at notably high DNA concentrations ($c \sim 470 \text{ mg/ml}$) for moderate aspect ratios ($8 \leq L/D \leq 10$). Although in the phase diagram of **Figure 4.18** the very concentrated region in the aspect ratio region $4.3 \leq L/D \leq 8.0$ is not explored, this does not exclude the possibility that $Sm-A$ might occur at higher DNA densities. However, an intriguing observation is that, while further increasing the DNA concentration at high aspect ratios ($L/D = 16.5$), a transition from $Sm-A$ to Col is obtained. Concerning the low aspect ratio region ($3.3 \leq L/D \leq 4.62$) of **Figure 4.18** the isotropic-to-smectic transition density abruptly increases as the L/D decreases. Finally, it is particularly important to note that also a 3D-hexagonal phase is observed for the aspect ratios $L/D = 3.3$ and $L/D = 3.96$. Furthermore, for $L/D = 3.3$, the calculated smectic layer thickness revealed an unconventional packing scenario within the smectic layers, in which the purely repulsive all-DNA rods are arranged in a coaxial stacking manner, resulting in the formation of dimers (Sm_b-A).

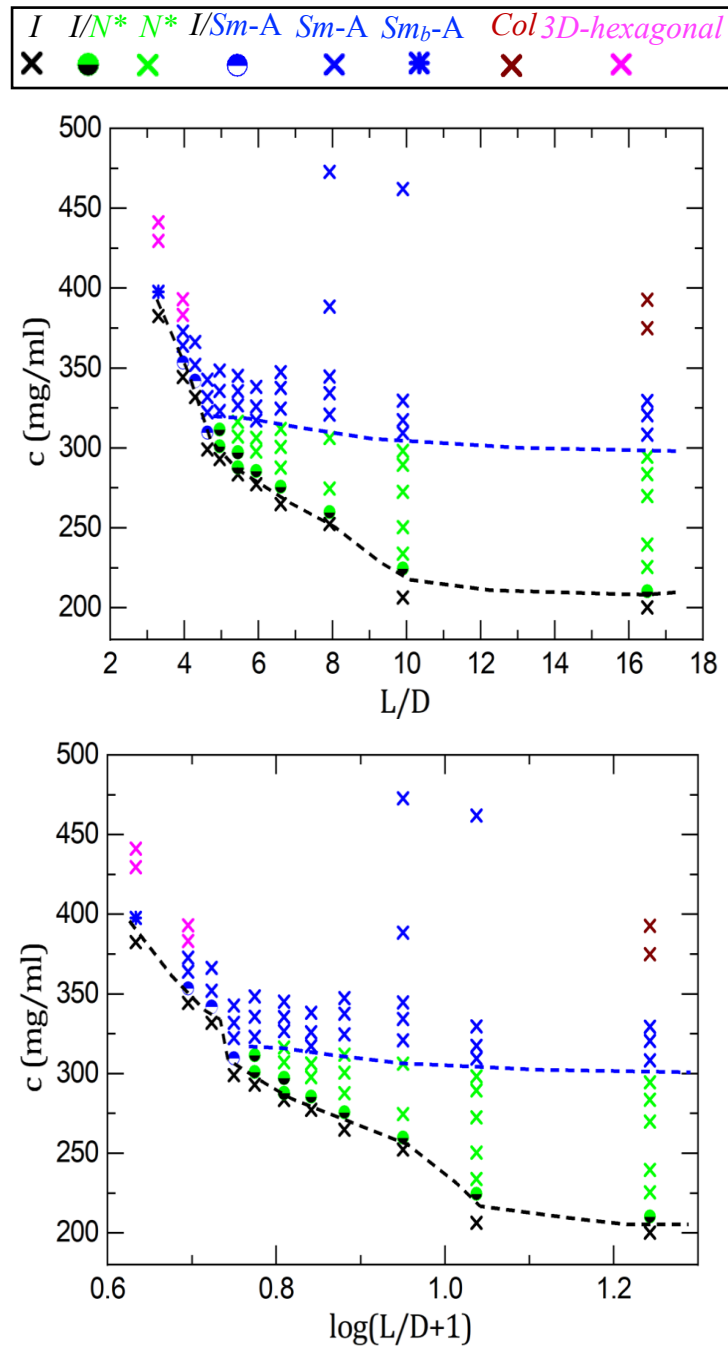


Figure 4.18 Experimental phase diagram of purely repulsive all-DNA rods with L/D between 3 and 17. In order to clearly demonstrate the phase behaviour in the low aspect ratio region $L/D < 5$, the phase diagram in the top is replotted (bottom: DNA concentration c as a function of $\log(L/D + 1)$). The black and blue dashed lines are added to assist identifying the transitions from isotropic (I)-to-chiral nematic (N^*) and chiral nematic N^* to-smectic ($Sm-A$), respectively. The following one-phase liquid crystalline phases were found (listed on the top of the figure): I (isotropic), N^* (chiral nematic), Sm_m-A (smectic A-type with monolayer morphology), Sm_b-A (smectic A-type with bilayer morphology), columnar (*Col*) and 3D-hexagonal. Two-phase coexistence: isotropic/chiral nematic (I/N^*) and chiral nematic/smectic-A ($N^*/Sm-A$).

Aiming to obtain a direct comparison of our experimental results of all-DNA rods with the phase behaviour of hard-core spherocylinders computed by Bolhuis and Frenkel¹⁶, we used the phase diagram re-plotted by Dussi²⁰ as the packing fraction η versus aspect ratio L/D (**Figure 4.19**). To account for the electrostatic repulsion and the DNA contour

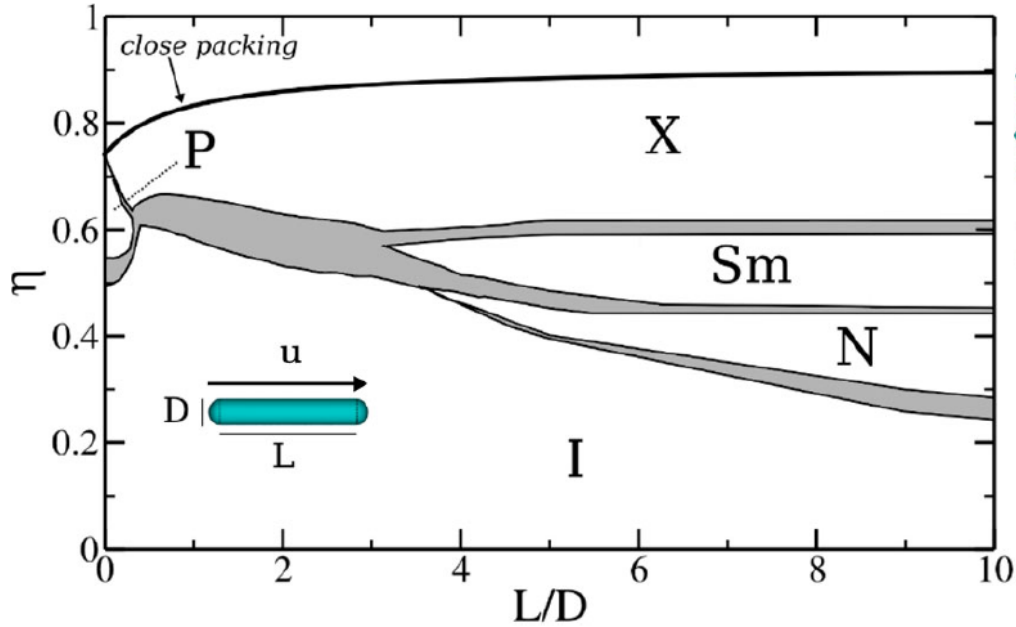


Figure 4.19 Phase diagram of hard spherocylinders of aspect ratio $L/D \leq 10$, adapted from ref. [20]. All two-phase regions are shown shaded. The following stable phases can be distinguished: Isotropic (I), nematic (N), smectic (Sm), crystal (X) and plastic crystal (P).²⁰

length extension due to the presence of ssDNA-based modifications at the terminal sites of the DNA duplex, an effective rod diameter D_{eff} and rod length L_{eff} are employed for the re-calculation of the all-DNA rods aspect ratio $(L/D)_{eff}$ and volume fraction φ_{eff} . The effective length L_{eff} was assumed to be $L + 2 \text{ nm}$. A contour length extension of 1 nm per duplex's terminal site is quite reasonable because it takes into account the contributions of the 5 thymine hairpin loop on one side and of the 6 thymine tail on the other. For the effective diameter D_{eff} , the value of 2.4 nm is chosen. This value is slightly larger than the steric diameter of DNA and it is found to offer a very good matching between experimental and numerical phase boundaries in the system of SC-duplexes presented in **Chapter 3**. The effective volume fraction reads

$$\varphi_{eff} = \frac{c N_A \left(\frac{D_{eff}}{2}\right)^2 L_{eff}}{M_w}$$

where c represents the DNA concentration, N_A the Avogadro's number and M_w the molecular weight of the all-DNA construct. In **Figure 4.20**, the experimental phase diagram shows many striking similarities with the above-mentioned phase diagram of hard spherocylinders. For simplicity, only the phase boundaries of the latter, together

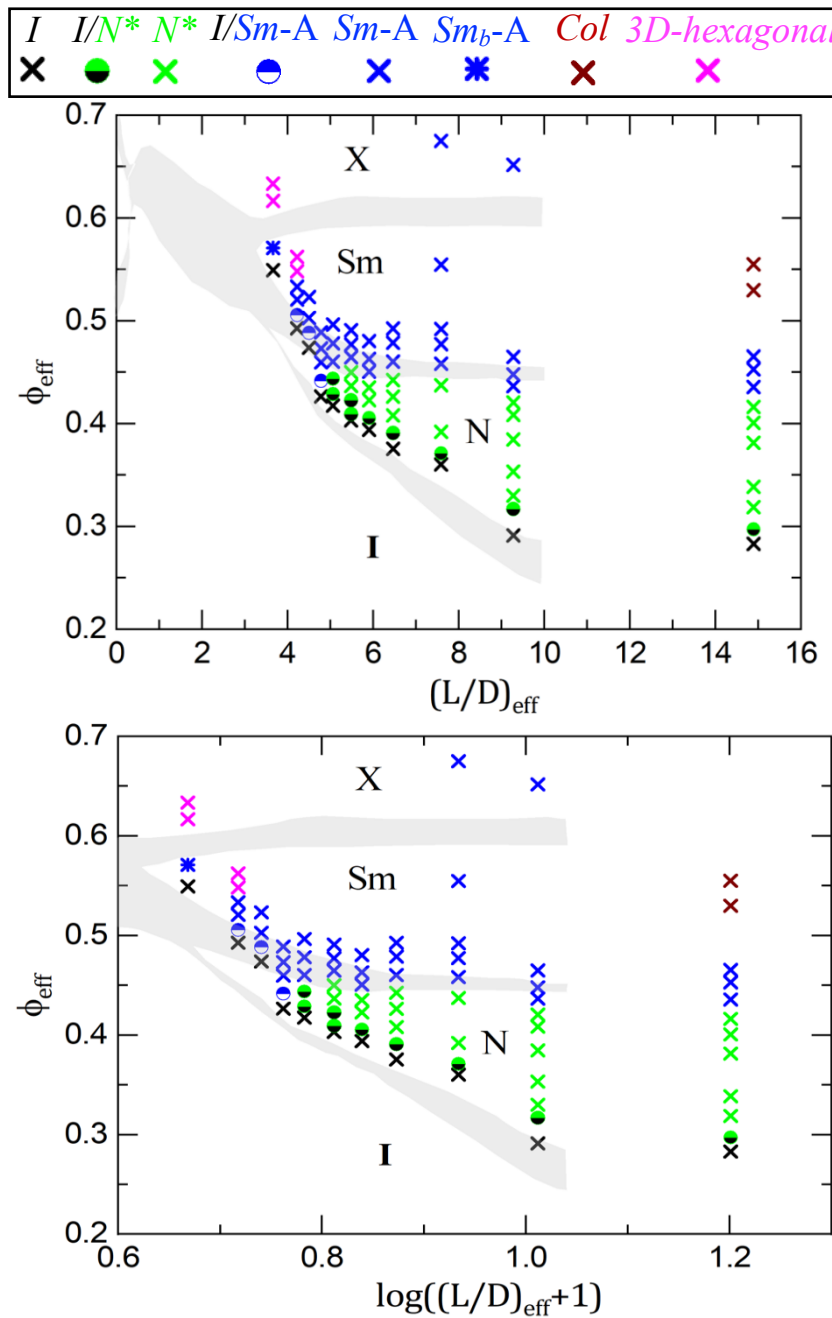


Figure 4.20 Experimental phase diagram of purely repulsive all-DNA rods depending on effective aspect ratio $(L/D)_{\text{eff}}$ and volume fraction. The rod's length L is corrected for the hairpin and the 6T tail terminal modifications and rod's diameter D is corrected for charge repulsion by taking an effective hard-rod diameter. In order to clearly demonstrate the phase behaviour in the low aspect ratio region $L/D < 5$, the phase diagram in the top is replotted (bottom: DNA concentration c as a function of $\log((L/D)_{\text{eff}} + 1)$). The experimental one-phase liquid crystalline phases are listed on the top of the figure: I (isotropic), N^* (chiral nematic), $Sm-A$ (monolayer smectic A-type), Sm_b-A (bilayer smectic A-type), Col (columnar) and 3D-hexagonal. The grey-shaded phase boundaries together with the corresponding stable phases (isotropic: I , nematic: N , smectic: Sm , crystal: X and plastic crystal: P) belong to the phase diagram of hard spherocylinders computed by Bolhuis and Frenkel.¹⁵

with the location of the thermodynamically stable simulated phases, are presented (grey-shaded phase boundaries). Similar to simulations, the isotropic-nematic phase boundary of the experimental phase diagram exhibits the same dependence on the aspect ratio. In addition, an isotropic/smectic phase coexistence is observed at low aspect ratios. Furthermore, smectic and nematic phases were found only for $L/D \geq 4.95$. At the highest volume fractions, the simulations demonstrate a crystalline phase in a wide range of aspect ratios. In the experimental phase diagram such a crystalline phase (3D-hexagonal) is found only in the low aspect ratio region defined by $L/D \leq 3.96$. However, the most intriguing observation is that there is a quantitative agreement between experiments and simulations in the volume fraction of the abovementioned phases.

4.4 Summary and conclusions

The phase diagram of concentrated aqueous suspensions of purely repulsive all-DNA rods is thoroughly mapped as the function of the rod length and the DNA concentration. Using model systems containing stiff DNA duplexes with their blunt-end stacking interactions blocked, it is demonstrated that such DNA-based rods can be considered as an accurate experimental realization of hard spherocylinders. This is clearly supported by the [Figure 4.20](#), since the phase behaviour of repulsive all-DNA rods, with moderate salt concentrations (150 mM NaCl), overlaps with the one of a corresponding hard-core rod system. The phase diagram of all-DNA rods is explored over a wide range of DNA densities and L/D values, demonstrating a good quantitative agreement with the simulation results for the hard spherocylinder system. To summarize, the key experimental findings are: N^* is stable from about $L/D \approx 5$, the I/N^* coexistence decreases as a function of L/D , the $I/Sm-A$ coexistence becomes stable at $L/D \approx 4.6$ and the N^* -to- $Sm-A$ transition is located at almost constant DNA concentration for $4.95 \leq L/D \leq 16.5$. The system that was used in this work is unique because it allows to examine liquid crystalline phases in the hard-core rods with a remarkable aspect ratio resolution. In addition, assembly methods coming from the DNA origami technology could be employed for constructing colloidal sized all-DNA rods, allowing 3D single particle studies.

One of the most outstanding findings in the computer simulations of hard spherocylinder systems is the absence of liquid crystalline phase for very low aspect ratios. Unfortunately, this is not demonstrated in the work at hand, since the experimental system design becomes unstable for short DNA duplexes. Alternative synthetic approaches based on DNA inter-strand crosslinking agents may solve this issue, allowing access to the ultra-low aspect ratio region $L/D \leq 3$. The importance of exploring this low shape anisotropy region is already demonstrated in this work by the results of concentration-dependent self-assembly at $L/D \approx 3.3$. Besides the crystalline phase (3D-hexagonal) predicted by simulations and hereby experimentally confirmed,

an unconventional smectic phase is found. In this liquid crystalline phase, the purely repulsive rods are packed within the smectic layers as dimers. Furthermore, the discrepancy between experiments and simulations in the volume fractions of the phases for $(L/D)_{eff} \leq 4.8$, seen in [Figure 4.20](#), is not unexpected. The simulated phase diagram of rods does not only depend on L/D , but also on the exact shape of the particle. For example, a demonstration of the delicate packing constraints related to the particle shape, is the case of hard ellipsoidal particles, which do not form stable smectic phases, although hard spherocylinders are able to do so.⁵³ This should be kept in mind when comparing with experiments.

Finally, the concentration-dependent transition from *Sm-A*-to-columnar (*Col*) phase, for all-DNA rods with large aspect ratio ($L/D = 16.5$), is quite intriguing since, for $L/D \approx 10$, the *Sm-A* persists at notably high DNA concentrations ($c \sim 462 \text{ mg/ml}$). Since all-DNA rods are monodisperse and purely repulsive systems, it is interesting to determine the particle aspect ratio requirements for stabilizing, by entropy alone, this liquid crystalline phase. It is worth mentioning that *fd*-virus particles with aspect ratios significantly larger than all-DNA rods, but with similar stiffness (L/l_p , where l_p is the persistence length of DNA duplex), show stable *Col* phase. Extensive studies on this chiral rod-like particle (*fd*-virus) suggested that the flexibility may play a key factor for stabilizing this phase.⁷ However, the ability to control the length of all-DNA rods with a sub-nanometre accuracy (at a single base level) could allow to address this issue. More experiments on all-DNA rods with L/D between 10 and 16 are definitely required in order to define the aspect ratio at which the *Col* phase begins.

Bibliography

1. Onsager, L. the Effects of Shape on the Interaction of Colloidal Particles. *Ann. N. Y. Acad. Sci.* **51**, 627–659 (1949).
2. Fraden, S., Maret, G., Caspar, D. L. D. & Meyer, R. B. Isotropic-nematic phase transition and angular correlations in isotropic suspensions of tobacco mosaic virus. *Phys. Rev. Lett.* **63**, 2068–2071 (1989).
3. Dogic, Z. & Fraden, S. Smectic phase in a colloidal suspension of semiflexible virus particles. *Phys. Rev. Lett.* **78**, 2417–2420 (1997).
4. Dogic, Z. & Fraden, S. Ordered phases of filamentous viruses. *Curr. Opin. Colloid Interface Sci.* **11**, 47–55 (2006).
5. Grelet, E. & Fraden, S. What Is the Origin of Chirality in the Cholesteric Phase of Virus Suspensions? *Phys. Rev. Lett.* **90**, 198302 (2003).
6. Grelet, E. Hard-rod behavior in dense mesophases of semiflexible and rigid charged viruses. *Phys. Rev. X* **4**, 021053 (2014).
7. Grelet, E. & Rana, R. From soft to hard rod behavior in liquid crystalline suspensions of sterically stabilized colloidal filamentous particles. *Soft Matter*

- 12, 4621–4627 (2016).
8. Kuijk, A., Blaaderen, A. Van & Imhof, A. Synthesis of Monodisperse, Rodlike Silica Colloids with Tunable Aspect Ratio. *J. Am. Chem. Soc.* **133**, 2346–2349 (2011).
 9. Kuijk, A., Byelov, D. V., Petukhov, A. V., Van Blaaderen, A. & Imhof, A. Phase behavior of colloidal silica rods. *Faraday Discuss.* **159**, 181–199 (2012).
 10. Bakker, H. E. *et al.* Phase diagram of binary colloidal rod-sphere mixtures from a 3D real-space analysis of sedimentation-diffusion equilibria. *Soft Matter* **12**, 9238–9245 (2016).
 11. Stroobants, A., Lekkerkerker, H. N. W. & Frenkel, D. Evidence for Smectic Order in a Fluid of Hard Parallel Spherocylinders. *Phys. Rev. Lett.* **57**, 1452–1455 (1986).
 12. Stroobants, A., Lekkerkerker, H. N. W. & Frenkel, D. Evidence for one-, two-, and three-dimensional order in a system of hard parallel spherocylinders. *Phys. Rev. A* **36**, 2929–2945 (1987).
 13. Jover, J., Haslam, A. J., Galindo, A., Jackson, G. & Müller, E. A. Pseudo hard-sphere potential for use in continuous molecular-dynamics simulation of spherical and chain molecules. *J. Chem. Phys.* **137**, 1–13 (2012).
 14. McGrother, S. C., Williamson, D. C. & Jackson, G. A re-examination of the phase diagram of hard spherocylinders. *J. Chem. Phys.* **104**, 6755–6771 (1996).
 15. McGrother, S. C., Gil-Villegas, A. & Jackson, G. The liquid-crystalline phase behaviour of hard spherocylinders with terminal point dipoles. *J. Phys. Condens. Matter* **8**, 9649–9655 (1996).
 16. Bolhuis, P. & Frenkel, D. Tracing the phase boundaries of hard spherocylinders. *J. Chem. Phys.* **106**, 666–687 (1997).
 17. Bolhuis, P. G., Stroobants, A., Frenkel, D. & Lekkerkerker, H. N. W. Numerical study of the phase behavior of rodlike colloids with attractive interactions. *J. Chem. Phys.* **107**, 1551–1564 (1997).
 18. McGrother, S. C., Sear, R. P. & Jackson, G. The liquid crystalline phase behavior of dimerizing hard spherocylinders. *J. Chem. Phys.* **106**, 7315–7330 (1997).
 19. Avendaño, C., Gil-Villegas, A. & González-Tovar, E. Computer simulation of charged hard spherocylinders. *J. Chem. Phys.* **128**, 044506 (2008).
 20. Dussi, S., Chiappini, M. & Dijkstra, M. On the stability and finite-size effects of a columnar phase in single-component systems of hard-rod-like particles. *Mol. Phys.* **116**, 2792–2805 (2018).
 21. Bates, M. A. & Frenkel, D. Influence of polydispersity on the phase behavior of colloidal liquid crystals: A Monte Carlo simulation study. *J. Chem. Phys.* **109**, 6193–6199 (1998).
 22. Veerman, J. A. C. & Frenkel, D. Phase diagram of a system of hard spherocylinders by computer simulation. *Phys. Rev. A* **41**, 3237–3244 (1990).
 23. Veerman, J. A. C. & Frenkel, D. Relative stability of columnar and crystalline phases in a system of parallel hard spherocylinders. *Phys. Rev. A* **43**, 4334–4343

- (1991).
24. Repula, A., Oshima Menegon, M., Wu, C., Van Der Schoot, P. & Grelet, E. Directing Liquid Crystalline Self-Organization of Rodlike Particles through Tunable Attractive Single Tips. *Phys. Rev. Lett.* **122**, 128008 (2019).
 25. Naderi, S. & van der Schoot, P. Effect of bending flexibility on the phase behavior and dynamics of rods. *J. Chem. Phys.* **141**, 124901 (2014).
 26. Růžička, Š. & Wensink, H. H. Simulating the pitch sensitivity of twisted nematics of patchy rods. *Soft Matter* **12**, 5205–5213 (2016).
 27. de Braaf, B., Oshima Menegon, M., Paquay, S. & van der Schoot, P. Self-organisation of semi-flexible rod-like particles. *J. Chem. Phys.* **147**, 244901 (2017).
 28. Liu, Y. & Widmer-Cooper, A. A versatile simulation method for studying phase behavior and dynamics in colloidal rod and rod-polymer suspensions. *J. Chem. Phys.* **150**, 244508 (2019).
 29. Oshima Menegon, M., Kusters, G. L. A. & van der Schoot, P. Self-organization of tip-functionalized elongated colloidal particles. *Phys. Rev. E* **100**, 042702 (2019).
 30. Loring, H. S. & Stanley, W. M. Isolation of Crystalline Tobacco Mosaic Virus Protein From Tomato Plants. *J. Biol. Chem.* **117**, 733–754 (1936).
 31. Stanley, W. M. Isolation of a Crystalline Protein Possessing the Properties of Tobacco-Mosaic Virus. *Science*. **81**, 644–645 (1935).
 32. Bawden, F. C., Pirie, N. W., Bernal, J. D. & Fankuchen, I. Liquid Crystalline Substances from Virus-infected Plants. *Nature* **138**, 1051–1052 (1936).
 33. Oldenbourg, R., Wen, X., Meyer, R. B. & Caspar, D. L. D. Orientational distribution function in nematic tobacco-mosaic-virus liquid crystals measured by X-ray diffraction. *Phys. Rev. Lett.* **61**, 1851–1854 (1988).
 34. Graf, H. & Löwen, H. Phase diagram of tobacco mosaic virus solutions. *Phys. Rev. E - Stat. Physics, Plasmas, Fluids, Relat. Interdiscip. Top.* **59**, 1932–1942 (1999).
 35. Lapointe, J. & Marvin, D. A. Filamentous Bacterial Viruses - 8. Liquid Crystals Of fd. *Mol Cryst Liq Cryst* **19**, 269–278 (1973).
 36. Fraden, S. Phase Transitions in Colloidal Suspensions of Virus Particles. in *Observation, Prediction and Simulation of Phase Transitions in Complex Fluids* (eds. Baus, M., Rull, L. F. & Ryckaert, J.-P.) 113–164 (Springer Netherlands, 1995). doi:10.1007/978-94-011-0065-6_3.
 37. Dogic, Z. Filamentous Phages As a Model System in Soft Matter Physics. *Front. Microbiol.* **7**, 1–7 (2016).
 38. Grelet, E. Hexagonal Order in Crystalline and Columnar Phases of Hard Rods. *Phys. Rev. Lett.* **100**, 168301 (2008).
 39. Lettinga, M. P., Barry, E. & Dogic, Z. Self-diffusion of rod-like viruses in the nematic phase. *Europhys. Lett.* **71**, 692–698 (2005).

40. Lettinga, M. P. & Grelet, E. Self-Diffusion of Rodlike Viruses through Smectic Layers. *Phys. Rev. Lett.* **99**, 197802 (2007).
41. Pouget, E., Grelet, E. & Lettinga, M. P. Dynamics in the smectic phase of stiff viral rods. *Phys. Rev. E - Stat. Nonlinear, Soft Matter Phys.* **84**, 1–6 (2011).
42. Naderi, S. *et al.* Fractional hoppinglike motion in columnar mesophases of semiflexible rodlike particles. *Phys. Rev. Lett.* **111**, 17–21 (2013).
43. Kats, C. M. Van, Johnson, P. M., Meerakker, J. E. A. M. Van Den & Blaaderen, A. Van. Synthesis of Monodisperse High-Aspect-Ratio Colloidal Silicon and Silica Rods. *Langmuir* **20**, 11201–11207 (2004).
44. Luzzati, V. & Nicolaieff, A. Etude par diffusion des rayons X aux petits angles des gels d'acide désoxyribonucléique et de nucléoprotéines : (note préliminaire). *J. Mol. Biol.* **1**, 127–133 (1959).
45. Livolant, F., Levelut, A. M., Doucet, J. & Benoit, J. P. The highly concentrated liquid-crystalline phase of DNA is columnar hexagonal. *Nature* **339**, 724–726 (1989).
46. Rill, R. L., Strzelecka, T. E., Davidson, M. W. & Van Winkle, D. H. Ordered phases in concentrated DNA solutions. *Phys. A Stat. Mech. its Appl.* **176**, 87–116 (1991).
47. Livolant F. Condensed phases of DNA. *Prog Polym Sci* **21**, 1115–1164 (1996).
48. Rill, R. L. Liquid crystalline phases in concentrated aqueous solutions of Na⁺ DNA. *Proc. Natl. Acad. Sci. U. S. A.* **83**, 342–346 (1986).
49. Davidson, M. W., Strzelecka, T. E. & Rill, R. L. Multiple Liquid Crystal Phases at High DNA Concentrations. *Nature* **331**, 457–460 (1988).
50. Merchant, K. & Rill, R. L. DNA length and concentration dependencies of anisotropic phase transitions of DNA solutions. *Biophys. J.* **73**, 3154–3163 (1997).
51. Nakata, M. *et al.* End-to-End Stacking and Liquid Crystal Condensation of 6– to 20–Base Pair DNA Duplexes. *Science*. **318**, 1276–1279 (2007).
52. Durand, D., Doucet, J. & Livolant, F. A study of the structure of highly concentrated phases of DNA by X-ray diffraction. *J. Phys. II* **2**, 1769–1783 (1992).
53. Frenkel, D. Invited article computer simulation of hard-core models for liquid crystals. *Mol. Phys.* **60**, 1–20 (1987).

Chapter 5

Phase diagram of purely repulsive all-DNA chain-sticks

Recently, through a combined experimental and simulation study, a novel smectic phase is found in concentrated aqueous solutions of blunt-ended gapped DNA duplexes (all-DNA chain-sticks). A bilayer-like packing scenario within the smectic layers is proposed, in which the chain-sticks are folded and arranged in a stacking manner through the contact of their attractive blunt-ends. Through a combination of physics arguments, the authors have suggested that the folding of all-DNA chain-sticks is an entropy-driven process. In this chapter, this hypothesis is thoroughly examined by the synthesis and self-assembly behaviour of purely repulsive all-DNA chain-sticks. A rich concentration vs. chain length phase diagram demonstrates the emergence of various liquid crystalline phases, including an unconventional smectic-to-smectic transition at a critical chain length. In this novel liquid crystalline phase transition, the all-DNA chain-sticks within the smectic layers undergo a conformational change from an unfolded to folded state, offering compelling evidence for the entropic origin of the folding mechanism.

5.1 Introduction

All-DNA chain-sticks with attractive tips consist of a gapped DNA duplex with a contour length near DNA's persistence length, where two stiff blunt-ended DNA duplexes of equal length are connected by a single-stranded DNA (ssDNA) flexible spacer, which is composed solely of thymine (T) bases. The phase behaviour of these systems has been extensively studied in the Institute of Biological Information Processing (IBI-4) in Forschungszentrum Jülich.^{1,2} In this chapter, a phase diagram of purely repulsive all-DNA chain-sticks, depending on DNA concentration and spacer length, is constructed. To this end, a synopsis of the key experimental findings in self-assembly of the all-DNA chain-sticks with attractive terminal sites will be presented, together with some new data for selected ssDNA spacer lengths at high DNA densities. These gapped duplexes will be designated as G_{xT} -duplex, where x indicates the number of T bases that the ssDNA spacer contains. Schematic drawings of the G_{xT} -duplex and its full-paired duplex analogue (F-duplex), that are employed for the exploration of the liquid crystalline behaviour of all-DNA chain-stick molecules with monovalent terminal attractive sites, are presented in **Figure 5.1**.

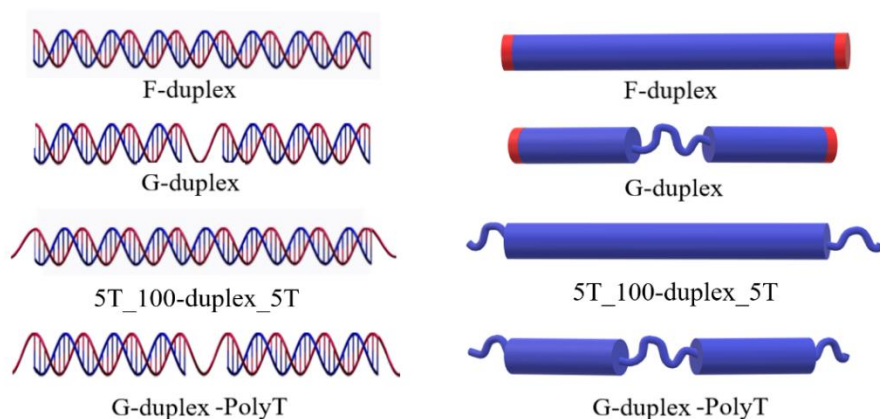


Figure 5.1 Schematic representation of the DNA duplexes used for the exploration of the LC behaviour of chain-stick molecules. From top to bottom: F-duplex, formed by combining two complementary ssDNA strands (red and blue strands) with a length of 116 bases. The blue rod depicts the DNA duplex and the red patches represent the blunt-ends; the G-duplex consists of one long DNA strand (red strand) and two short strands (blue ones), which are complementary to the parts of the long strand. In the 5T_100-duplex_5T system, the red patches are replaced with the polyT tails. The G-duplex-PolyT is a purely repulsive chain-stick molecule.

The F-duplex, 116 base-pairs (bp) long, was used as a reference system (Figure 5.1, first system from the top). In the all-DNA blunt-ended chain-sticks, the stiff duplex segments are 48bp long ($L_{dsDNA} \sim 16 \text{ nm}$), and the length of the flexible ssDNA spacer ranges within the interval $4T \leq L_{ssDNA} \leq 40T$. A combination of SAXS measurements and Monte Carlo simulations have demonstrated a novel and unconventional smectic-A type of liquid crystalline phase, so called Sm_b-A , for a long enough flexible spacer ($L_{ssDNA} \geq 10T$). The occurrence of such liquid crystalline phase is rather counterintuitive, since smectic ordering in aqueous solutions of stiff blunt-ended DNA duplexes does not occur.^{1,3,4} Furthermore, it is also unusual for such a phase to occur in flexible hard rod molecules since, according to the theoretical studies, the flexibility destabilizes the smectic phase.⁵⁻⁹ These studies revealed that an increase of flexibility shifts nematic-smectic coexistence densities towards higher values, accompanied with a shrinkage of the smectic layer thickness. Finally, it is expected that sufficiently flexible rods may not form a smectic at all. The authors of “Smectic phase in suspensions of gapped DNA duplexes”¹ have argued that the formation of smectic phase in all-DNA blunt-ended chain-sticks is possible owing to the self-folding ability of these molecules. The chain-sticks fold and stuck on top of each other due to the attractive forces acting between their blunt-ends, forming uniform smectic layers with thickness equal to one molecular length. In addition, has been hypothesized that the self-folding mechanism responsible for the formation of above-mentioned smectic phase with bilayer architecture (Sm_b-fA) is purely entropy-driven.

In order to confirm this entropic origin, we synthesized all-DNA chain-sticks with a 6T tail on both blunt ends, creating purely repulsive chain-stick molecules (G_{xT} -duplex-PolyT). This type of terminal modifications is proved sufficient to inhibit the blunt-end attractions (**Chapter 3** and **Chapter 4**). Such a system, schematically presented in the last sketch of **Figure 5.1**, is built by the self-assembly of three partially complementary ssDNA strands in a 1:1:1 stoichiometric ratio, as already explained in the subsection **2.3.3**. In this newly synthesized molecule, the length of the sticks is kept constant (48bp ($L_{dsDNA} = 48 \text{ bp} \sim 16 \text{ nm}$)), while the length of the flexible ssDNA spacer (L_{ssDNA}) varies between 3T and 30T. As a reference for these new systems, we used the already mentioned (see end of section **4.3.1**) 100 bp long DNA duplex, capped on both ends with non-sticky ssDNA dangling tails with length of 5 thymine bases (5T) (see the third system from the top, 5T_100-duplex_5T, in **Figure 5.1**). Blocking the blunt-ends stacking interactions with PolyT dangling tails results in the appearance of the smectic phase for all investigated ssDNA spacers.

5.2 Previous and current work on the all-DNA blunt-ended chain-sticks

The phase diagram of aqueous solutions of G_{xT} -duplexes ($4 \leq x \leq 40$) as a function of the ssDNA spacer length L_{ssDNA} is presented in **Figure 5.2**. The data plotted on this phase diagram was obtained from SAXS and POM experiments and they are published in the PhD thesis of Dr. Sanja Novak².

Figure 5.2 shows that the length of the ssDNA spacer affects the stability of the Sm_b - fA phase, the LC phase boundaries and the LC phase widths. The F-duplex was used as a reference point for understanding the effects of the spacer's flexibility on the LC phase sequence of G_{xT} -duplexes. In the phase diagram of **Figure 5.2**, the F-duplex phase behaviour is shown outside of the phase diagram, on the left-hand side of it. Looking at the biphasic region of the F-duplex, we notice that it is much narrower than in the case of polydisperse dsDNA fragments with number of base pairs around 146 ± 12 ¹⁰. This is expected since F-duplex is monodisperse in length. Therefore, we can exclude once again the possibility that the absence of the Sm phase is due to polydispersity in length. In the limit of long ssDNA spacer, G_{40T} -duplex, the formation of Sm_b - fA phase at high DNA concentrations is observed.

As already mentioned, when the chain-sticks fold, they attract each other through their blunt-ends, forming an unconventional bilayer Sm_b - fA . By calculating the length of the smectic layer from the 1D-SAXS profile of G_{40T} -duplex, we get the 39.25 nm, which roughly corresponds to the length of two folded chain-sticks stuck on top of each other. This packing scenario is schematically presented in **Figure 5.3**. Another observation worth of mention is the complete absence of the N^* phase and of the coexistence between I and Sm - fA . Decreasing the length of the flexible spacer to

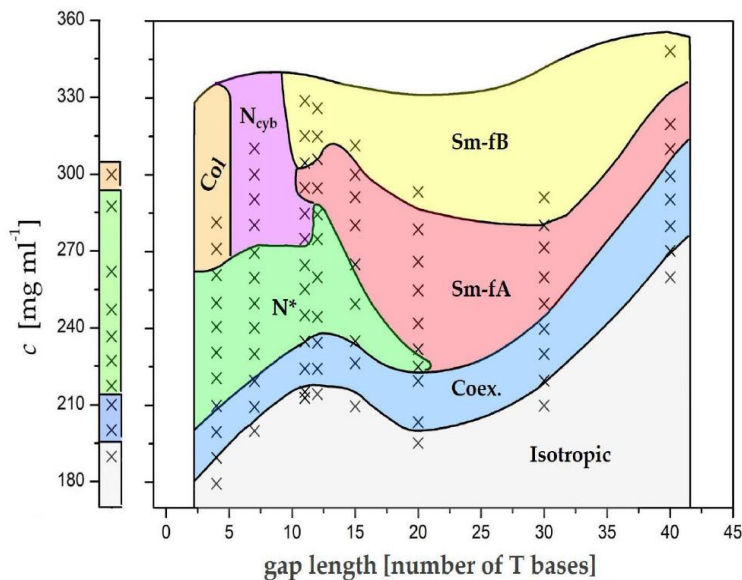


Figure 5.2 A full phase diagram of all-DNA blunt-ended chain-sticks, where ‘gap length’ refers to the length of the flexible ssDNA spacer. The coloured regions correspond to different LC phases. The black markers indicate the concentrations of the samples that were loaded in the capillaries for SAXS measurements. Outside the phase diagram, on the left side, the LC phase sequence of the F-duplex (116bp DNA duplex), is shown. The figure is reproduced from the PhD thesis of Dr S. Novak.²

30T(G_{30T}-duplex), the same LC phase sequence is observed, accompanied with the shrinkage of the coexistent region, which is shifted towards lower concentrations. The phase behaviour of the G_{20T}-duplex is quite different concerning the I/LC coexistence. An I/N* coexistence and a rather narrow one-phase N* are found after the isotropic

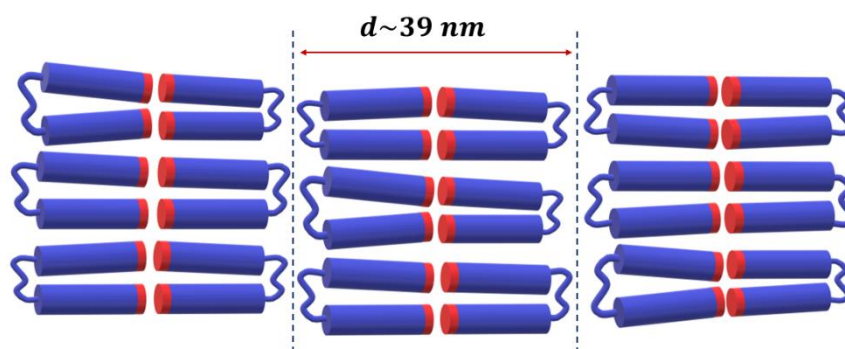


Figure 5.3 A schematic representation of the blunt-ended all-DNA chain-sticks molecular arrangement in a bilayer smectic folded phase (Sm_b-fA). Molecules are folded, and the thickness of the smectic layer corresponds to the length of the two folded chain-stick molecules stuck on top of each other, which roughly equals to $d \sim 39$ nm in the case of G_{40T}-duplex.

phase. Furthermore, a decrease of ssDNA spacer (from G_{40T}-duplex to G_{20T}-duplex) results in a decrease of the smectic layer's thickness from ~39 nm to ~35 nm. For $L_{ssDNA} = 12T$, the LC phase sequence remains the same, while the N^* region widens at the expense of Sm_b-fA . Moreover, in the case of G_{11T}-duplex, the N_{cyb} phase precedes Sm_b-fA . The nematic cybotactic (N_{cyb}), first observed around 70s,¹¹ is a liquid crystalline phase in which the molecules are arranged in clusters with a short-range layer-like structure.¹²⁻¹⁴ Further decreasing the length spacer (G_{7T}-duplex) results in the complete suppression of the smectic phase to the benefit of N_{cyb} phase. Finally, the G_{4T}-duplex is found to form LC phases similar to those observed for the F-duplex. The G_{4T}-duplex demonstrates that the sequence of phase transitions from lower to higher DNA concentrations is I -to- I/N^* -to- N^* - Col .

Additional SAXS experiments for selected G_{xT}-duplexes were performed in order to explore the phase behaviour at sufficiently high DNA densities. The new data, the type of LC phase and the corresponding SAXS pattern are presented in **Figure 5.4** and **Figure 5.5**. Interestingly, the 1D-SAXS profile of G_{7T}-duplex at the concentration of 430.44 mg/ml indicates the formation of a smectic phase with a layer thickness equal to nearly half of the molecular length. This implies that the clusters of folded G_{7T}-duplexes (N_{cyb}), at further compression, form a monolayer folded smectic phase (Sm_m-fA). The formation of monolayer instead of bilayer smectic may suggest that there is an apparent orientational component to the blunt-end base stacking interaction that is hard to be

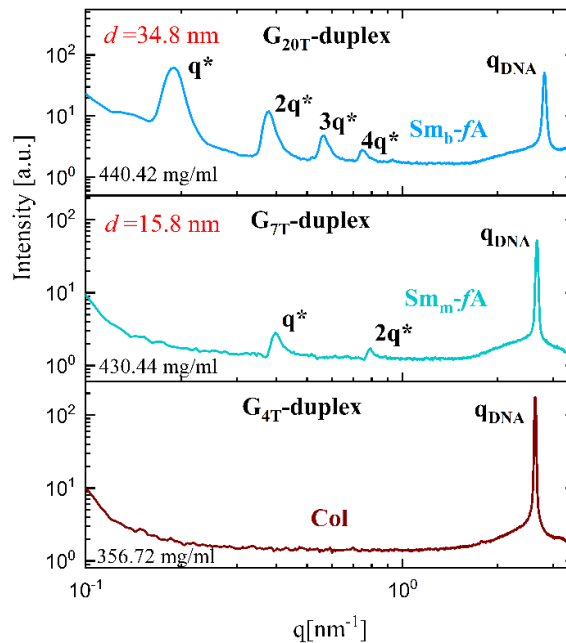


Figure 5.4 1D-SAXS scattering profiles for G_{4T}-duplex, G_{7T}-duplex and G_{20T}-duplex. For the each 1D-SAXS profile the corresponding type of phase behaviour is also indicated. The thickness of the smectic layers d for the G_{7T}-duplex implies the formation of the monolayer folded smectic-A (Sm_m-A).

stabilized at such high DNA densities. Contrary to the G_{7T} -duplex, the Sm_b - fA of the G_{20T} -duplex persists at notably high DNA concentration (440.42 mg/ml, 1D-SAXS profile in the top panel of **Figure 5.4**). Finally, in the case of G_{4T} -duplex, the Col phase remains stable up to 356.72 g/ml, without encountering any evidence of a smectic phase (third panel from the top in **Figure 5.4**).

Taken together, the above observations suggest that, for $L_{ssDNA} \leq 11T$, there is a delicate balance between the blunt-end base stacking and the ability of G_{xT} -duplexes to fold. It is particularly important to emphasize that a four-base loop is close to the minimum sterically accepted length.^{15,16} Therefore, it is unclear why the G_{4T} -duplex and G_{7T} -duplex were not able to fold in order to form a stable Sm_b - fA . Both base-stacking and self-folding are strongly involved in the formation of Sm_b - fA . Hence, in order to explore the entropic origin of the self-folding mechanism, purely repulsive all-DNA chain-sticks are synthesized by terminating both ends of G_{xT} -duplex with six-thymine (6T) dangling tails (G_{xT} -duplex-PolyT, **Figure 5.1**).

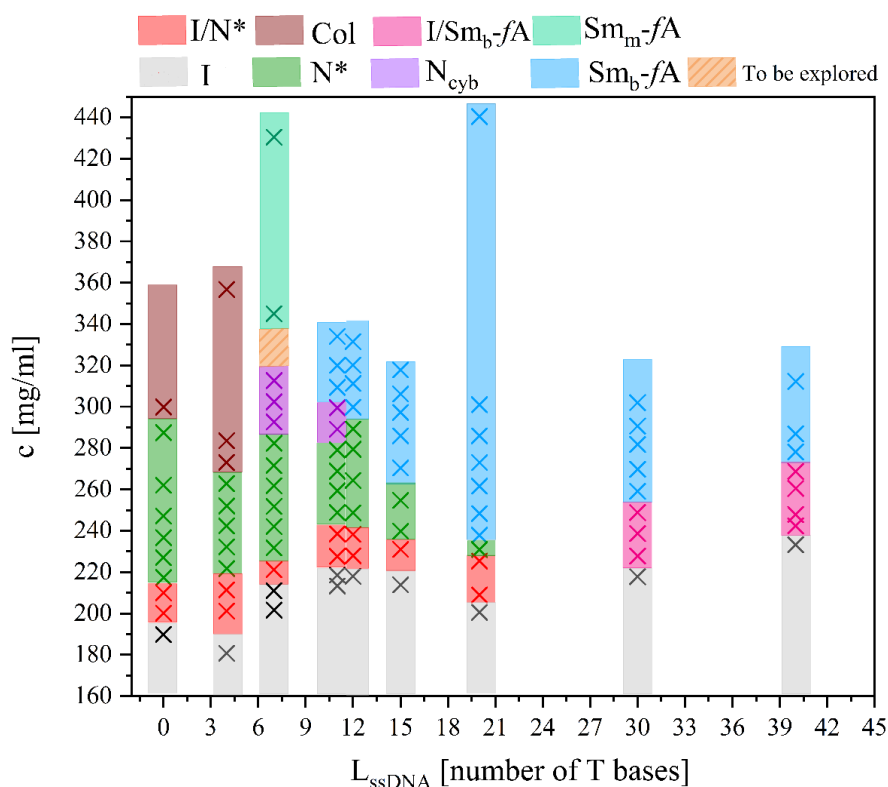


Figure 5.5 Replotted full phase diagram of blunt-ended all-DNA chain-sticks, with the addition of highly concentrated samples of G_{4T} -duplex, G_{7T} -duplex and G_{20T} -duplex. The length of the flexible ssDNA spacer ranges from 4T to 40T. Colourful markers represent the concentrations of the samples that were loaded into capillaries and measured with SAXS, where the colourful regions represent different LC phases (see legend above the diagram). The phases identification, and the determination of their boundaries, was possible with the combination of SAXS experiments, the visual inspection of the capillaries between cross-polarizers and the recording of the optical textures as observed by POM.

5.3 The self-assembly of purely repulsive all-DNA chain-sticks

In [Chapter 4](#), we demonstrated a successful interruption of the blunt-end stacking interactions in all-DNA rods by implementing a hairpin loop on one side, and a poly-thymine (poly-T) dangling tail (6T), on another side. In order to probe the impact of the absence of terminal attractions (blunt-ends) on the phase behaviour of all-DNA chain-sticks, both blunt-ends are modified with 6T dangling tails. Using hairpin loops, in this case, would not be possible, since there is a maximum length of the single stranded oligomer that could be produced synthetically. It shall be demonstrated that the above terminal modifications result in purely repulsive all-DNA chain-stick molecules. The length of the flexible ssDNA spacers varied from 3T to 30T.

The attraction screening efficiency of poly-T is demonstrated by the appearance of a smectic phase in G_{3T}-duplex-PolyT. It is important to note the absence of any kind of smectic phase in G_{4T}-duplex. In [Figure 5.6](#), X-ray scattering profiles of G_{3T}-duplex-PolyT are shown. At the concentration of 275.56 mg/ml, we observe a broad peak, which corresponds to N^* ordering ([Figure 5.6e](#)). By further increasing the concentration up to 295 mg/ml, we notice the appearance of four equidistant smectic peaks and a sharp high q_{DNA} peak superimposed with the broad one (light blue curve in [Figure 5.6d](#)). This indicates the coexistence between smectic and the less ordered N^* phase. The position of the maximum of the broad peaks remains at the same q value in both phases. At the concentration of 315.69 mg/ml, a sharp high q_{DNA} peak and a principal q^* peak, followed by other three equidistant peaks, are observed. The latter set of Bragg reflections indicate the formation of a smectic phase (see [Figure 5.6c](#)). The thickness of the smectic layer, ($d = 2\pi/q^*$), is found to be 34.05 nm, which roughly corresponds to the length of one G_{3T}-duplex-PolyT. This means that the system is in an unfolded conformation. This phase will be labelled as monolayer smectic-A phase ($Sm_m -A$). Surprisingly, at very high concentrations (above ~370 mg/ml), we observe an unusual smectic-to-smectic transition, where the purely repulsive all-DNA chain-sticks change their configuration within the layers from the unfolded to the folded state. This new phase is defined as monolayer smectic folded A ($Sm_m -fA$). Compelling evidence for the stability of this type of smectic phase is provided by the corresponding 1D-SAXS profile, presented in [Figure 5.6b](#). From the primary q^* peak position, the thickness of the smectic layers is calculated to be 16.1 nm. This corresponds to half the length of one G_{3T}-duplex-PolyT, which strongly implies that the chain-sticks are folded. A schematic of the suggested packing scenario for the $Sm_m -fA$ is depicted in [Figure 5.7](#).

Additionally, a comparison of 1D-SAXS profiles from G_{4T}-duplex and G_{4T}-duplex-PolyT at a similar DNA concentration, reveals that the presence of blunt-end attractions favours the development of the *Col* phase ([Figure 5.8a](#)). In [Figure 5.8b](#), a similar comparison for longer ssDNA spacers (7T), shows that the presence of blunt-end

attractions stabilizes the N^* phase and postpones the formation of Sm_m-fA (G_{7T} -duplex), which is immediately visible in the case of (G_{7T} -duplex-PolyT) at similar concentration.

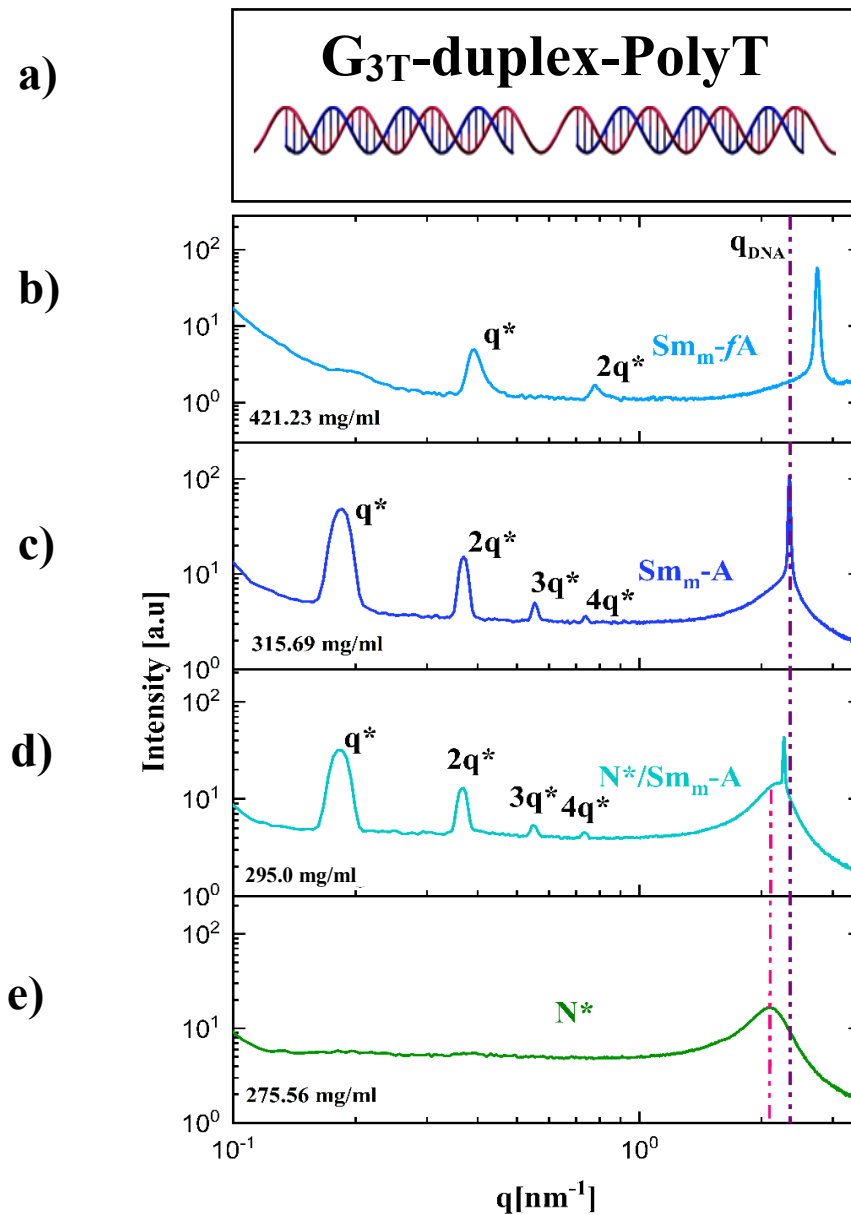


Figure 5.6 **a)** A schematic representation of the G_{3T} -duplex-PolyT **b)** 1D-SAXS profile of monolayer folded smectic-A phase (Sm_m-fA) at the concentration of 421.23 mg/ml **c)** A typical smectic 1D-SAXS scattering profile at the concentration of 315.69 mg/ml, which corresponds to the monolayer smectic-A phase (Sm_m-A). The purple dashed line across the whole figure enables an easier observation of the concentration dependence of the sharp high q_{DNA} peak. **d)** 1D-SAXS profile showing the coexistence between a sharp and a broad peak, which corresponds to the coexistence between the N^* and Sm_m-A phases at the concentration of 294.901 mg/ml. **e)** 1D-SAXS profile of the one-phase N^* (green curve, 275.56 mg/ml). The pink dashed line shows that the maximum of the broad peak for N^* and the N^*/Sm_m-A is located at the same q value.

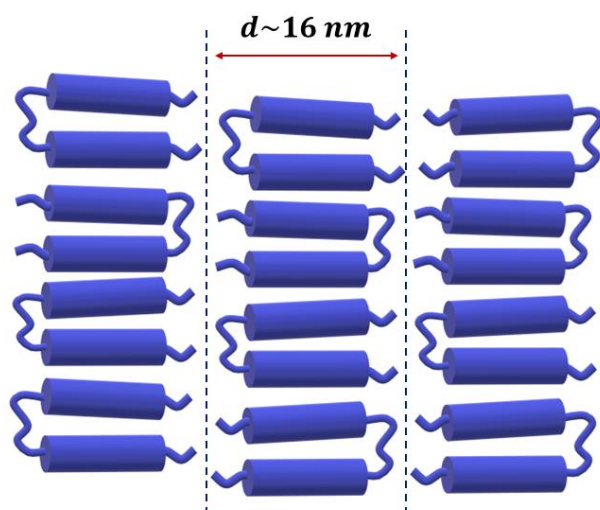


Figure 5.7 A schematic representation of the repulsive all-DNA chain-sticks, G_{4T} -duplex-PolyT, packing in a monolayer smectic folded phase, Sm_m-fA . The thickness of the smectic layers is around 16 nm, where the chain-sticks do not have preferred orientation within the layers.

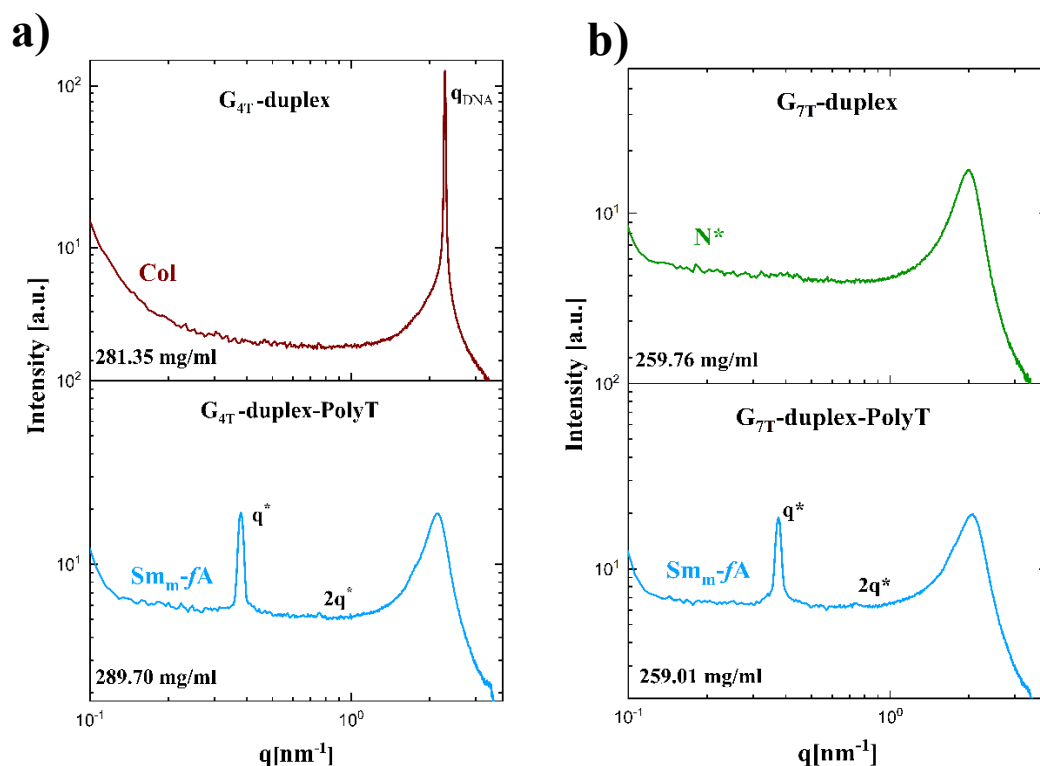


Figure 5.8 1D-SAXS profiles for **a)** G_{4T} -duplex (dark, red curve, top panel) and G_{4T} -duplex-PolyT (blue curve, bottom panel) **b)** G_{7T} -duplex (green curve, top panel) and G_{7T} -duplex-PolyT (blue curve, bottom panel) at almost similar DNA concentrations.

5.4 Phase diagram of the repulsive all-DNA chain-sticks

The SAXS measurements described in the previous paragraph are summarized in the phase diagram of **Figure 5.9**, where the DNA concentration is plotted against the length of ssDNA spacer L_{ssDNA} , which is given as number of T bases. The $L_{ssDNA} = 0$ corresponds to a fully paired DNA duplex, consisting of 100 bp having both ends terminated with a 5T dangling tails (5T_100-duplex_5T). This system corresponds to the repulsive stick-like counterpart of a chain-stick and allows to monitor the effect of the bending flexibility (G_{xT} -duplex-PolyT) on the phase behaviour of monodisperse rod-like particles. The crosses in the phase diagram of Figure 5.12, represent concentrations that were loaded into capillaries and measured with SAXS, where different colours represent different LC phases.

Purely repulsive all-DNA chain-sticks show a quite rich phase behaviour. The phase diagram of **Figure 5.9** demonstrates that the increase of ssDNA spacer not only changes the LC phase sequence, but also affects the phase boundaries. The 5T_100-duplex_5T

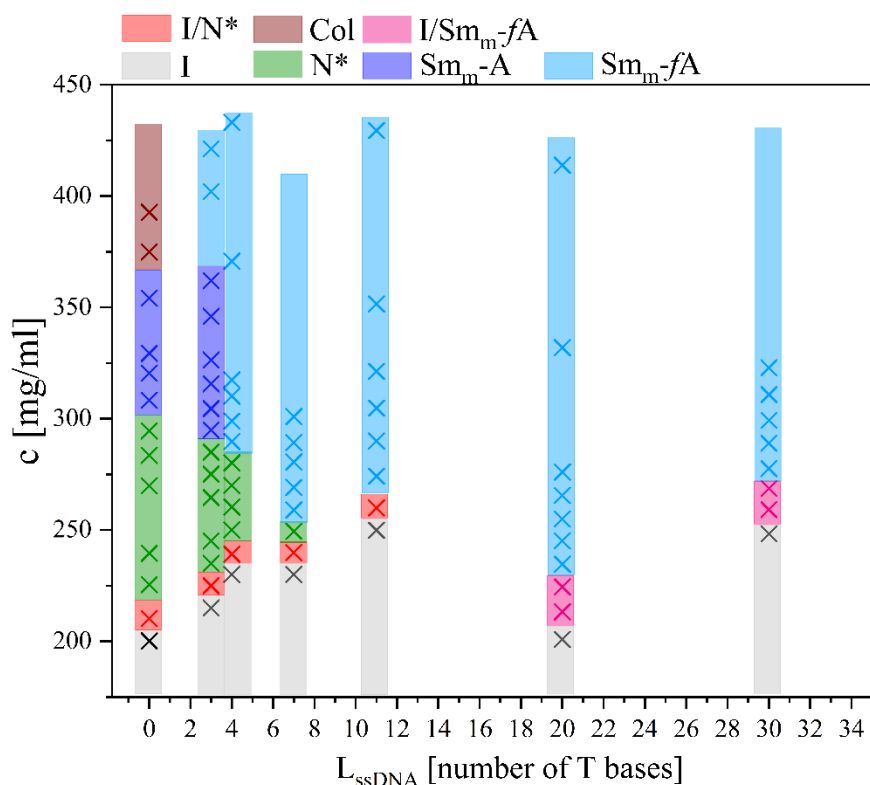


Figure 5.9 Phase diagram of repulsive all-DNA chain-sticks with $3T \leq L_{ssDNA} \leq 30T$. The colourful markers represent the concentrations of the samples that were loaded into capillaries and measured with SAXS, while the colourful regions represent different LC phases (see the legend above the phase diagram). The concentration-dependent phase behaviour of the fully-paired duplex, 5T_100-duplex_5T, is also plotted.

shows the expected phase sequence $I-I/N^*-N^*-Sm-Col$ for a repulsive rod-like particle. Inserting a flexible spacer in the middle of the rod and increasing its length results in the widening of the smectic region at the expense of N^* phase.

Starting from the G_{11T} -duplex-PolyT, it is observed that the N^* region is very narrow and, increasing the DNA concentration, results to the formation of the Sm_m-fA phase, that persists even up to very high concentrations. The increase of the flexible ssDNA spacer length to 20T (G_{20T} -duplex-PolyT) is accompanied with a complete suppression of the N^* phase and the emergence of a I/Sm_m-fA coexistence. In the case of G_{30T} -duplex-PolyT, the same phase sequence is still observed, but the phase boundaries are shifted towards higher DNA concentrations.

The concentration-dependent LC phase sequence is found to be similar for chain-sticks with a spacer length belonging to the interval $3T < L_{ssDNA} < 11T$. The sequence of phase transitions from lower to higher DNA concentrations ($I-I/N^*-N^*-Sm_m-fA$) is not changed; however, decreasing the length of the flexible ssDNA spacer results in the widening of the N^* at the expense of the Sm_m-fA . This finding is not surprising since the decrease of the ssDNA spacer length reduces its flexibility, making harder for the chain-stick to fold. Strikingly different is the LC phase sequence for $L_{ssDNA} = 3T$ (G_{3T} -duplex-PolyT). Besides the further widening of the N^* region, a unique smectic-to-smectic transition (Sm_m-A -to- Sm_m-fA) is observed, in which the all-DNA chain sticks within the smectic layers undergo a conformational change from an unfolded to a folded state. It is particularly important to note that the $L_{ssDNA} = 3T$ is very close to the minimum sterically acceptance length for the self-folding of ssDNA chain.^{15,16} Therefore, the above-mentioned transition can be understood in terms of restrictions in the ability of the ssDNA spacer to fold, which can be elevated by further compression of the system (increase of DNA concentration). However, it is expected that this condition will break down at smaller values of L_{ssDNA} . The existence of a concentration-dependent unfolded smectic to folded smectic transition at fixed length of ssDNA spacer is a direct consequence of the entropic origin of the self-folding mechanism in the gapped duplexes. Furthermore, the phase diagram of [Figure 5.9](#) shows that the same transition can be induced by altering the length of the ssDNA spacer at constant DNA concentration. The corresponding SAXS profiles are depicted in [Figure 5.10](#).

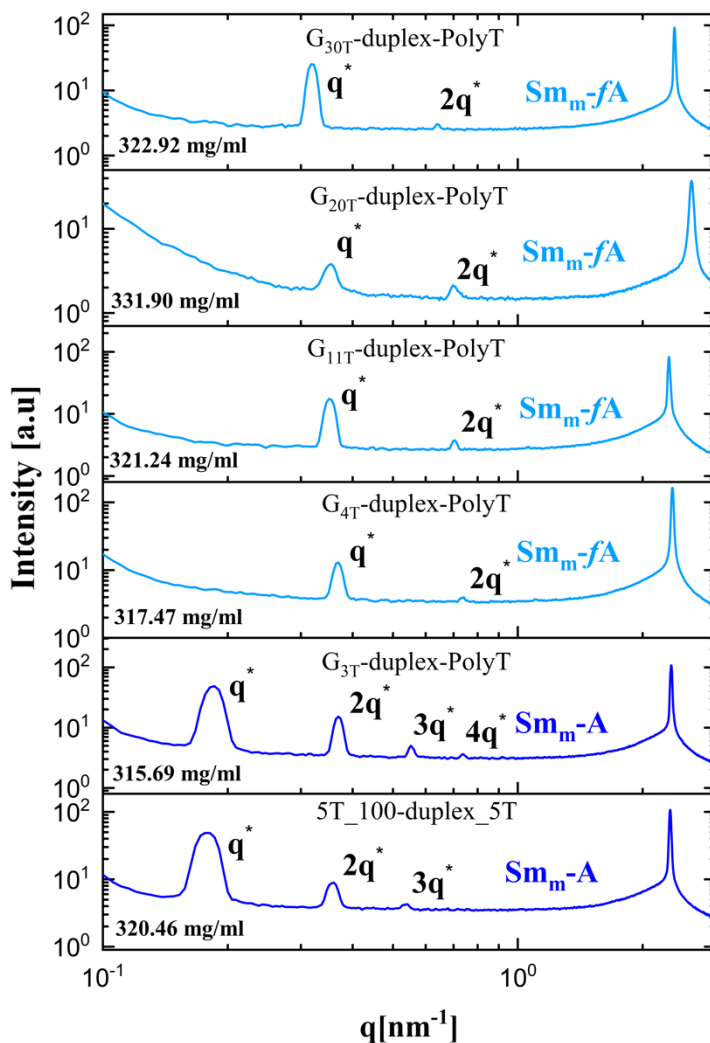


Figure 5.10 ID-SAXS profiles for repulsive all-DNA chain-sticks with different length of the ssDNA spacer, at similar DNA concentration. From bottom to top: $L_{ssDNA} = 0T, 3T, 4T, 11T, 20T$ and $30T$.

Summary and conclusions

Taken together, the work presented in this chapter on the self-assembly of all-DNA constructs with a chain-stick architecture demonstrates that these liquid crystalline building blocks exhibit a rich phase behaviour, owing to the unique DNA's inherent physico-chemical properties. Using the DNA, as a molecular building block, offered a superior control over the interactions involved in the self-assembly process. The key interactions are: the shape-based excluded volume interactions and the patchy interactions that contribute entropically and enthalpically to the self-assembly, respectively. Tuning of the above-mentioned interactions was accomplished through

molecular engineering of the particle flexibility and the attraction strength of the particle terminal sites. The former is precisely tuned by controlling the length of ssDNA spacer (L_{ssDNA}) on a sub-nanometre level (at single base level) and the latter is achieved by capping the DNA duplex's terminal sites (blunt-ends) with a Poly-T dangling tails.

The key mechanism for the formation and the stability of the reported unconventional smectic phases (Sm_b-fA and Sm_m-fA) and, a multiple order-to-order phase transitions (N^* -to- Sm_m-A -to- Sm_m-fA) in all-DNA chain sticks, is the ability of these anisotropic DNA constructs to fold. The entropic origin of the self-folding mechanism is unambiguously demonstrated by inhibiting the intermolecular base-stacking interactions between blunt-ended DNA helices. The study of the self-assembly behaviour of these purely repulsive all-DNA chain-sticks allowed us to decouple the terminal attractions from the folding mechanism, which are strongly intertwined in the case of blunt-ended all-DNA chain-sticks. As a direct consequence of this, at a critical length of the ssDNA spacer, a novel smectic (Sm_m-A)-to-smectic (Sm_m-fA) phase transition was found by increasing the DNA concentration, where the chain-sticks undergo a conformational change from the unfolded to folded state.

An intriguing aspect of this study is that the building block design could offer exquisitely tuneable means to engineer a potentially rich assortment of lyotropic liquid crystalline structures and self-assembly pathways. For example, an interesting new direction could be to study the self-assembly of all-DNA chain-sticks with competing interactions at the single-particle level. This can be achieved either by selectively blocking the DNA duplex's attractive sites (capping only the one terminal site) or by selectively altering the tethered all-DNA geometry (shape anisotropy).

Bibliography

1. Salamonczyk, M. *et al.* Smectic phase in suspensions of gapped DNA duplexes. *Nat. Commun.* **7**, 13358 (2016).
2. Novak, S. Self-assembly of anisotropic DNA-based patchy particles, PhD thesis. (Heinrich Heine University of Düsseldorf, 2019).
3. Livolant, F. & Bouligand, Y. Liquid Crystalline Phases Given By Helical Biological Polymers (Dna, Pblg and Xanthan). Columnar Textures. *J. Phys. Paris* **47**, 1813–1827 (1986).
4. Livolant, F., Levelut, A. M., Doucet, J. & Benoit, J. P. The highly concentrated liquid-crystalline phase of DNA is columnar hexagonal. *Nature* **339**, 724–726 (1989).
5. Van Der Schoot, P. The nematic-smectic transition in suspensions of slightly flexible hard rods. *J. Phys. II* **6**, 1557–1569 (1996).
6. Cinacchi, G. & De Gaetani, L. Phase behavior of wormlike rods. *Phys. Rev. E* **77**, 051705 (2008).
7. Tkachenko, A. V. Effect of chain flexibility on the nematic-smectic transition. *Phys. Rev. E* **58**, 5997–6002 (1998).
8. Bladon, P. & Frenkel, D. Simulating polymer liquid crystals. *J. Phys. Condens. Matter* **8**, 9445–9449 (1996).
9. de Braaf, B., Oshima Menegon, M., Paquay, S. & van der Schoot, P. Self-organisation of semi-flexible rod-like particles. *J. Chem. Phys.* **147**, 244901 (2017).
10. Merchant, K. & Rill, R. L. DNA length and concentration dependencies of anisotropic phase transitions of DNA solutions. *Biophys. J.* **73**, 3154–3163 (1997).
11. Chistyakov, I. G. & Chaikowsky, W. M. The Structure of p -Azoxybenzenes in Magnetic Fields . *Mol. Cryst.* **7**, 269–277 (1969).
12. Vries, A. De. X-ray Photographic Studies of Liquid Crystals I. A Cybotactic Nematic Phase. *Mol. Cryst. Liq. Cryst.* **10**, 219–236 (1970).
13. Vries, A. De. Microscopic Structure of Mesomorphic Phasesexperimental Investigations of the Structure of Thermotropic Liquid Crystals. *Le J. Phys. Colloq.* **36**, C1-1-C1-11 (1975).
14. Azároff, L. V. & Schuman, C. A. X-Ray Diffraction by Cybotactic Nematics. *Mol. Cryst. Liq. Cryst.* **122**, 309–319 (1985).
15. Haasnoot, C. A. G., Den Hartog, J. H. j., de Rooij, J. F. m., van Boom, J. H. & Altona, C. Loopstructures in synthetic oligodeoxynucleotides. *Nucleic Acids Res.* **8**, 169–182 (1980).
16. Haasnoot, C. A. G. *et al.* Structure, Kinetics and Thermodynamics of DNA Hairpin Fragments in Solution. *J. Biomol. Struct. Dyn.* **1**, 115–129 (1983).

Conclusions

The work described in this thesis is a step forward in the realization of programmable self-assembly in DNA-based liquid crystals. In general, the establishment of a well-defined set of instructions that direct the reproducible formation of a specific, pre-selected self-assembled structure is a challenging task in materials science. Here, the “assembly information” encoded into all-DNA building blocks is based on two pillars, namely: control of how shape-based excluded volume interactions contribute entropically to self-assembly through molecular engineering of the all-DNA scaffold; site-specific positioning of weak monovalent attractive patches on the surface of the all-DNA scaffold in the format of blunt-end stacking interactions. This hierarchical self-assembly approach is demonstrated by the synthesis of stiff all-DNA particles with control of both the internal flexibility (linear and chain-stick polymer topology) and the number of attractive terminal sites (blunt-ends).

In **Chapter 3**, it is demonstrated how a selective screening of the blunt-end attractions in stiff linear DNA fragments, on the basis of hairpin-capped DNA blunt-ends, can be developed to encode specific directionality in their intermolecular interactions (patchiness). The work at hand provides a full characterization of blunt-ends stacking interactions between DNA-duplexes and identifies the key role that they play in the formation of layered all-DNA structures. Through a combined experimental and simulation study, unambiguous evidence of the formation of a novel smectic phase with a bilayer architecture in one blunt-end capped DNA duplexes (semi-capped (SC)-duplexes) is provided. Interestingly, the lack of stacking polarity induced by the complete blocking of the blunt-end attractions (fully-capped (FC)-duplexes) reveal that the so far elusive monolayer smectic phase in DNA rod-like liquid crystal ordering is a thermodynamically stable phase. Moreover, contrary to the FC-duplex, the control over the strength of the terminal base-stacking (blunt-end) attraction in the SC-duplexes allowed to stabilize the hexagonal columnar phase at varying DNA densities reaching much higher values than in past studies. The molecular origin of this liquid crystalline phase was ascribed to the bending flexibility at the junction point of the SC-duplex dimers.

Building upon the knowledge gained in **Chapter 3**, purely repulsive all-DNA rods with variable shape anisotropy were synthesized. The study of their concentration-dependent self-assembly behaviour, using a combination of X-ray scattering and polarization microscopy, is presented in **Chapter 4**. The results revealed that the reported all-DNA rod system can be considered as an experimental realization of hard spherocylinders (cylinders of length L and diameter D capped with two hemispheres at both ends), since its phase behaviour can be mapped onto that of a corresponding hard-particle model system, simulated by Frenkel and co-workers in the early 1980's. The

reported DNA-based experimental rod-like system offers, for the first time, access to the small aspect ratio (L/D) region, revealing the existence of isotropic-smectic coexistence and the formation of a crystalline phase at high DNA densities, which is characterized by hexagonally ordered layers. The above-mentioned nanosized stiff all-DNA constructs of controlled size and shape allowed to explore the phase behaviour of purely repulsive rods with an astonishing aspect ratio resolution within $5.0 \leq L/D \leq 16.5$, establishing the proposed DNA-based system as a unique lyotropic liquid crystal platform for studying entropic-driven phase transitions.

Finally, in **Chapter 5**, the phase diagram of all-DNA chain-sticks is revisited. These all-DNA constructs consist of a gapped DNA duplex with a contour length near the DNA's persistence length, where two stiff blunt-ended DNA duplexes of equal length are connected by a variable length single-stranded DNA flexible spacer. Earlier studies have shown that concentrated aqueous solutions of these molecules form a bilayer smectic liquid crystalline phase. It was demonstrated that the all-DNA chain-sticks attain a folded conformation in this two-dimensional fluid layers mesophase, with the vertically aligned molecules having a long molecular axis almost perpendicular to the layer plane. The stabilization of this novel phase was attributed to a delicate balance of an entropy-driven (excluded volume reduction) self-organization and the presence of weak attractive stacking interactions between the blunt-ends. In this chapter, the entropic origin of the self-folding mechanism is directly addressed by the synthesis and study of the self-assembly behaviour of their purely repulsive counterparts. A rich self-assembly behaviour is found by altering the chain length, with the most prominent finding to be the concentration- and chain length-dependent smectic-to-smectic phase transition. In this novel and unconventional liquid crystalline phase transition, the purely repulsive all-DNA chain sticks within the smectic layers (each layer being one molecular length thick) undergo a conformational change from the unfolded to the folded state.

Natural DNA bases stack weakly to moderately. However, due to rapid developments in the fields of synthetic chemistry and automated synthesis of oligonucleotides, is feasible to integrate a variety of non-natural bases that attract each other via stacking interactions more strongly than the natural ones. This points the way towards the creation of a palette of monovalent patches with tuneable attraction strength. Given the great advances in static DNA self-assembly in the field of structural DNA nanotechnology, we foresee that complex anisotropic DNA nanoarchitectures with “blunt-end” patches of variable interaction strength, exposed at prescribed surface locations, will guide programmable strategies for the engineering of various exotic lyotropic liquid crystal phases with desired/tailored macroscopic properties.